AFRL-SN-WP-TR-2001-1122

Acquisition and Recognition of Moving Targets and Enabling Technologies Volume 1

Dr. Jian Li
Dr. Jose C. Principe

University of Florida
Department of Electrical and Computer Engineering
437 EB, P.O. Box 116130
Gainesville, FL 32611

JULY 2001

FINAL REPORT FOR PERIOD OF 15 MAY 1999 – 01 JUNE 2001

Approved for public release; distribution unlimited

20020103 139

SENSORS DIRECTORATE
AIR FORCE RESEARCH LABORATORY
AIR FORCE MATERIEL COMMAND
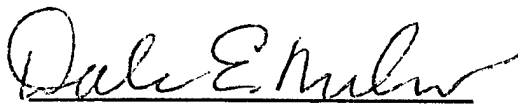WRIGHT-PATTERSON AIR FORCE BASE, OH 45433-7318

NOTICE

USING GOVERNMENT DRAWINGS, SPECIFICATIONS, OR OTHER DATA INCLUDED IN THIS DOCUMENT FOR ANY PURPOSE OTHER THAN GOVERNMENT PROCUREMENT DOES NOT IN ANY WAY OBLIGATE THE US GOVERNMENT. THE FACT THAT THE GOVERNMENT FORMULATED OR SUPPLIED THE DRAWINGS, SPECIFICATIONS, OR OTHER DATA DOES NOT LICENSE THE HOLDER OR ANY OTHER PERSON OR CORPORATION; OR CONVEY ANY RIGHTS OR PERMISSION TO MANUFACTURE, USE, OR SELL ANY PATENTED INVENTION THAT MAY RELATE TO THEM.

THIS REPORT IS RELEASABLE TO THE NATIONAL TECHNICAL INFORMATION SERVICE (NTIS). AT NTIS, IT WILL BE AVAILABLE TO THE GENERAL PUBLIC, INCLUDING FOREIGN NATIONS.

THIS TECHNICAL REPORT HAS BEEN REVIEWED AND IS APPROVED FOR PUBLICATION.

LOUIS A. TAMBURINO
Target Recognition Branch
Project Engineer

DALE E. NELSON, CHIEF
Target Recognition Branch

CLYDE R. HEDDINGS, Major, USAF
Deputy, Sensor ATR Technology Division
Sensors Directorate

Do not return copies of this report unless contractual obligations or notice on a specific document requires its return.

REPORT DOCUMENTATION PAGE

Public reporting burden for this collection of information is estimated to average 1 hour per response, including the time for reviewing instructions, searching existing data sources, gathering and maintaining the data needed, and completing and reviewing this collection of information. Send comments regarding this burden estimate or any other aspect of this collection of information, including suggestions for reducing this burden to Washington Headquarters Services, Directorate for Information Operations and Reports, 1215 Jefferson Davis Highway, Suite 1204, Arlington, VA 22202-4302, and to the Office of Management and Budget, Paperwork Reduction Project (0704-0188), Washington, DC 20503

1. AGENCY USE ONLY (Leave blank)	2. REPORT DATE July 2001	3. REPORT TYPE AND DATES COVERED Final, 05/15/1999 – 06/01/2001

4. TITLE AND SUBTITLE Acquisition and Recognition of Moving Targets and Enabling Technologies Volume 1	5. FUNDING NUMBERS C: F33615-99-1-1507 PE: 63762E PR: ARPS TA: NA
6. AUTHOR(S) Dr. Jian Li Dr. Jose C. Principe	WU: 0L

7. PERFORMING ORGANIZATION NAME(S) AND ADDRESS(ES) University of Florida Department of Electrical and Computer Engineering 437 EB, P.O. Box 116130 Gainesville, FL 32611	8. PERFORMING ORGANIZATION REPORT NUMBER

9. SPONSORING / MONITORING AGENCY NAME(S) AND ADDRESS(ES) SENSORS DIRECTORATE AIR FORCE RESEARCH LABORATORY AIR FORCE MATERIEL COMMAND WRIGHT-PATTERSON AIR FORCE BASE, OH 45433-7318 POC: Louis A. Tamburino, AFRL/SNAT, 937-255-1115 x4389	10. SPONSORING / MONITORING AGENCY REPORT NUMBER AFRL-SN-WP-TR-2001-1122

11. SUPPLEMENTARY NOTES
The work in this report is published in several journals and conference proceedings. This is Volume 1 of 2.

12a. DISTRIBUTION / AVAILABILITY STATEMENT Approved for public release; distribution unlimited.	12b. DISTRIBUTION CODE

13. ABSTRACT *(Maximum 200 Words)*
State-of-the-art research on spectral estimation, feature extraction, and pattern recognition algorithms are presented for radar signal processing and automatic target recognition. Advanced space-time spectral estimation algorithms are presented for multiple moving target feature extraction as well as clutter and jamming suppression for airborne high range resolution (HRR) phased-array radar. A nonparametric adaptive filtering-based approach, referred to as the Gapped-data Amplitude and Phase EStimation (GAPES) algorithm, is proposed for the spectral analysis of gapped data sequences as well as synthetic aperture radar (SAR) imaging with angle diversity data fusion. A QUasi-parametric ALgorithm for target feature Extraction (QUALE) algorithm is also investigated for angle diversity data fusion. Support Vector Machines (SVMs) as compared with other advanced classifiers in the MSTAR Public Domain Release and HRR data are found to outperform neural networks and matched filters. A new concept to create negative examples from the known target class is presented and shown to tremendously improve the rejection of confusers. Finally, Information Theoretic Learning (ITL) is proposed as a new algorithm to demix HRR signatures of closely parked targets.

14. SUBJECT TERMS Space-Time Processing, Moving Target Detection and Feature Extraction, SAR Imaging, Angle Diversity, Data Fusion, Support Vector Machines, Confuser Rejection, Information Theoretic Learning	15. NUMBER OF PAGES 102
	16. PRICE CODE

17. SECURITY CLASSIFICATION OF REPORT Unclassified	18. SECURITY CLASSIFICATION OF THIS PAGE Unclassified	19. SECURITY CLASSIFICATION OF ABSTRACT Unclassified	20. LIMITATION OF ABSTRACT SAR

NSN 7540-01-280-5500

Contents

5 A Quasi-parametric Algorithm for SAR Target Feature Extraction and Imaging with Angle Diversity   72

Abstract

This document presents advanced spectral estimation techniques for multiple moving target feature extraction, spectral analysis of one-dimensional (1-D) gapped data sequences, and synthetic aperture radar (SAR) imaging with angle diversity data fusion.

For the multiple moving target feature extraction problem, we study clutter suppression and feature extraction of multiple moving targets for airborne high range resolution (HRR) phased array radar. We show how to use a Vector Auto-Regressive (VAR) filtering technique to suppress the correlated ground clutter and propose a relaxation-based parameter estimation algorithm for multiple moving target feature extraction. For the spectral analysis of gapped data sequences, we present an algorithm for nonparametric complex spectral estimation of gapped data via an adaptive filtering approach, referred to as the GAPES (Gapped-data Amplitude and Phase EStimation) algorithm, which iterates between steps of estimating the adaptive filter and the corresponding spectrum via APES (Amplitude and Phase EStimation) and filling in the gaps via a least squares (LS) fitting. For the SAR imaging with angle diversity data fusion, we study both nonparametric and quasi-parametric methods. For the nonparametric method, we propose to use the GAPES algorithm to fill in the gaps in a range-wise mode and then use a two-dimensional (2-D) APES algorithm to obtain the final 2-D SAR image. For the quasi-parametric method, we first establish a flexible data model that describes each target scatterer as a 2-D complex sequence with arbitrary amplitude and constant phase in range and cross-range. Then we present an algorithm, referred to as QUALE (QUasi-parametric ALgorithm for target feature Extraction), for the SAR target feature extraction and imaging with angle diversity data fusion based on the flexible data model. Numerical results are presented to illustrate the performances of all algorithms proposed in the document.

1. Introduction

This document presents advanced spectral estimation techniques for multiple moving target feature extraction, spectral analysis of one-dimensional (1-D) gapped data sequences, and synthetic aperture radar (SAR) imaging with angle diversity data fusion.

For the multiple moving target feature extraction problem, we study clutter suppression and feature extraction of multiple moving targets for airborne high range resolution (HRR) phased array radar. We show how to use a Vector Auto-Regressive (VAR) filtering technique to suppress the correlated ground clutter and propose a relaxation-based parameter estimation algorithm for multiple moving target feature extraction. For the spectral analysis of gapped data sequences, we present an algorithm for nonparametric complex spectral estimation of gapped data via an adaptive filtering approach, referred to as the GAPES (Gapped-data Amplitude and Phase EStimation) algorithm, which iterates between steps of estimating the adaptive filter and the corresponding spectrum via APES (Amplitude and Phase EStimation) and filling in the gaps via a least squares (LS) fitting. For the SAR imaging with angle diversity data fusion, we study both nonparametric and quasi-parametric methods. For the nonparametric method, we propose to use the GAPES algorithm to fill in the gaps in a range-wise mode and then use a two-dimensional (2-D) APES algorithm to obtain the final 2-D SAR image. For the quasi-parametric method, we first establish a flexible data model that describes each target scatterer as a 2-D complex sequence with arbitrary amplitude and constant phase in range and cross-range. Then we present an algorithm, referred to as QUALE (QUasi-parametric ALgorithm for target feature Extraction), for the SAR target feature extraction and imaging with angle diversity data fusion based on the flexible data model.

This document contains 5 chapters. In Chapter 2, we study the multiple moving target feature extraction for airborne HRR phased array radar. Chapter 3 presents a technique for nonparametric spectral analysis of gapped data sequences. In Chapters 4 and 5, we study the SAR imaging with angle diversity data fusion via nonparametric and quasi-parametric methods, respectively.

In Chapter 2, we study the clutter suppression and feature extraction of multiple moving targets for HRR phased array radar. To avoid range migration problems that occur in the HRR radar data, we divide each HRR profile into non-overlapping low range resolution (LRR) segments, so that each LRR segment contains a sequence of HRR range bins. No information is lost due to the division and hence no loss of resolution occurs. We show how to use the VAR filtering technique to suppress the correlated ground clutter. Then a relaxation-based parameter estimation algorithm is presented for multiple moving target feature extraction. The problem of multiple target feature extraction is reduced to the feature extraction of a single target in a relaxation-based iteration step. In each iteration step and for each target, the target phase history sequence and Direction-Of-Arrival (DOA) (or the unknown array manifold) are estimated from some spatial signature vectors by minimizing a Weighted Least Squares (WLS) cost function. The complex amplitude and range of each target scatterer are then extracted from the estimated target phase history sequence by using RELAX, a target feature extraction algorithm with super resolution performance.

In Chapter 3, We present the GAPES algorithm for nonparametric complex spectral estimation of gapped data. Unlike the fast Fourier transform (FFT), windowed or averaged FFT spectra, the APES spectrum has good resolution properties, suffers from little or no leakage effects, and has good statistical stability. The excellent performance of APES in this class of nonparametric spectral analysis methods is one of the reasons why we choose to extend this particular approach to the gapped-data case. The incomplete data sequence may contain gaps of various sizes. The GAPES algorithm iterates the following two steps: (1) estimating the adaptive FIR filter and the corresponding complex spectrum via APES, and (2) filling in the gaps via a LS fitting criterion. The initial condition for the iteration is obtained from the available data segments via APES.

In Chapter 4, we investigate the SAR imaging with angle diversity data fusion via GAPES. The APES and GAPES algorithms are first introduced for the spectral estimations of complete and gapped data, respectively. For the angle diversity data fusion for SAR imaging, the radar measurements in range are complete whereas the gaps are caused by the intermittent measurement mode and thus only exist in the azimuth (cross-range) dimen-

2

sion. We perform the 1-D windowed FFTs (WFFTs) in range, use the GAPES algorithm to interpolate the gaps in the aperture for each range, apply the 1-D inverse FFTs (IFFTs) and de-window in range, and apply the two-dimensional (2-D) APES algorithm to the interpolated matrix to obtain the final 2-D SAR image.

In Chapter 5, We first establish a flexible data model that describes each target scatterer as a 2-D complex sinusoid with arbitrary amplitude and constant phase in range and cross-range, and then present the QUALE algorithm for SAR target feature extraction and imaging via data fusion through angle diversity based on the established flexible data model. QUALE first estimates the model parameters that include, for each scatterer, a 2-D arbitrary real-valued amplitude sequence, a constant phase, and scatterer locations in range and cross-range. QUALE then averages the estimated 2-D real-valued amplitude sequence over range by making the assumption that the scatterer radar cross section (RCS) is approximately constant. QUALE next models the so-obtained 1-D sequence with a simple sinc function by assuming that the scatterer is approximately a dihedral (a trihedral is approximated as a very short dihedral), and estimates the relevant sinc function parameters by minimizing a nonlinear least squares (NLS) fitting function. Finally, the approximate 2-D SAR image is reconstructed by using the estimated features.

Each of the aforementioned chapters is self-contained with its own introduction, formulation of the problem of interest, detailed presentation of approaches, conclusions, and references. We acknowledge Dr. Rob Williams of Air Force Research Laboratory for giving us the interesting research topic of SAR imaging with angle diversity data fusion.

2. Multiple Moving Target Feature Extraction for Airborne HRR Radar

2.1 Introduction

Clutter and jamming suppression is critical for airborne radar signal processing. The ground clutter observed by an airborne radar is spread over two dimensions of both the range and spatial angle and the clutter spectrum also covers a certain Doppler region due to the platform motion. A Vector Auto-Regressive (VAR) filtering technique was recently proposed by Swindlehurst and Stoica [1] to suppress the clutter adaptively. It is more robust than the non-adaptive Displaced-Phase-Center-Antenna (DPCA) processing since the latter is sensitive to both array calibration errors and system mismatch. The VAR filtering technique whitens the correlated clutter only temporally and can be computationally simpler than the conventional Space-Time Adaptive Processing (STAP) based techniques, which may require a significant amount of computations due to the need of using a bank of filters and the inversions of matrices of large dimensions. STAP cannot be used for jamming suppression if the secondary data bins used to obtain the second-order statistics of the ground clutter do not contain jamming interference. Although the VAR filtering technique can be easily used for spatial whitening as well, it is not needed since the VAR-filtered interference is assumed to be spatially colored with an unknown and arbitrary covariance matrix, which automatically achieves jamming suppression when the VAR filter output is used with the Maximum Likelihood (ML) methods presented by Swindlehurst and Stoica [1] to estimate the target parameters for Low Range Resolution (LRR) wide-area surveillance radar.

Future airborne radars will be required to provide increasingly High Range Resolution (HRR) features of ground targets, which makes the signal processing needed by airborne HRR phased array radars even more important. Compared to a conventional airborne LRR radar [2], an airborne HRR radar can not only enhance the radar's capability of detecting, locating, and tracking moving targets, but also can provide more features for applications including Automatic Target Recognition (ATR) [3, 4]. To avoid the range migration problems

4

that occur in HRR radar data, we first divide the HRR range profiles into LRR segments. Since each LRR segment contains a sequence of HRR range bins, no information is lost due to the division and hence no loss of resolution occurs. We extend the VAR filtering technique and the unstructured ML method in [1] for clutter suppression and single target feature extraction for airborne HRR phased array radar. The target phase history sequence and Direction-Of-Arrival (DOA) (or the unknown array manifold) are estimated from some spatial signature vectors by minimizing a Weighted Least Squares (WLS) cost function, and the complex amplitude and range of each target scatterer are extracted from the estimated target phase history sequence by using RELAX [5].

We also extend the single target approaches to the case of multiple targets. The multiple moving target scenario occurs frequently in radar applications. Yet to the best of our knowledge, little research on the topic has been reported in the literature. We present a relaxation-based algorithm for multiple moving target feature extraction. Each of the targets is assumed to have a rigid-body and the scatterers of the same target have the same DOA. The relaxation-based algorithm is used to minimize a nonlinear least squares fitting function by letting only the parameters of one target vary at a time while fixing the parameters of all other targets at their most recently determined values. Thus the problem of multiple target feature extraction is reduced to the feature extraction of a single target in a relaxation-based iteration step. We use numerical examples to demonstrate the performance of this algorithm for clutter suppression and multiple moving target feature extraction.

The remainder of this paper is organized as follows. In Section 2, we establish the multiple moving target data model for airborne HRR phased array radar, which is followed by a brief discussion of the VAR filtering technique. In Section 3, we present the relaxation-based multiple moving target feature extraction method. Simulation results and their analysis are presented in Section 4. Finally, we give the conclusions in Section 5.

2.2 Data Model and VAR Filtering

The range resolution of a radar is determined by the transmitted signal bandwidth. To achieve high range resolution, a radar must transmit wide band pulses, which are often linear frequency modulated (LFM) chirp signals [6]. The range resolution of a LRR radar is much larger than the length of a target so that the target occupies only one LRR range bin, while the range resolution of a HRR radar is so small that each target occupies several HRR range bins.

Consider an airborne HRR radar having a one-dimensional (1-D) antenna array with M elements uniformly spaced along the flight path of an airborne platform. A cluster of N chirp pulses is transmitted during a coherent processing interval (CPI). After dechirping, sampling, and Fourier transforming the signals in each element of the array, we obtain the HRR range profiles. Without clutter and jamming suppression, these clutter and jamming dominated profiles are not useful for any applications. To avoid range migration problems, we divide each HRR profile into non-overlapping LRR segments so that each LRR segment contains L HRR range bins, as shown in Figure 2.1. We choose L to be much larger than the maximum number of range bins over which all targets can possibly expand and migrate during the CPI. We then apply inverse Fourier transform to each segment. For the segment of interest, where targets may be present, the inverse Fourier transform yields the primary data. We assume that D targets are present in the primary data with the dth target consisting of K_d scatterers. We assume that the scatterers of each target have the same Doppler frequency and the same DOA, but different complex amplitudes and range frequencies. Then the primary data model can be written as (see Appendix A for the model derivation):

$$
\mathbf{x}_l(n) = \sum_{d=1}^{D} \left(\sum_{k=1}^{K_d} \alpha_{dk} e^{j2\pi f_{dk} l} \right) e^{j v_d n l} e^{j \omega_d n} \mathbf{a}(\theta_d) + \mathbf{e}_l(n),
$$
$$
l = 0, \cdots, L-1, \quad n = 0, \cdots, N-1, \tag{2.1}
$$

where $\mathbf{x}_l(n)$ is the array output vector of the lth phase history sample due to the nth pulse; $\mathbf{a}(\theta_d)$ is the array manifold and is a function of the dth target DOA θ_d relative to the flight path; $\mathbf{e}_l(n)$ is the interference including the temporally and spatially correlated Gaussian

ground clutter, both temporally and spatially white Gaussian noise, and possibly a jammer that is temporally white but a point source in space. We assume that the clutter, noise, and jamming in different HRR range bins are independent and identically distributed. The complex amplitude α_{dk} and the frequency f_{dk} are, respectively, proportional to the RCS and range of the kth scatterer of the dth target. The v_d and ω_d are, respectively, the scaled radial velocity and the normalized Doppler frequency of the dth target. Range migration can occur due to the radial motion between the radar and target and the high range resolution of the HRR radar. For notational convenience, let

$$\omega_{dl} = \omega_d(1 + rl), \quad l = 0, \cdots, L - 1, \quad d = 1, \cdots, D, \tag{2.2}$$

where $r = v_d/\omega_d$ is a known constant independent of the target motion (see Appendix A) and is usually very small ($\ll 0.01$). Then (2.1) can be written as

$$\mathbf{x}_l(n) = \sum_{d=1}^{D} b_{dl}e^{j\omega_{dl}n}\mathbf{a}_d + \mathbf{e}_l(n), \quad l = 0, \cdots, L - 1, \quad n = 0, \cdots, N - 1, \tag{2.3}$$

where we drop the dependence of $\mathbf{a}_d$ on θ_d for notational brevity and $b_{dl} = \sum_{k=1}^{K_d} \alpha_{dk}e^{j2\pi f_{dk}l}$. Note that, when $L = 1$, the model in (2.3) reduces to the data model for the LRR case. For $L > 1$, we have a phase history sequence for each LRR segment and no loss of range resolution occurs because of no information loss.

The secondary data are obtained from segments adjacent to the segment of interest in the same way as the primary data are obtained from the segment of interest (see Figure 2.1. The secondary data are assumed to be target free (see [7] for the latest research results on the selection of secondary data) and are modeled as a VAR random process [1]. The VAR filter has the form:

$$\mathcal{H}(z^{-1}) = \mathbf{I} + \sum_{p=1}^{P} \mathbf{H}_p z^{-p}, \tag{2.4}$$

where P is the VAR filter order, z^{-1} denotes the unit delay operator, and $\mathbf{I}$ is the identity matrix.

Next, we outline the estimation of the VAR filter $\mathcal{H}(z^{-1})$ using the target-free secondary data. Let $\mathbf{e}_{sl}(n)$, $s = 1, \cdots, S$, $l = 0, \cdots, L - 1$, $n = 0, \cdots, N - 1$, denote the secondary

data, where S denotes the number of secondary data segments. From

$$\hat{H}_1, \cdots, \hat{H}_P = \arg \min_{H_1, \cdots, H_P} \sum_{l=0}^{L-1} \sum_{s=1}^{S} \sum_{n=P}^{N-1} \left\| e_{sl}(n) + \sum_{p=1}^{P} H_p e_{sl}(n-p) \right\|^2, \qquad (2.5)$$

with $\|\cdot\|$ denoting the Euclidean norm, we get

$$\hat{H} = E\Psi^H \left(\Psi\Psi^H \right)^{-1}, \qquad (2.6)$$

where

$$\Psi = [\Psi_{10} \ \cdots \ \Psi_{sl} \ \cdots \ \Psi_{S(L-1)}],$$

$$E = [E_{10} \ \cdots \ E_{sl} \ \cdots \ E_{S(L-1)}],$$

$$\Psi_{sl} = [\psi_{sl}(P) \ \cdots \ \psi_{sl}(N-1)],$$

$$\psi_{sl}(n) = - \left[e_{sl}^T(n-1) \cdots e_{sl}^T(n-P) \right]^T,$$

and

$$E_{sl} = [e_{sl}(P) \ \cdots \ e_{sl}(N-1)], \quad l = 0, \cdots, L-1, \quad s = 1, \cdots, S,$$

with $(\cdot)^T$ and $(\cdot)^H$ denoting the transpose and conjugate transpose, respectively.

Once the VAR filter coefficients are determined, we use the filter to suppress the clutter in the primary data. The VAR filter output for the primary data has the form

$$\begin{aligned} y_l(n) &= \hat{\mathcal{H}}(z^{-1})x_l(n) \\ &= \sum_{d=1}^{D} b_{dl} \hat{\mathcal{H}}_{dl} a_d e^{j\omega_{dl}n} + \epsilon_l(n), \\ &\quad l = 0, \cdots, L-1, \quad n = P, \cdots, N-1, \end{aligned} \qquad (2.7)$$

where $\hat{\mathcal{H}}(z^{-1})$ has the same form as $\mathcal{H}(z^{-1})$ in (2.4) except that the $\{H_p\}_{p=1}^{P}$ in (2.4) are replaced by $\{\hat{H}_p\}_{p=1}^{P}$,

$$\hat{\mathcal{H}}_{dl} = I + \sum_{p=1}^{P} \hat{H}_p e^{-j\omega_{dl}p}, \quad l = 0, \cdots, L-1, \quad d = 1, \cdots, D, \qquad (2.8)$$

and

$$\epsilon_l(n) = \hat{\mathcal{H}}(z^{-1})e_l(n), \quad l = 0, \cdots, L-1, \quad n = P, \cdots, N-1. \qquad (2.9)$$

8

Let

$$\bar{\alpha}_{dl} = b_{dl}\hat{\mathcal{H}}_{dl}\mathbf{a}_d, \quad l = 0, \cdots, L-1, \quad d = 1, \cdots, D, \tag{2.10}$$

be referred to as the *spatial signature vector* of the dth target for the lth phase history sample. Then (2.7) can be rewritten as

$$\mathbf{y}_l(n) = \sum_{d=1}^{D} \bar{\alpha}_{dl}e^{j\omega_{dl}n} + \epsilon_l(n), \quad l = 0, \cdots, L-1, \quad n = P, \cdots, N-1. \tag{2.11}$$

Our problem of interest is to estimate $\{\omega_d, \ \theta_d, \ \{\alpha_{dk}, \ f_{dk}\}_{k=1}^{K_d}\}_{d=1}^{D}$ if the array manifold $\{\mathbf{a}(\theta_d)\}_{d=1}^{D}$ is known or $\{\omega_d, \ \mathbf{a}_d, \ \{\alpha_{dk}, \ f_{dk}\}_{k=1}^{K_d}\}_{d=1}^{D}$ if the array manifold $\{\mathbf{a}(\theta_d)\}_{d=1}^{D}$ is unknown from the VAR filter output $\mathbf{y}_l(n), \quad l = 0, \cdots, L-1, \quad n = P, \cdots, N-1$, by minimizing Nonlinear Least Squares (NLS) criteria using a relaxation-based optimization algorithm.

2.3 Feature Extraction of Multiple Moving Targets

Our feature extraction algorithm consists of the following two separate steps:

Step I: Estimate the target space-time parameters $\{\omega_d, \ \theta_d, \ \{b_{dl}\}_{l=0}^{L-1}\}_{d=1}^{D}$ if the array manifold $\{\mathbf{a}(\theta_d)\}_{d=1}^{D}$ is known or $\{\omega_d, \ \mathbf{a}_d, \ \{b_{dl}\}_{l=0}^{L-1}\}_{d=1}^{D}$ if the array manifold is unknown from the VAR filter output $\{\mathbf{y}_l(n)\}, \quad l = 0, \cdots, L-1, \quad n = P, \cdots, N-1$.

Step II: Estimate the target range parameters $\{\alpha_{dk}, \ f_{dk}\}_{k=1}^{K_d}, \ d = 1, \cdots, D$, from the estimate $\{\hat{b}_{dl}\}_{l=0}^{L-1}$ of $\{b_{dl}\}_{l=0}^{L-1}$ obtained in **Step I**.

2.3.1 Space-Time Parameter Estimation

The NLS estimates of the space-time parameters $\{\omega_d, \ \theta_d, \ \{b_{dl}\}_{l=0}^{L-1}\}_{d=1}^{D}$ or $\{\omega_d, \ \mathbf{a}_d, \ \{b_{dl}\}_{l=0}^{L-1}\}_{d=1}^{D}$ can be obtained by minimizing the following NLS criterion:

$$C_1 = \sum_{l=0}^{L-1} \left\| \mathbf{y}_l(n) - \sum_{d=1}^{D} \bar{\alpha}_{dl}e^{j\omega_{dl}n} \right\|^2. \tag{2.12}$$

The minimization of the cost function C_1 in (2.12) is a highly nonlinear complicated optimization problem. Here we present an alternating or relaxation-based optimization approach, which is a conceptually and computationally simple method for multiple moving target feature extraction. The relaxation-based algorithm is used to minimize C_1 by letting only the

9

parameters of one target vary at a time while fixing the parameters of all other targets at their most recently determined values. Therefore, the feature extraction of multiple moving targets is reduced to the feature extraction of a single moving target in a relaxation-based iteration step. We first consider the space-time parameter estimation of the dth target and then give detailed steps of our approach for multiple targets.

Space-Time Parameter Estimation of the dth Target

Let

$$\mathbf{y}_{dl}(n) = \mathbf{y}_l(n) - \sum_{i=1, i\neq d}^{D} \hat{b}_{il}\hat{\mathcal{H}}_{il}\hat{\mathbf{a}}_i e^{j\hat{\omega}_{il}n}, \quad l = 0, \cdots, L-1, \quad n = P, \cdots, N-1, \qquad (2.13)$$

where $\{\hat{\omega}_i, \hat{\mathbf{a}}_i, \{\hat{b}_{il}\}_{l=0}^{L-1}\}_{i=d, i\neq d}^{D}$ is assumed available. Note that if the array manifold is known, $\hat{\mathbf{a}}_i$ is replaced by $\mathbf{a}(\hat{\theta}_i)$, with $\{\hat{\theta}_i\}_{i=1, i\neq d}^{D}$ assumed available. Hence $\mathbf{y}_{dl}(n)$ can be written as

$$\mathbf{y}_{dl}(n) = \bar{\alpha}_{dl}e^{j\omega_{dl}n} + \epsilon_{dl}(n), \quad l = 0, \cdots, L-1, \quad n = P, \cdots, N-1, \qquad (2.14)$$

where $\epsilon_{dl}(n)$ denotes the interference due to clutter, noise, and contributions from other targets. We assume that $\{\epsilon_{dl}(n)\}$ is a zero-mean temporally white Gaussian random process with an unknown arbitrary spatial covariance matrix $\mathbf{Q}_d$. Then the negative log-likelihood function of $\mathbf{y}_{dl}(n)$ in (2.14), is proportional to

$$C_2 = \ln|\mathbf{Q}_d| + \text{Tr}\left(\mathbf{Q}_d^{-1}\mathbf{C}_d\right), \qquad (2.15)$$

where $|\cdot|$ and $\text{Tr}(\cdot)$ denote, respectively, the determinant and the trace of a matrix and

$$\begin{aligned}
\mathbf{C}_d &= \frac{1}{\tilde{N}L}\sum_{l=0}^{L-1}\sum_{n=P}^{N-1}\left[\mathbf{y}_{dl}(n) - \bar{\alpha}_{dl}e^{j\omega_{dl}n}\right]\left[\mathbf{y}_{dl}(n) - \bar{\alpha}_{dl}e^{j\omega_{dl}n}\right]^H \\
&= \frac{1}{\tilde{N}L}\sum_{l=0}^{L-1}\left[\mathbf{Y}_{dl} - \bar{\alpha}_{dl}\beta_{dl}^H\right]\left[\mathbf{Y}_{dl} - \bar{\alpha}_{dl}\beta_{dl}^H\right]^H,
\end{aligned} \qquad (2.16)$$

with

$$\mathbf{Y}_{dl} = [\mathbf{y}_{dl}(P) \cdots \mathbf{y}_{dl}(N-1)], \quad l = 0, \cdots, L-1, \qquad (2.17)$$

and

$$\beta_{dl} = \left[e^{j\omega_{dl}P} \cdots e^{j\omega_{dl}(N-1)} \right]^H, \quad l = 0, \cdots, L-1. \tag{2.18}$$

Minimizing C_2 in (2.15) with respect to $\mathbf{Q}_d$ results in $\hat{\mathbf{Q}}_d = \mathbf{C}_d$. The cost function in (2.15) with $\mathbf{Q}_d$ replaced by $\hat{\mathbf{Q}}_d$ becomes:

$$
\begin{aligned}
C_3 &= \ln |\mathbf{C}_d| \\
&= \ln \left| \frac{1}{\tilde{N}L} \sum_{l=0}^{L-1} \left[\tilde{N} \left(\bar{\alpha}_{dl} - \frac{\mathbf{Y}_{dl}\beta_{dl}}{\tilde{N}} \right) \left(\bar{\alpha}_{dl} - \frac{\mathbf{Y}_{dl}\beta_{dl}}{\tilde{N}} \right)^H + \mathbf{Y}_{dl}\mathbf{Y}_{dl}^H - \frac{\mathbf{Y}_{dl}\beta_{dl}\beta_{dl}^H\mathbf{Y}_{dl}^H}{\tilde{N}} \right] \right|.
\end{aligned}
\tag{2.19}
$$

The minimization of C_3 in (2.19) with respect to $\bar{\alpha}_{dl}$ gives

$$\hat{\bar{\alpha}}_{dl} = \frac{1}{\tilde{N}} \mathbf{Y}_{dl}\beta_{dl} \Big|_{\omega_{dl} = \hat{\omega}_d(1+rl)}, \quad l = 0, \cdots, L-1. \tag{2.20}$$

The estimate of the Doppler frequency ω_d of the dth target is obtained by minimizing the concentrated cost function,

$$C_4 = \ln \left| \frac{1}{\tilde{N}L} \sum_{l=0}^{L-1} \left[\mathbf{Y}_{dl}\mathbf{Y}_{dl}^H - \frac{\mathbf{Y}_{dl}\beta_{dl}\beta_{dl}^H\mathbf{Y}_{dl}^H}{\tilde{N}} \right] \right|, \tag{2.21}$$

which requires a 1-D search. Note that the spatial signature estimate in (2.20) can be interpreted as the temporal average of the Doppler shift and range migration compensated VAR filtered spatial measurements.

The estimate $\hat{\mathbf{Q}}_d$ of the covariance matrix $\mathbf{Q}_d$ of the VAR filtered interference sequence can be written as

$$\hat{\mathbf{Q}}_d = \frac{1}{\tilde{N}L} \sum_{l=0}^{L-1} \left[\mathbf{Y}_{dl}\mathbf{Y}_{dl}^H - \tilde{N}\hat{\bar{\alpha}}_{dl}\hat{\bar{\alpha}}_{dl}^H \right]. \tag{2.22}$$

Given $\{\hat{\bar{\alpha}}_{dl}\}_{l=0}^{L-1}$ and $\hat{\mathbf{Q}}_d$, the estimates of $\{b_{dl}\}_{l=0}^{L-1}$ and DOA θ_d (if the array manifold is known) or $\mathbf{a}_d$ (if the array manifold is unknown) can be obtained by minimizing the following Weighted Least Squares (WLS) cost function,

$$C_5 = \sum_{l=0}^{L-1} \left(\hat{\bar{\alpha}}_{dl} - b_{dl}\hat{\mathcal{H}}_{dl}\mathbf{a}_d \right)^H \hat{\mathbf{Q}}_d^{-1} \left(\hat{\bar{\alpha}}_{dl} - b_{dl}\hat{\mathcal{H}}_{dl}\mathbf{a}_d \right). \tag{2.23}$$

11

Note that this cost function is similar to the one used for the unstructured method in [1] since the Fisher information matrix (FIM) for $\bar{\alpha}_{dl}$ in (2.14) is also proportional to $\mathbf{Q}_d^{-1}$ (see [1] for more details).

Method 1: To estimate θ_d, we must know the array manifold $\mathbf{a}(\theta_d)$ as a function of θ_d. The method for estimating $\{b_{dl}\}_{l=0}^{L-1}$ and θ_d by using the array manifold is referred to as Method 1. Without loss of generality, we consider a uniform linear array (ULA), where $\mathbf{a}(\theta_d)$ has the form,

$$\mathbf{a}(\theta_d) = \begin{bmatrix} 1 & e^{j\frac{2\pi\zeta}{\lambda}\cos\theta_d} & \cdots & e^{j(M-1)\frac{2\pi\zeta}{\lambda}\cos\theta_d} \end{bmatrix}^T, \qquad (2.24)$$

with λ being the radar wavelength and ζ being the spacing between two adjacent sensors. Minimizing C_5 in (2.23) gives

$$\hat{b}_{dl} = \frac{\mathbf{a}_d^H \hat{\mathcal{H}}_{dl}^H \hat{\mathbf{Q}}_d^{-1} \hat{\bar{\alpha}}_{dl}}{\mathbf{a}_d^H \hat{\mathcal{H}}_{dl}^H \hat{\mathbf{Q}}_d^{-1} \hat{\mathcal{H}}_{dl} \mathbf{a}_d}, \quad l = 0, \cdots, L-1, \qquad (2.25)$$

and

$$\hat{\theta}_d = \arg\max_{\theta_d} \sum_{l=0}^{L-1} \frac{\left| \mathbf{a}_d^H \hat{\mathcal{H}}_{dl}^H \hat{\mathbf{Q}}_d^{-1} \hat{\bar{\alpha}}_{dl} \right|^2}{\mathbf{a}_d^H \hat{\mathcal{H}}_{dl}^H \hat{\mathbf{Q}}_d^{-1} \hat{\mathcal{H}}_{dl} \mathbf{a}_d}. \qquad (2.26)$$

Once $\hat{\theta}_d$ is determined, $\{\hat{b}_{dl}\}_{l=0}^{L-1}$ is obtained with (2.25) by replacing $\mathbf{a}_d$ with $\mathbf{a}(\hat{\theta}_d)$.

Method 2: To achieve robustness against array calibration errors, we can assume that $\mathbf{a}_d$ is completely unknown. The corresponding method used to estimate both $\{b_{dl}\}_{l=0}^{L-1}$ and $\mathbf{a}_d$ is referred to as Method 2. Note that since replacing $\{b_{dl}\}_{l=0}^{L-1}$ by $\{\beta b_{dl}\}_{l=0}^{L-1}$ and $\mathbf{a}_d$ by $\mathbf{a}_d/\beta$ in (2.23), where β is any non-zero complex scalar, does not change C_5, $\{b_{dl}\}_{l=0}^{L-1}$ and $\mathbf{a}_d$ can only be determined up to an unknown multiplicative complex constant. This unknown complex scalar, similar to the unknown gain and initial phase of a radar system, does not affect most practical applications such as ATR. C_5 (see below).

Given $\{b_{dl}\}_{l=0}^{L-1}$, minimizing C_5 in (2.23) with respect to $\mathbf{a}_d$ yields

$$\hat{\mathbf{a}}_d = \left[\sum_{l=0}^{L-1} |b_{dl}|^2 \hat{\mathcal{H}}_{dl}^H \hat{\mathbf{Q}}_d^{-1} \hat{\mathcal{H}}_{dl} \right]^{-1} \sum_{l=0}^{L-1} b_{dl}^* \hat{\mathcal{H}}_{dl}^H \hat{\mathbf{Q}}_d^{-1} \hat{\bar{\alpha}}_{dl}, \qquad (2.27)$$

12

where $(\cdot)^*$ denotes the complex conjugate. Given $\mathbf{a}_d$, $\{b_{dl}\}_{l=0}^{L-1}$ can be estimated by using (2.25). Hence we can cyclically iterate (2.25) and (2.27) to obtain the estimates of $\{b_{dl}\}_{l=0}^{L-1}$ and $\mathbf{a}_d$.

To start the iteration, we must have an initial estimate of either $\mathbf{a}_d$ or $\{b_{dl}\}_{l=0}^{L-1}$. Our initialization approach is obtained by using the Singular Value Decomposition (SVD) [8]. Rewriting C_5 in (2.23), we have

$$C_6 = \sum_{l=0}^{L-1} \left(\hat{\mathcal{H}}_{dl}^{-1} \hat{\tilde{\alpha}}_{dl} - b_{dl}\mathbf{a}_d \right)^H \hat{\mathbf{Q}}_{dl} \left(\hat{\mathcal{H}}_{dl}^{-1} \hat{\tilde{\alpha}}_{dl} - b_{dl}\mathbf{a}_d \right), \tag{2.28}$$

where

$$\hat{\mathbf{Q}}_{dl} = \hat{\mathcal{H}}_{dl}^H \hat{\mathbf{Q}}_d^{-1} \hat{\mathcal{H}}_{dl}, \quad l = 0, \cdots, L-1. \tag{2.29}$$

To place the most weight on the term that is associated with the largest signal energy, we choose $\mathbf{W}_d = \hat{\mathbf{Q}}_{dl_0}$, where l_0 is selected such that $\left\| \hat{\mathcal{H}}_{dl_0}^{-1} \hat{\tilde{\alpha}}_{dl_0} \right\|$ is the largest among $\left\{ \left\| \hat{\mathcal{H}}_{dl}^{-1} \hat{\tilde{\alpha}}_{dl} \right\| \right\}_{l=0}^{L-1}$. Let

$$\check{\alpha}_{dl} = \mathbf{W}_d^{\frac{1}{2}} \hat{\mathcal{H}}_{dl}^{-1} \hat{\tilde{\alpha}}_{dl}, \tag{2.30}$$

and

$$\check{\mathbf{a}}_d = \mathbf{W}_d^{\frac{1}{2}} \mathbf{a}_d. \tag{2.31}$$

We minimize the following approximate cost function

$$C_7 = \sum_{l=0}^{L-1} \left(\check{\alpha}_{dl} - b_{dl}\check{\mathbf{a}}_d \right)^H \left(\check{\alpha}_{dl} - b_{dl}\check{\mathbf{a}}_d \right), \tag{2.32}$$

which is equivalent to

$$C_8 = \left\| \check{\mathbf{A}}_d - \check{\mathbf{a}}_d \mathbf{b}_d^T \right\|_F^2, \tag{2.33}$$

where $\| \cdot \|_F$ denotes the Frobenius norm,

$$\mathbf{b}_d = [b_{d0} \quad \cdots \quad b_{d(L-1)}]^T, \tag{2.34}$$

and

$$\check{\mathbf{A}}_d = \begin{bmatrix} \check{\alpha}_{d0} & \cdots & \check{\alpha}_{d(L-1)} \end{bmatrix}. \tag{2.35}$$

13

The C_8 in (2.33) is minimized if

$$\check{\mathbf{a}}_d \mathbf{b}_d^T = \mathbf{u}_{d1} \sigma_{d1} \mathbf{v}_{d1}^H, \tag{2.36}$$

where $\mathbf{u}_{d1}$ and $\mathbf{v}_{d1}$ are, respectively, the left and right singular vectors associated with the largest singular value σ_{d1} of $\check{\mathbf{A}}_d$. Then either the initial estimate of $\mathbf{b}_d$, i.e.,

$$\hat{\mathbf{b}}_d^{(0)} = \mathbf{v}_{d1}^*, \tag{2.37}$$

or the initial estimate of $\mathbf{a}_d$, i.e.,

$$\hat{\mathbf{a}}_d^{(0)} = \mathbf{W}_d^{-\frac{1}{2}} \mathbf{u}_{d1}, \tag{2.38}$$

can be used to initialize the alternating optimization approach. We use the one in (2.37) in our numerical examples. The steps of Method 2 are summarized as follows:

Step (0): Obtain the initial estimate $\hat{\mathbf{b}}_d^{(0)}$ of $\mathbf{b}_d$ with (2.37).

Step (1): Update $\{\hat{b}_{dl}\}_{l=0}^{L-1}$ with (2.25) by replacing $\mathbf{a}_d$ in (2.25) with the most recently determined $\hat{\mathbf{a}}_d$.

Step (2): Update $\hat{\mathbf{a}}_d$ with (2.27) by replacing $\{b_{dl}\}_{l=0}^{L-1}$ in (2.27) with the most recently determined $\{\hat{b}_{dl}\}_{l=0}^{L-1}$.

Step (3): Iterate **Steps (1)** and **(2)** until practical convergence, which is determined by checking the relative change ξ of the cost function C_5 in (2.23) between two consecutive iterations.

We remark that if the range migration is negligible, i.e., $r = 0$ in (2.2), then $\{\hat{\mathcal{H}}_{dl}\}_{l=0}^{L-1}$ in (2.8) do not depend on l. Then **Step (0)** alone gives the solution that minimizes the C_5 in (2.23).

Summary of the Steps of Space-Time Parameter Estimation

The space-time parameter estimates $\{\hat{\omega}_d, \hat{\theta}_d \text{ (or } \hat{\mathbf{a}}_d), \hat{\mathbf{b}}_d\}_{d=1}^D$ of the multiple moving targets can be obtained as follows:

Step I.1: Assume $D = 1$. Obtain $\{\hat{\omega}_d, \hat{\theta}_d \text{ (or } \hat{\mathbf{a}}_d), \hat{\mathbf{b}}_d\}_{d=1}$ from $\mathbf{y}_l(n)$.

Step I.2: Assume $D = 2$. Compute $\mathbf{y}_{2l}(n)$ with (2.13) using $\{\hat{\omega}_d, \hat{\theta}_d \text{ (or } \hat{\mathbf{a}}_d), \hat{\mathbf{b}}_d\}_{d=1}$ obtained in **Step I.1**. Obtain $\{\hat{\omega}_d, \hat{\theta}_d \text{ (or } \hat{\mathbf{a}}_d), \hat{\mathbf{b}}_d\}_{d=2}$ from $\mathbf{y}_{2l}(n)$. Next, compute $\mathbf{y}_{1l}(n)$ with

14

(2.13) using $\{\hat{\omega}_d, \hat{\theta}_d \text{ (or } \hat{a}_d), \hat{b}_d\}_{d=2}$ and then re-determine $\{\hat{\omega}_d, \hat{\theta}_d \text{ (or } \hat{a}_d), \hat{b}_d\}_{d=1}$ from $y_{1l}(n)$. Iterate the previous two substeps until "practical convergence" is achieved (to be discussed later on).

Step I.3: Assume $D = 3$. Compute $y_{3l}(n)$ with (2.13) using $\{\hat{\omega}_d, \hat{\theta}_d \text{ (or } \hat{a}_d), \hat{b}_d\}_{d=1,2}$ obtained in **Step I.2**. Obtain $\{\hat{\omega}_d, \hat{\theta}_d \text{ (or } \hat{a}_d), \hat{b}_d\}_{d=3}$ from $y_{3l}(n)$. Next, compute $y_{1l}(n)$ with (2.13) using $\{\hat{\omega}_d, \hat{\theta}_d \text{ (or } \hat{a}_d), \hat{b}_d\}_{d=2,3}$ and then re-determine $\{\hat{\omega}_d, \hat{\theta}_d \text{ (or } \hat{a}_d), \hat{b}_d\}_{d=1}$ from $y_{1l}(n)$. Then, compute $y_{2l}(n)$ with (2.13) using $\{\hat{\omega}_d, \hat{\theta}_d \text{ (or } \hat{a}_d), \hat{b}_d\}_{d=1,3}$ and re-determine $\{\hat{\omega}_d, \hat{\theta}_d \text{ (or } \hat{a}_d), \hat{b}_d\}_{d=2}$ from $y_{2l}(n)$. Iterate the above three substeps until "practical convergence" is reached.

Remain Steps: Continue similarly until D is equal to the desired or estimated number of targets, which is assumed to be known or can be determined by using the Generalized Akaike Information Criterion (GAIC) [5, 9]. $d = 1, \cdots, D$.

The "practical convergence" in the iterations of the above algorithm can be determined by checking the relative change ϵ of the cost function C_1 in (2.12) between two consecutive iterations. The steps leading to the last step are needed to provide good initial conditions for the last step of the algorithm.

Estimating the target range features $\{\hat{\alpha}_{dk}, \hat{f}_{dk}\}_{k=1}^{K_d}$ from $\hat{b}_d$, $d = 1, \cdots, D$, is our next concern.

2.3.2 Target Range Feature Estimation

Once the sequences $\{\hat{b}_{dl}\}_{l=0}^{L-1}$, $d = 1, \cdots, D$, for all targets are available, the range feature estimates, $\{\hat{\alpha}_{dk}, \hat{f}_{dk}\}_{k=1}^{K_d}$, $d = 1, \cdots, D$, can be obtained by minimizing the following cost function,

$$C_9(\{\alpha_{dk}, f_{dk}\}_{k=1}^{K_d}) = \|\hat{b}_d - F_d \alpha_d\|^2, \quad d = 1, \cdots, D, \tag{2.39}$$

where $\hat{b}_{dl}$ is the lth element of vector $\hat{b}_d$,

$$\alpha_d = [\alpha_{d1} \quad \cdots \quad \alpha_{dK_d}]^T, \quad d = 1, \cdots, D,$$

and

$$\mathbf{F}_d = [\mathbf{f}_{d1} \quad \cdots \quad \mathbf{f}_{dK_d}], \ d = 1, \cdots, D,$$

with

$$\mathbf{f}_{dk} = \begin{bmatrix} 1 & e^{j2\pi f_{dk}} & \cdots & e^{j2\pi f_{dk}(L-1)} \end{bmatrix}^T, \ d = 1, \cdots, D, \ k = 1, \cdots, K_d.$$

The estimates $\{\hat{\alpha}_{dk}, \hat{f}_{dk}\}_{k=1}^{K_d}$ of $\{\alpha_{dk}, f_{dk}\}_{k=1}^{K_d}$ can be obtained by using the RELAX algorithm (see [5] for more details), which has a similar structure as the approach used for space-time parameter estimation.

We remark that our multiple moving target feature extraction algorithm above may have used more unknowns than necessary at certain steps. We choose to do so to simplify and speed up the algorithm. For example, to use the relaxation-based optimization algorithm, we could estimate both the space-time and the range parameters of the dth target and subtract out the dth target based on the parameter estimates $\{\hat{\omega}_d, \ \hat{\theta}_d \text{ (or } \hat{\mathbf{a}}_d), \{\hat{\alpha}_{dk}, \ \hat{f}_{dk}\}_{k=1}^{K_d}\}_{d=1}^{D}$ for the iteration steps. However, since estimating the range parameters $\{\hat{\alpha}_{dk}, \ \hat{f}_{dk}\}_{k=1}^{K_d}$ can be computationally demanding, we choose to separate the range parameter estimation from the space-time parameter estimation. Our numerical results have shown little accuracy degradation but reduced computations, especially for large K_d, as a result of the separate space-time and range parameter estimation.

2.4 Numerical Examples

We present several numerical examples to illustrate the performance of our proposed algorithm. In the following examples, we assume that the array is a ULA with $M = 8$; the interelement distance between two antennas is $\zeta = \lambda/2$; the number of pulses in a CPI is $N = 16$; the phase history sample number is $L = 16$, i.e., an LRR range segment contains 16 HRR range bins. Consider two targets ($D = 2$) with DOAs $\theta_1 = 30°$ and $\theta_2 = 150°$, and Doppler frequencies $\omega_1 = 0.2\pi$ and $\omega_2 = 0.4\pi$ with $r = 0.01$. Each of the two targets consists of two closely spaced scatterers ($K_1 = K_2 = 2$) with parameters $\alpha_{11} = 1$, $\alpha_{12} = 1$, $\alpha_{21} = 1$, $\alpha_{22} = 1$, $f_{11} = 0.1$, $f_{12} = 0.1 + 1/2L$, $f_{21} = 0.3$, and $f_{22} = 0.3 + 1/2L$, where the subscript ij means the jth scatterer of the ith target. The VAR filter order is $P = 2$. (No

16

obvious performance improvement is obtained by higher orders.) The number of secondary range bins is $S = 4$. We set $\epsilon = \xi = 10^{-3}$ to determine the "practical convergence" in the simulations. The mean-squared errors (MSEs) of the various estimates are obtained from 100 Monte Carlo trials.

We simulate the ground clutter as a temporally and spatially correlated Gaussian random process [10]. The Clutter-to-Noise Ratio (CNR), defined as the ratio of the clutter variance to the noise variance, is set to be CNR= 40 dB. A jamming signal, which is a zero-mean temporally white Gaussian random process, also exists. The Jammer-to-Noise Ratio (JNR), which is the ratio of the jammer's temporal variance to the noise variance, is chosen as JNR= 25 dB and the jamming impinges from $\theta_J = 120°$. When array calibration errors exist, the errors for different elements are assumed to be independent and identically distributed complex Gaussian random variables. In our simulations, a complex Gaussian random vector with zero-mean and covariance matrix $0.04\mathbf{I}$ is added to the array manifold to simulate array calibration errors, which implies that the variance of the calibration error for each element is 0.04.

We first present an example of no array calibration errors. Note that the complex amplitude estimates $\{\hat{\alpha}_{dk}\}_{k=1}^{K_d}$ of $\{\alpha_{dk}\}_{k=1}^{K_d}$ obtained via Method 2 are all scaled by a common unknown complex scalar. To calculate their best possible MSEs, we scale them to minimize

$$C_{10} = \|\boldsymbol{\alpha}_{d0} - \beta\boldsymbol{\alpha}_d\|^2, \qquad (2.40)$$

where $\boldsymbol{\alpha}_{d0}$ is the true value of $\boldsymbol{\alpha}_d$. Minimizing (2.40) with respect to β yields:

$$\beta = \frac{\hat{\boldsymbol{\alpha}}_d^H \boldsymbol{\alpha}_{d0}}{\|\hat{\boldsymbol{\alpha}}_d^H\|^2}. \qquad (2.41)$$

Note that this scaling scheme is only used to illustrate the complex amplitude estimate performance; it is not a necessary step in a practical application including ATR since only the relative amplitudes are of interest. For comparison purposes, the MSEs of the estimates $\{\hat{\alpha}_{dk}\}_{k=1}^{K_d}$ obtained via Method 1 are presented both with and without a scaling scheme similar to (2.40).

17

Figures 2.2(a)-2.2(d) show the MSEs of the estimates of the Doppler frequency, target DOA, complex amplitude, and range frequency of the first scatterer of the first target as a function of Signal-to-Noise Ratio (SNR), which is defined as the ratio of $|\alpha_{11}|^2$ to the noise variance, and compare them with the corresponding Cramér-Rao bounds (CRBs) (see Appendix B for the CRB derivation). (The results for the other scatterer and the other target are similar.) Due to using the scaling scheme in (2.40), the MSEs of $\{\hat{\alpha}_{dk}\}_{k=1}^{K_d}$ may be better than the CRBs (which do not account for such a scaling). We note that as the SNR increases, the MSEs can approach the corresponding CRBs, which indicates that the clutter suppression scheme works well and the parameter estimation algorithm is highly accurate.

Next, we present an example when the array calibration errors exist. All other parameters are kept the same as for Figure 2.2. Figures 2.3(a)-2.3(d) show the MSEs of the estimates of the Doppler frequency, target DOA, complex amplitude, and range frequency of the first scatterer of the first target, as a function of SNR. Note that the MSEs of the complex amplitude and range frequency estimates obtained via Method 2 are close to the CRBs as the SNR increases, while the MSEs of the complex amplitude estimates for Method 1 fail to follow the CRBs if the scaling scheme is not used, though the range frequency is still well estimated via Method 1. Hence from Figure 2.3, we note that both Methods 1 and 2 are robust against calibration errors as far as the Doppler frequency, relative complex amplitude, and range frequency of the scatterer are concerned.

rigid-body moving $\omega_2 = 0.4\pi$, DOAs, and $\{b_k, \theta_k, \omega_k\}_{k=1,2}$ primary data

We remark that the above simulation results show that Methods 1 and 2 provide similar performances for target relative complex amplitude and range frequency estimation. Method 2 avoids the 1-D search over the DOA space and usually requires only a few ($3 \sim 6$) iterations. To estimate the target phase history sequence $\{b_{1l}\}_{l=0}^{L-1}$ from the spatial signature estimates $\{\hat{\alpha}_{1l}\}_{l=0}^{L-1}$, Method 2 needs only about $10\% \sim 30\%$ of the amount of computations measured in MATLAB flops required by Method 1. (This difference is mainly due to the fact that the latter requires a 1-D search over the DOA space.) Hence if the array calibration errors are known to be significant enough to result in a useless target DOA estimate or if the target DOA is not of interest, Method 2 is preferred over Method 1.

2.5 Conclusions

We have presented a robust and accurate method for the clutter suppression and feature extraction of multiple moving targets for airborne HRR phased array radar. To avoid the range migration problems that occur in HRR radar data, we divided the HRR range profiles into LRR segments. We have shown how to use the VAR filtering technique to suppress the ground clutter and use the relaxation-based algorithm to extract the features of multiple moving targets. The multiple moving target feature extraction problem is reduced to the feature extractions of a single moving target in a relaxation-based iteration step. For each target and in each iteration, the target phase history sequence and DOA (or the unknown array manifold) are estimated from the spatial signature vectors by minimizing a Weighted Least Squares (WLS) cost function. Numerical results have demonstrated that our multiple moving target feature extraction algorithm performs well in the presence of strong interference including clutter, noise, and jammer and is robust against array calibration errors.

Appendix A: Data Model Derivation

We sketch below the derivation of the data model used in (2.3). We first establish the data model for the case of a single antenna, then extend it to the case of the phased array radar.

Assume that the radar transmits a group of chirp pulses with the pulse width T_0 and the pulse repetition interval (PRI) T. A normalized chirp signal has the form

$$s(t) = e^{-j\left(2\pi f_0 t + \gamma t^2\right)}, \quad |t| \leq T_0/2, \tag{2.42}$$

where f_0 denotes the carrier frequency and 2γ denotes the frequency modulation rate. First, we assume that there are D targets with different DOAs, radial velocities, and RCSs. At time t, the range of the dth target is $R_d(t) = R_d + v_d t$, $d = 1, \cdots, D$, where R_d and V_d denote the range location and radial velocity of the dth target, respectively, when the first pulse was transmitted.

19

Let $\tilde{t} = t - nT$ denote the *fast time*, where n is the pulse number. Then the received signal from the dth target is:

$$r_d(t) = \tilde{\alpha}_d \exp\left\{ j\left[2\pi f_0 \left(\tilde{t} - \tau_0 - \Delta\tau_d - \frac{2V_d t}{c} \right) + \gamma \left(\tilde{t} - \tau_0 - \Delta\tau_d - \frac{2V_d t}{c} \right)^2 \right] \right\},$$
$$|\tilde{t}| \le T_0/2, \quad n = 0, 1, \cdots, N-1, \tag{2.43}$$

where $\tilde{\alpha}_d$ is determined by the RCS of the dth target, $\tau_0 = 2R_0/c$, $\Delta\tau_d = 2(R_d - R_0)/c$ with R_0 denoting a reference range (possibly corresponding to the center of the target), c is the speed of light, and N is the total number of pulses transmitted in a CPI. By using $s(\tilde{t} - \tau_0)$, with $|\tilde{t} - \tau_0| \le T_0/2$, as the reference signal, the dechirped signal has the form:

$$\begin{aligned}
\bar{x}_d(t, n) &= r_d(t) s^*(t - \tau_0) \\
&= \tilde{\alpha}_d \exp\left[-j 2\pi f_0 \left(\Delta\tau_d + \frac{2V_d t}{c} \right) \right] \\
&\quad \cdot \exp\left[-j\gamma \left(2\tilde{t} - 2\tau_0 - \Delta\tau_d - \frac{2V_d t}{c} \right) \left(\Delta\tau_d + \frac{2V_d t}{c} \right) \right].
\end{aligned} \tag{2.44}$$

Since V_d/c and $\Delta\tau_d$ tend to be very small in practice, when the dwell time, $(N-1)T$, is short, we can approximately express (2.44) as:

$$\begin{aligned}
\bar{x}_d(\tilde{t}, n) &\approx \alpha_d \exp\left[-j\left(\frac{4\pi V_d}{\lambda} + \frac{4\gamma\tau_0 V_d}{c} + 2\gamma\Delta\tau_d \right) \tilde{t} \right] \exp\left[-j\left(\frac{4\pi}{\lambda} - \frac{4\gamma\tau_0}{c} \right) vTn \right] \\
&\quad \exp\left(-j\frac{4\gamma V_d T}{c} \tilde{t}n \right), \quad d = 1, \cdots, D, \quad n = 0, 1, \cdots, N-1, \tag{2.45}
\end{aligned}$$

where λ denotes the radar wavelength, and α_d is $\tilde{\alpha}_d$ scaled by a constant phase. Note that, in (2.45) above, the first exponential term, a linear function of $\tilde{t}$, corresponds to the phase change of the signal due to the dth target within a chirp pulse, which is caused by the relative range and target velocity; the second one accounts for the phase shift (Doppler shift) between pulses, which is due to the radial velocity of the dth target; finally, the last term represents the accumulated phase shift from profile to profile, i.e., range migration.

We assume that $2(R_{\max} - R_{\min})/c \ll T_0$, where $R_{\max}$ and $R_{\min}$ denote the maximum and minimum ranges between the radar and target scatterers, respectively. Let T_s denote

20

the sampling period. Then we can express the sampled dechirped signal as

$$\bar{x}_l(n) = \sum_{d=1}^{D} \alpha_d e^{j2\pi f_d l} e^{jv_d nl} e^{j\omega_d n}, \quad n = 0, \cdots, N-1, \quad l = 0, \cdots, L-1, \qquad (2.46)$$

where L denotes the number of data samples due to each pulse,

$$f_d = - \left(\frac{2V_d}{\lambda} + \frac{2\gamma\tau_0 V_d}{\pi c} + \frac{\gamma\Delta\tau_d}{\pi} \right) T_s, \qquad (2.47)$$

$$\omega_d = 2\pi V_d T \left(\frac{2\gamma\tau_0}{\pi c} - \frac{2}{\lambda} \right), \qquad (2.48)$$

and

$$v_d = -\frac{4\gamma V_d T T_s}{c}. \qquad (2.49)$$

Since both v_d and ω_d depend on the relative speed between the radar and the target, if ω_d is known, so is v_d, and vice versa. Defining $v_d = r\omega_d$, we have:

$$r = \frac{v_d}{\omega_d} = \frac{\gamma T_s}{\pi f_0 - \gamma\tau_0}, \qquad (2.50)$$

which is independent of the target velocity.

For an HRR phased array radar with the array manifold $\mathbf{a}(\theta_d)$, (2.46) becomes

$$\mathbf{x}_l(n) = \sum_{d=1}^{D} \left(\alpha_d e^{j2\pi f_d l} e^{jv_d nl} e^{j\omega_d n} \right) \mathbf{a}(\theta_d), \quad n = 0, \cdots, N-1, \quad l = 0, \cdots, L-1. \qquad (2.51)$$

Here, we assume D rigid-body targets with K_d scatterers for the dth target. We also assume that the scatterers of the same target have the same DOA. Straightforwardly, (2.51) has the form

$$\mathbf{x}_l(n) = \sum_{d=1}^{D} \left(\sum_{k=1}^{K_d} \alpha_{dk} e^{j2\pi f_{dk} l} \right) e^{jv_d nl} e^{j\omega_d n} \mathbf{a}(\theta_d), \quad n = 0, \cdots, N-1, \quad l = 0, \cdots, L-1, \qquad (2.52)$$

where $\{\alpha_{dk}, f_{dk}, v_d, \omega_d\}$ are the parameters of the kth scatterer of the dth target. Finally, when the interference is included, we obtain the data model in (2.1).

Appendix B: Derivation of the CRBs

The CRB matrix corresponding to the data model in (2.1) is derived for the general case in which the interference term $\mathbf{e}_l(n)$ includes clutter, jamming, and noise.

Rewrite (2.1) as,

$$\chi = \sum_{d=1}^{D} \left(\sum_{k=1}^{K_d} \alpha_{dk} \omega_{dk}^s \right) \otimes \omega_d^f \odot \omega_d^r \otimes \mathbf{a}_d + \mathbf{e} \in \mathcal{C}^{MNL \times 1}, \qquad (2.53)$$

where $\otimes$ and $\odot$ denote the Kronecker and Hadamard matrix products, respectively,

$$\omega_{dk}^s = \begin{bmatrix} 1 & e^{j2\pi f_{dk}} & \cdots & e^{j2\pi f_{dk}(L-1)} \end{bmatrix}^T, \qquad (2.54)$$

$$\omega_d^f = \begin{bmatrix} 1 & e^{j\omega_d} & \cdots & e^{j\omega_d(N-1)} \end{bmatrix}^T, \qquad (2.55)$$

and

$$\omega_d^r = \begin{bmatrix} \bar{\mathbf{f}}_d^T(0) & \bar{\mathbf{f}}_d^T(1) & \cdots & \bar{\mathbf{f}}_d^T(L-1) \end{bmatrix}^T, \qquad (2.56)$$

with

$$\bar{\mathbf{f}}_d(l) = \begin{bmatrix} 1 & e^{j\omega_d rl} & \cdots & e^{j\omega_d rl(N-1)} \end{bmatrix}^T, \quad l = 0, \cdots, L-1. \qquad (2.57)$$

Let $\mathbf{Q}_N$, $\mathbf{Q}_C$, and $\mathbf{Q}_J$ be, respectively, the covariance matrices of the noise, ground clutter, and jamming, which are independent of each other. Then

$$\mathbf{Q} = E\{\mathbf{e}\mathbf{e}^H\} = \mathbf{Q}_N + \mathbf{Q}_C + \mathbf{Q}_J, \qquad (2.58)$$

where

$$\mathbf{Q}_N = \sigma_N^2 \mathbf{I}_{MNL}, \qquad (2.59)$$

$$\mathbf{Q}_C = \sigma_C^2 \mathbf{I}_L \otimes \mathbf{Q}_c, \qquad (2.60)$$

and

$$\mathbf{Q}_J = \sigma_J^2 \mathbf{I}_{NL} \otimes (\mathbf{a}_J \mathbf{a}_J^H), \qquad (2.61)$$

with σ_N^2, σ_C^2, and σ_J^2 being, respectively, the variances of the noise, clutter, and jamming, $\mathbf{I}_L$ being the identity matrix of dimension L, $\mathbf{Q}_c$ being as given in [10], and $\mathbf{a}_J$ denoting the jammer steering vector which has the same form as $\mathbf{a}(\theta_d)$ in (2.24) except that θ_d in (2.24) is replaced by the jammer DOA θ_J.

According to the extended Slepian-Bangs' formula, the ijth element of the Fisher information matrix (FIM) has the form [11, 12]

$$\{\text{FIM}\}_{ij} = \text{Tr}\left(\mathbf{Q}^{-1}\frac{\partial \mathbf{Q}}{\partial \eta_i}\mathbf{Q}^{-1}\frac{\partial \mathbf{Q}}{\partial \eta_j}\right) + 2\text{Re}\left[\left(\frac{\partial \boldsymbol{\chi}}{\partial \eta_i}\right)^H \mathbf{Q}^{-1}\left(\frac{\partial \boldsymbol{\chi}}{\partial \eta_i}\right)\right], \qquad (2.62)$$

where

$$\boldsymbol{\eta} = \left[\ \text{Re}^T(\boldsymbol{\alpha})\ \ \text{Im}^T(\boldsymbol{\alpha})\ \ \mathbf{f}^T\ \ \boldsymbol{\omega}\ \ \boldsymbol{\theta}\ \right]^T, \qquad (2.63)$$

with $\boldsymbol{\alpha}, \mathbf{f}, \boldsymbol{\omega}$, and $\boldsymbol{\theta}$ being the vectors consisting of the complex amplitudes, range frequencies, Doppler frequencies, and DOAs of the targets, respectively; $\left(\frac{\partial \mathbf{x}}{\partial \eta_i}\right)$ denotes the derivative of $\mathbf{x}$ with respect to the ith parameter of $\boldsymbol{\eta}$; $\text{Re}(x)$ is the real part of x and $\text{Im}(x)$ is the imaginary part of x. Note that the FIM is block diagonal since the parameters in $\mathbf{Q}$ are independent of those in $\boldsymbol{\mu}$ and vice versa. Hence, the CRB matrix for the target features and the motion parameters can be calculated from the second term on the right side of (2.62). Let

$$\mathbf{g}_{dk}^{\alpha_r} = \left[\left(\boldsymbol{\omega}_{dk}^s \otimes \boldsymbol{\omega}_d^f\right) \odot \boldsymbol{\omega}_d^r\right] \otimes \mathbf{a}_d, \qquad (2.64)$$

and

$$\mathbf{g}_{dk}^{\alpha_i} = j\mathbf{g}_{dk}^{\alpha_r}. \qquad (2.65)$$

Let

$$\mathbf{g}_d^f = j2\pi \left\{\left[\left(\sum_{k=1}^{K_d} \alpha_{dk}\mathbf{d}_L \odot \boldsymbol{\omega}_{dk}^s\right) \otimes \boldsymbol{\omega}_d^f\right] \odot \boldsymbol{\omega}_d^r\right\} \otimes \mathbf{a}_d, \qquad (2.66)$$

where $\mathbf{d}_L = [0\ 1\ \cdots\ L-1]^T$. Let

$$\mathbf{g}_d^\omega = j\left\{\left[\left(\sum_{k=1}^{K_d} \alpha_{dk}\boldsymbol{\omega}_{dk}^s\right) \otimes \boldsymbol{\omega}_d^f\right] \odot \left[(\mathbf{u}_L + r\mathbf{d}_L) \otimes \mathbf{d}_N\right] \odot \boldsymbol{\omega}_d^r\right\} \otimes \mathbf{a}_d, \qquad (2.67)$$

and

$$\mathbf{g}_d^\theta = \zeta_d\left[(\boldsymbol{\omega}_{dk}^s \otimes \boldsymbol{\omega}_d^f) \odot \boldsymbol{\omega}_d^r\right] \otimes (\mathbf{d}_M \odot \mathbf{a}_d), \qquad (2.68)$$

where $\mathbf{u}_L = [1\ \cdots\ 1]^T \in \mathcal{C}^{L \times 1}$ and $\zeta_d = -j(\pi^2/180)\sin(\theta_d\pi/180)$ with θ_d being measured in degrees. Let

$$\mathbf{G} = \left[\ \mathbf{G}_{\alpha_r}\ \ \mathbf{G}_{\alpha_i}\ \ \mathbf{G}_f\ \ \mathbf{G}_\omega\ \ \mathbf{G}_\theta\ \right], \qquad (2.69)$$

where

$$\mathbf{G}_{\alpha_r} = \begin{bmatrix} \mathbf{g}_{11}^{\alpha_r} & \cdots & \mathbf{g}_{1K_1}^{\alpha_r} & \cdots & \mathbf{g}_{D1}^{\alpha_r} & \cdots & \mathbf{g}_{DK_D}^{\alpha_r} \end{bmatrix},$$

$$\mathbf{G}_{\alpha_i} = j\mathbf{G}_{\alpha_r},$$

$$\mathbf{G}_f = \begin{bmatrix} \mathbf{g}_{11}^{f} & \cdots & \mathbf{g}_{1K_1}^{f} & \cdots & \mathbf{g}_{D1}^{f} & \cdots & \mathbf{g}_{DK_D}^{f} \end{bmatrix},$$

$$\mathbf{G}_\omega = \begin{bmatrix} \mathbf{g}_1^{\omega} & \cdots & \mathbf{g}_D^{\omega} \end{bmatrix},$$

and

$$\mathbf{G}_\theta = \begin{bmatrix} \mathbf{g}_1^{\theta} & \cdots & \mathbf{g}_D^{\theta} \end{bmatrix}.$$

Then the CRB matrix for the parameter vector $\boldsymbol{\eta}$ is given by

$$\mathrm{CRB}(\boldsymbol{\eta}) = \begin{bmatrix} 2\mathrm{Re}(\mathbf{G}^H \mathbf{Q}^{-1} \mathbf{G}) \end{bmatrix}^{-1}. \tag{2.70}$$

Reference

[1] A. L. Swindlehurst and P. Stoica, "Maximum likelihood methods in radar array signal processing," *Proceedings of the IEEE*, vol. 86, pp. 421–441, February 1998.

[2] D. C. Schleher, *MTI and Pulsed Doppler Radar*. Norwood, MA: Artech House, Inc., 1991.

[3] S. Hudson and D. Psaltis, "Correlation filters for aircraft identification from radar range profiles," *IEEE Transactions on Aerospace and Electronic Systems*, vol. 29, pp. 741–748, July 1993.

[4] S. P. Jacobs and J. A. O'Sullivan, "High resolution radar models for joint tracking and recognition," *IEEE National Conference on Radar, Syracuse, New York*, pp. 99–104, May 1997.

[5] J. Li and P. Stoica, "Efficient mixed-spectrum estimation with applications to target feature extraction," *IEEE Transactions on Signal Processing*, vol. 44, pp. 281–295, February 1996.

[6] D. R. Wehner, *High Resolution Radar*. Norwood, MA: Artech House, 1987.

[7] D. J. Rabideau and A. O. Steinhardt, "Improved adaptive clutter cancellation through data-adaptive training," *IEEE Transactions on Aerospace and Electronic Systems*, vol. 35, pp. 879–891, July 1999.

[8] G. W. Stewart, *Introduction to Matrix Computations*. New York, NY: Academic Press, Inc., 1973.

[9] T. Söderström and P. Stoica, *System Identification*. London, U.K.: Prentice-Hall International, 1989.

[10] J. Ward, "Space-time adaptive processing for airborne radar," Technical Report 1015, MIT Lincoln Laboratory, December 1994.

[11] W. Bangs, *Array processing with generalized beamformers*. Ph.D. dissertation, Yale University, New Haven, CT, 1971.

[12] P. Stoica and R. L. Moses, *Introduction to Spectral Analysis*. Englewood Cliffs, NJ: Prentice-Hall, 1997.

L HRR Range Bins

Secondary Segment

Segment of Interest

HRR Range Profile

IFFT

IFFT

Secondary Data

Primary data $\{x_j(n)\}_{j=0}^{L-1}$
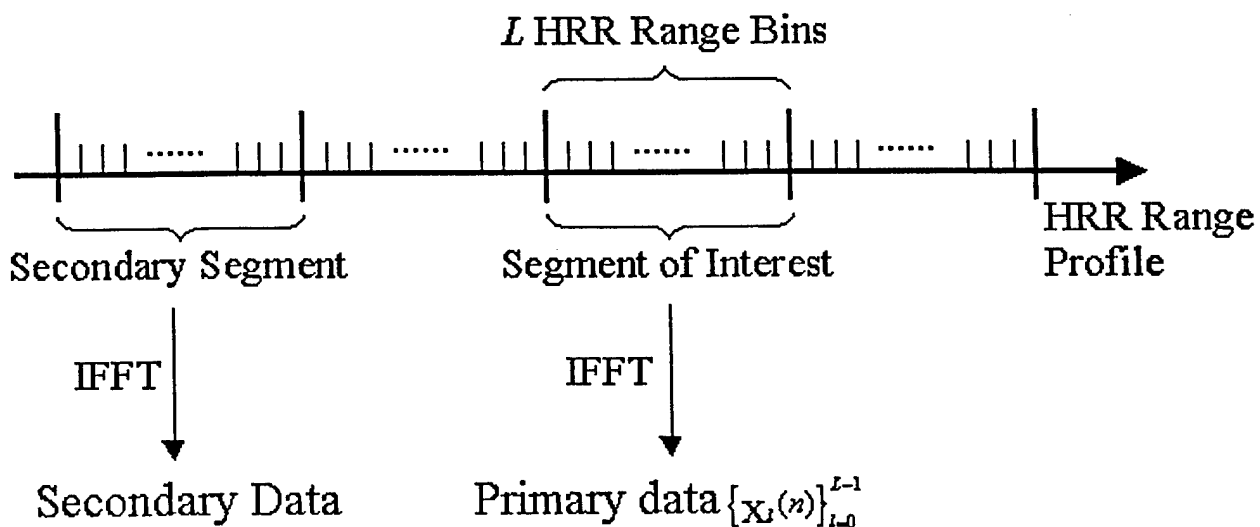
Figure 2.1: HRR range profiles are divided into LRR segments with each segment containing L HRR range bins
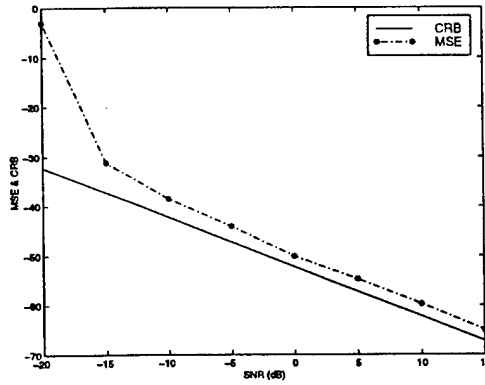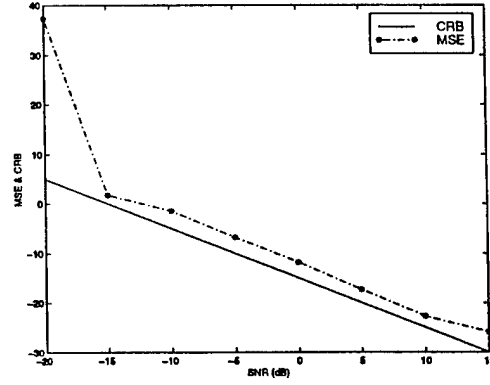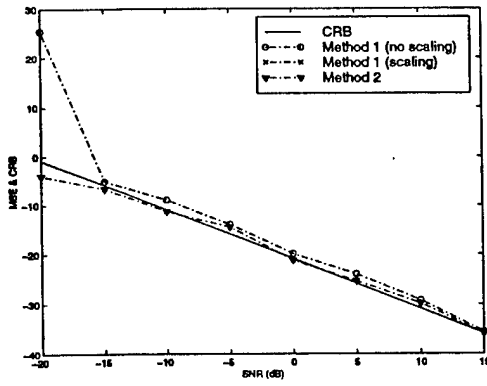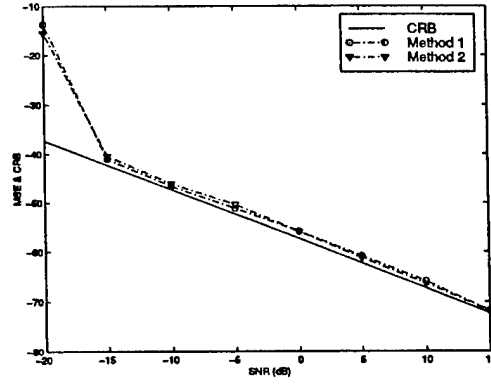
Figure 2.2: Comparison of MSEs with CRBs as a function of SNR for (a) Doppler frequency, (b) DOA, (c) amplitude, and (d) range frequency of the first scatterer of the first target with CNR= 40 dB, JNR= 25 dB, and no array calibration error.

26
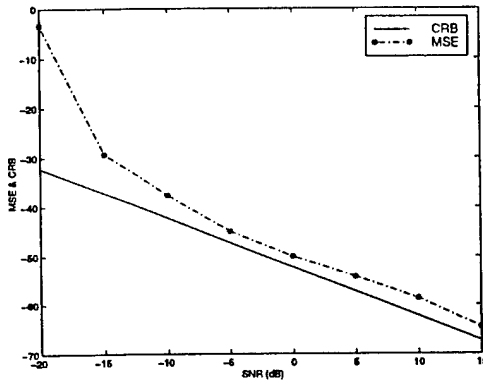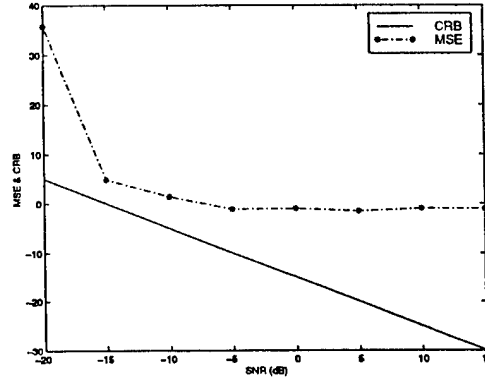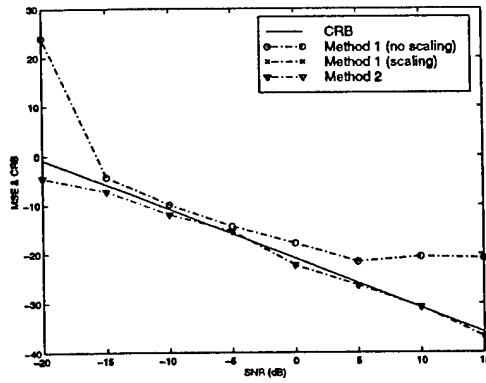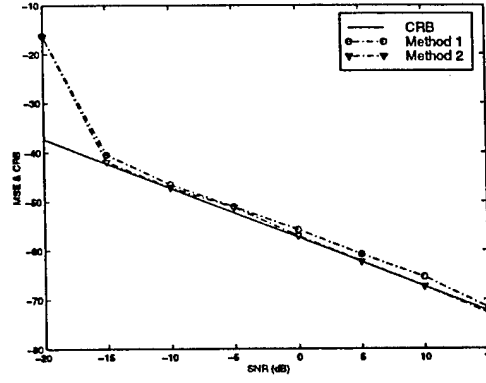
Figure 2.3: Comparison of MSEs with CRBs as a function of SNR for (a) Doppler frequency, (b) DOA, (c) amplitude, and (d) range frequency of the first scatterer of the first target with CNR= 40 dB, JNR= 25 dB, and array calibration error (covariance matrix = 0.04**I**) .

27

3. Nonparametric Spectral Analysis of Gapped Data via an Adaptive Filtering Approach

3.1 Introduction

Spectral analysis of incomplete data is needed in many applications including astronomy, underwater acoustics, radar, and communications. Conventional fast Fourier transform (FFT)-based approaches have been widely used for spectral analysis tasks due to their high computational efficiency. However, they suffer from low resolution and poor accuracy. Many other spectral analysis methods [1, 2, 3] with enhanced performance have been proposed for spectral analysis of data sequences. These methods include parametric (e.g. [4]), non-parametric (e.g. [5, 6, 7]), and semi-parametric (e.g. [8]) approaches. In general, the nonparametric approaches are less sensitive to data modeling errors than their parametric counterparts. Most, if not all of the cited methods, however, are devised for sequences of contiguous measurements without any missing data samples or gaps.

The gapped (or missing) data problem usually arises when contiguous data measurements for a long time are hard to obtain or the measurements during some intervals are not useful due to strong interference or jamming and must be discarded. For instance, in astronomy data measurements are available only in the form of groups of samples separated by rather long intervals for which no reliable measurements can be taken (see, e.g., [9, 10, 11, 12] and the references therein). In astronomical applications, special attention has been paid to detecting the presence of one or more periodic signals from incomplete data measurements by using techniques such as the periodogram [13], discrete Fourier transform (DFT) interpolation [14], the CLEAN deconvolution [11], and reconstruction of evenly sampled data by making certain assumptions on the data sequence. In radar signal processing, azimuth angle diversity data fusion (see, e.g., [15]) and data measurements in several discontinuous frequency bands also require spectral estimation for gapped or incomplete data sequences.

In this paper, we present an algorithm for nonparametric complex spectral analysis of gapped data via an adaptive FIR filtering approach, referred to as the Gapped-data Ampli-

28

tude and Phase EStimation (GAPES) algorithm. The incomplete data sequence may contain gaps of various sizes. The GAPES algorithm iterates the following two steps: (1) estimating the adaptive FIR filter and the corresponding complex spectrum via APES (Amplitude and Phase EStimation) [5, 6, 7], a nonparametric adaptive FIR filtering spectral estimation approach, and (2) filling in the gaps via an APES least squares fitting criterion. The initial condition for the iteration is obtained from the available data segments via APES.

The remainder of this paper is organized as follows. In Section 2, we formulate the problem of interest. The GAPES algorithm for complex spectral analysis of gapped data is described in detail in Section 3. In Section 4, numerical examples are presented to illustrate the performance of the proposed algorithm. Finally, Section 5 contains our conclusions.

3.2   Problem Formulation

We consider the complex spectral analysis of one-dimensional discrete-time evenly sampled data sequences with gaps of various sizes. Let $\{x(n)\}_{n=0}^{N-1}$ denote a data sequence without gaps or missing data, where N denotes the data length. The spectral analysis of $\{x(n)\}$ essentially amounts to decomposing $x(n)$, at each frequency ω of interest as:

$$x(n) = \alpha(\omega)e^{j\omega n} + e_\omega(n), \qquad n = 0, \cdots, N-1, \quad \omega \in [0, 2\pi), \qquad (3.1)$$

where $e_\omega(n)$ denotes the unmodeled noise and interference at frequency ω, and $\alpha(\omega)$ is the value of the complex spectrum of $\{x(n)\}$ at ω. Note that in some applications only the amplitude (or power) spectrum $|\alpha(\omega)|$ is of interest, whereas in others the phase of $\alpha(\omega)$ is also required.

For the complete data sequence $\{x(n)\}$, a simple method of estimating the complex spectrum $\alpha(\omega)$ is to use the computationally efficient FFT. The FFT of $\{x(n)\}$ at frequency ω normalized by a factor N gives the FFT spectral estimate $\hat{\alpha}(\omega)$ of $\alpha(\omega)$ (note that padding with zeros when performing the FFT may be necessary to obtain a smooth complex spectrum [1, 2, 3]). However, the FFT approach is known to suffer from sidelobe artifacts and poor accuracy. Many types of windows can be applied to the data sequence prior to performing

29

FFT to reduce the sidelobe effects at the cost of worsening the spectral resolution.

When some segments of the data sequence $\{x(n)\}$ are not available, we are led to the gapped data problem. Let

$$\mathbf{x} = [x(0) \quad \cdots \quad x(N-1)]^T$$
$$\triangleq [\mathbf{x}_1^T \quad \mathbf{x}_2^T \quad \cdots \quad \mathbf{x}_P^T]^T \tag{3.2}$$

be the full data vector, where $(\cdot)^T$ denotes the transpose and $\mathbf{x}_1 \cdots \mathbf{x}_P$ are nonoverlapping subvectors of $\mathbf{x}$ with lengths $N_1, \cdots, N_P$ and $\sum_{p=1}^P N_p = N$. A gapped data vector $\mathbf{x}_g$ is defined similarly to $\mathbf{x}$ above except that $\mathbf{x}_p$ for $p = 2, 4, \cdots, P-1$ (P is assumed to be an odd number) are missing.

The FFT-based spectral analysis of gapped-data sequences by filling in the gaps with zeros may well yield an estimated spectrum with many artifacts, such as false peaks (which in RADAR applications would correspond to ghost targets). This phenomenon is illustrated in Figure 3.1 in which the simulated true spectrum (Figure 3.1(a)) consists of two spectral lines located at $f_1 = \omega_1/2\pi = 0.12$ Hz and $f_2 = \omega_2/2\pi = 0.14$ Hz with amplitudes $\alpha_1 = 1$ and $\alpha_2 = 0.2$, respectively. The total number of samples is $N = 64$ with the samples 19 through 40 missing and hence set to zero in the FFT (in the previous notation this scenario corresponds to $N_1 = 18, N_2 = 22$, and $N_3 = 24$). The available data samples are corrupted by an additive white Gaussian noise sequence with zero-mean and variance 0.01. A Taylor window with shape parameter 5 and -35 dB sidelobe level will be used throughout this paper for the windowed FFTs. Although usually we are interested in the complex spectrum, in the figures we only present the moduli of the complex spectral estimates for convenience. Figure 3.1(b) shows the magnitude of the windowed FFT spectrum of the gapped data sequence $\{x_g(n)\}$ with a zero-padding length equal to $4N$. Owing to replacing the missing data with zeros, the spectrum in Figure 3.1(b) contains significant sidelobe artifacts, which are due to leakage from the dominant peak. The peak due to the second spectral line at $f_2 = 0.14$ Hz is completely buried in the sidelobe effects of the dominant peak. For comparison, Figures 3.1(c) and (d), respectively, show the moduli of the windowed FFT spectra of $\{x(n)\}$ and $\{x_3(n)\}$, the longer non-zero data segment in $\{x_g(n)\}$. Both sequences are zero-padded to 4

times their original lengths. The two spectral lines are not resolved in the windowed FFT spectrum in Figure 3.1(d) due to the short length of $\{x_3(n)\}$. Furthermore, even though the difference between the two frequencies f_1 and f_2 is larger than the FFT resolution limit of $1/N$ (i.e. $|f_1 - f_2| = 0.02 > 1/N \approx 0.016$), they cannot be clearly resolved even when the complete data sequence is assumed to be available since windowing worsens the FFT resolution (see Figure 3.1(c)).

Hence, as expected, the analysis of individual contiguous-data segments in a gapped sequence leads to poor spectral resolution. Also, data fusion via the direct FFT of the sequence with the gaps filled with zeros yields spectra with significant artifacts, such as ghost peaks, which are difficult to interpret. In what follows we show how to estimate $\alpha(\omega)$ from $\{x_g(n)\}$ via an enhanced nonparametric adaptive filtering approach referred to as GAPES (an acronym that was explained in Section 1).

3.3 Spectral Analysis of Gapped Data via GAPES

We first present the GAPES algorithm for a data sequence with one gap. We then extend it in a straightforward manner to the case of multiple gaps of various lengths.

3.3.1 Data Sequence with One Gap

When only one gap exists in the measured data sequence, we have

$$\mathbf{x}_g = \begin{bmatrix} \mathbf{x}_1^T & \mathbf{x}_2^T & \mathbf{x}_3^T \end{bmatrix}^T, \tag{3.3}$$

where the elements of $\mathbf{x}_2$ are considered to be unknown parameters in what follows. Let $\mathbf{h}(\omega)$ denote the impulse response of an M-tap FIR filter,

$$\mathbf{h}(\omega) = [h_1(\omega) \quad h_2(\omega) \quad \cdots \quad h_M(\omega)]^T, \tag{3.4}$$

and let

$$\bar{\mathbf{x}}_g(l) = [x_g(l) \quad x_g(l+1) \quad \cdots \quad x_g(l+M-1)]^T, \quad l = 0, \cdots, L-1, \tag{3.5}$$

31

denote the forward overlapping vectors constructed from the sequence $\{x_g(n)\}$, where $L = N - M + 1$ and $x_g(n)$ denotes the nth element of $\mathbf{x}_g$. Note that $\bar{\mathbf{x}}_g(l)$ is a function of $\mathbf{x}_2$. We would like to choose $\mathbf{h}(\omega)$ such that the filter output, $\mathbf{h}^H \bar{\mathbf{x}}_g(l)$, resembles as much as possible the sinusoidal component of frequency ω in the data sequence:

$$\mathbf{h}^H(\omega)\bar{\mathbf{x}}_g(l) = \alpha(\omega)e^{j\omega l} + \mathrm{res}_\omega(l), \quad l = 0, \ldots, L-1, \tag{3.6}$$

where the residual term should be as small as possible (in a least-squares sense, see below). At the same time, we want to choose $\mathbf{x}_2$ similarly so that the $\{\mathrm{res}_\omega(l)\}$ are kept small for any ω. Finally, we determine the estimated complex spectrum $\hat{\alpha}(\omega)$ from the same considerations. Mathematically, we propose to obtain the estimated spectrum as well as an estimate of the missing data by solving the following minimization problem:

$$\left\{\hat{\mathbf{x}}_2, \hat{\mathbf{h}}(\omega), \hat{\alpha}(\omega)\right\} = \min_{\mathbf{x}_2, \mathbf{h}(\omega), \alpha(\omega)} \sum_\omega \sum_{l=0}^{L-1} \left|\mathbf{h}^H(\omega)\bar{\mathbf{x}}_g(l) - \alpha(\omega)e^{j\omega l}\right|^2,$$
$$\text{subject to} \quad \mathbf{h}^H(\omega)\mathbf{a}(\omega) = 1, \tag{3.7}$$

where $\sum_\omega$ denotes the summation over a set of frequency values in $[0, 2\pi)$ (which will be specified later), and

$$\mathbf{a}(\omega) = \begin{bmatrix} 1 & e^{j\omega} & \cdots & e^{j(M-1)\omega} \end{bmatrix}^T. \tag{3.8}$$

In the above equations we have used the notation $\mathbf{h}(\omega)$ to emphasize the dependence of the filter coefficient vector on the frequency ω. Also, in these equations, $(\cdot)^H$ denotes the conjugate transpose, and the constraint $\mathbf{h}^H(\omega)\mathbf{a}(\omega) = 1$ is imposed to ensure that the FIR filter passes the frequency ω undistorted.

The minimization in (3.7) is a complicated nonlinear (fourth-order) optimization problem. Below we present a cyclic approach that alternates between two basic steps of spectrum estimation and gap filling. Specifically, one step determines the adaptive filter and the complex spectrum by using the most recent estimate $\hat{\mathbf{x}}_2$ of $\mathbf{x}_2$ in (3.7). As shown in the sequel this step entails an application of the APES algorithm to the interpolated data sequence $\hat{\mathbf{x}} = [\mathbf{x}_1^T \ \hat{\mathbf{x}}_2^T \ \mathbf{x}_3^T]^T$. The other step fills in the gap using the latest filter and spectrum estimate in (3.7) to determine $\mathbf{x}_2$. These two steps are presented in detail below.

Spectral Estimation

Assume that an estimate $\hat{\mathbf{x}}_2$ of $\mathbf{x}_2$ is available. We obtain the interpolated data $\hat{\mathbf{x}}$ by replacing $\mathbf{x}_2$ in (3.3) with $\hat{\mathbf{x}}_2$. The estimated vectors $\hat{\bar{\mathbf{x}}}(l)$, $l = 0, 1, \cdots, L-1$, are constructed from $\hat{\mathbf{x}}$ in the same way as $\bar{\mathbf{x}}_g(l)$ are formed from $\mathbf{x}_g$ (see (3.5)). The criterion in (3.7) for filter and spectrum determination can then be expressed as

$$\left\{ \hat{\mathbf{h}}(\omega), \hat{\alpha}(\omega) \right\} = \min_{\mathbf{h}(\omega), \alpha(\omega)} \sum_{l=0}^{L-1} \left| \mathbf{h}^H(\omega)\hat{\bar{\mathbf{x}}}(l) - \alpha(\omega)e^{j\omega l} \right|^2,$$
$$\text{subject to} \quad \mathbf{h}^H(\omega)\mathbf{a}(\omega) = 1. \tag{3.9}$$

Let $\bar{\mathbf{X}}(\omega)$ be the normalized Fourier transform of the vector sequence $\{\hat{\bar{\mathbf{x}}}(l)\}$

$$\bar{\mathbf{X}}(\omega) = \frac{1}{L} \sum_{l=0}^{L-1} \hat{\bar{\mathbf{x}}}(l) e^{-j\omega l}. \tag{3.10}$$

and let $\hat{\bar{\mathbf{R}}}$ denote the sample covariance matrix of $\{\hat{\bar{\mathbf{x}}}(l)\}$,

$$\hat{\bar{\mathbf{R}}} = \frac{1}{L} \sum_{l=0}^{L-1} \hat{\bar{\mathbf{x}}}(l)\hat{\bar{\mathbf{x}}}^H(l). \tag{3.11}$$

Then it can readily be verified [7] that the minimization of the quadratic criterion in (3.9) with respect to $\mathbf{h}(\omega)$ and $\alpha(\omega)$ yields the filter

$$\hat{\mathbf{h}}(\omega) = \frac{\hat{\mathbf{Q}}^{-1}(\omega)\mathbf{a}(\omega)}{\mathbf{a}^H(\omega)\hat{\mathbf{Q}}^{-1}(\omega)\mathbf{a}(\omega)}, \tag{3.12}$$

and the following estimated complex spectrum at frequency ω:

$$\hat{\alpha}(\omega) = \hat{\mathbf{h}}^H(\omega)\bar{\mathbf{X}}(\omega), \tag{3.13}$$

where

$$\hat{\mathbf{Q}}(\omega) = \hat{\bar{\mathbf{R}}} - \bar{\mathbf{X}}(\omega)\bar{\mathbf{X}}^H(\omega). \tag{3.14}$$

The $\{\hat{\alpha}(\omega)\}$ above is recognized as the APES spectrum estimate obtained from the interpolated data sequence $\hat{\mathbf{x}}$ [5, 6, 7]. It might be thought that the implementation of (3.13) requires the inversion of an $M \times M$ matrix for each ω. However, this is not necessary. Indeed,

by the matrix inversion lemma:

$$\hat{Q}^{-1}(\omega) = \hat{\bar{R}}^{-1} + \frac{\hat{\bar{R}}^{-1}\bar{X}(\omega)\bar{X}(\omega)^H\hat{\bar{R}}^{-1}}{1 - \bar{X}(\omega)^H\hat{\bar{R}}^{-1}\bar{X}(\omega)} \tag{3.15}$$

Hence we only need to compute $\hat{\bar{R}}^{-1}$, which is independent of ω. By letting

$$\beta(\omega) = \mathbf{a}(\omega)^H\hat{\bar{R}}^{-1}\mathbf{a}(\omega) \tag{3.16}$$

$$\gamma(\omega) = \mathbf{a}(\omega)^H\hat{\bar{R}}^{-1}\bar{X}(\omega) \tag{3.17}$$

$$\rho(\omega) = \bar{X}(\omega)^H\hat{\bar{R}}^{-1}\bar{X}(\omega) \tag{3.18}$$

we can simply write:

$$\hat{\alpha}(\omega) = \frac{\gamma(\omega)}{\beta(\omega)(1 - \rho(\omega)) + |\gamma(\omega)|^2} \tag{3.19}$$

and similarly for $\hat{h}(\omega)$. When applied to complete data sequences, APES achieves the best performance for a filter length of $M = N/2$ [5, 6]. In what follows, we will choose $M = N/2$ (unless specified otherwise) to calculate the APES-like spectrum estimate in (3.13) for the gapped-data case. We will evaluate (3.13) at the discrete Fourier transform (DFT) frequencies $\omega_k = 2\pi k/K$, $k = 0, 1, \cdots K - 1$ (with $K \geq N$).

Gap Filling

Once $\{\hat{h}(\omega_k), \hat{\alpha}(\omega_k)\}_{k=0}^{K-1}$ were made available, we can determine $\mathbf{x}_2$ by solving the following quadratic minimization problem (cf. (3.7)):

$$\hat{\mathbf{x}}_2 = \min_{\mathbf{x}_2} \sum_{k=0}^{K-1} \sum_{l=0}^{L-1} \left|\hat{h}^H(\omega_k)\bar{x}_g(l) - \hat{\alpha}(\omega_k)e^{j\omega_k l}\right|^2. \tag{3.20}$$

Let

$$H_k = \begin{bmatrix} \hat{h}^H(\omega_k) & & & \\ & \hat{h}^H(\omega_k) & & \\ & & \ddots & \\ & & & \hat{h}^H(\omega_k) \end{bmatrix}, \tag{3.21}$$

34

and

$$z_k = \hat{\alpha}(\omega_k) \begin{bmatrix} 1 \\ e^{j\omega_k} \\ \vdots \\ e^{j(L-1)\omega_k} \end{bmatrix}. \qquad (3.22)$$

Using this notation we can write the criterion in (3.20) as:

$$\sum_{k=0}^{K-1} \left\| H_k \begin{array}{c} x_1 \\ x_2 \\ x_3 \end{array} - z_k \right\|^2. \qquad (3.23)$$

Partition H_k as:

$$H_k = [\underbrace{A_k}_{N_1} \ \underbrace{B_k}_{N_2} \ \underbrace{C_k}_{N_3}] \qquad (3.24)$$

and define

$$y_k = -A_k x_1 - C_k x_3 + z_k. \qquad (3.25)$$

With this notation the criterion becomes,

$$\sum_{k=0}^{K-1} \|B_k x_2 - y_k\|^2 \qquad (3.26)$$

whose minimizer with respect to x_2 is well-known to be

$$\hat{x}_2 = \left[\sum_{k=0}^{K-1} B_k^H B_k \right]^{-1} \sum_{k=0}^{K-1} B_k^H y_k. \qquad (3.27)$$

The interpolated data sequence $\hat{x}$ is obtained by replacing x_2 in (3.3) with $\hat{x}_2$.

Initialization

To start the algorithm we need an initial estimate of either x_2 or the adaptive filter along with the complex spectrum. In our initialization approach we first obtain an initial adaptive FIR filter $h^{(0)}(\omega)$ and an initial spectral estimate $\alpha^{(0)}(\omega)$ by using the available data x_1 and x_3.

35

Note that both the forward and backward data vectors are often used to achieve better spectral estimation performance [5, 6]. When both the forward and backward vectors are used for spectral estimation, $\hat{h}(\omega)$ in (3.12) and $\hat{\alpha}(\omega)$ in (3.13) remain the same except that $\hat{Q}(\omega)$ in (3.14) is replaced by [7]

$$\hat{Q}(\omega) = \hat{R} - X(\omega)X^H(\omega), \tag{3.28}$$

where

$$\hat{R} = \frac{1}{2}\left(\hat{\bar{R}} + \hat{\tilde{R}}\right), \tag{3.29}$$

$$X(\omega) = \frac{1}{\sqrt{2}}\left[\bar{X}(\omega) \quad \tilde{X}(\omega)\right], \tag{3.30}$$

$$\tilde{X}(\omega) = \frac{1}{L}\sum_{l=0}^{L-1}\hat{\tilde{x}}(l)e^{-j\omega l}, \tag{3.31}$$

$$\hat{\tilde{R}} = \frac{1}{L}\sum_{l=0}^{L-1}\hat{\tilde{x}}(l)\hat{\tilde{x}}^H(l), \tag{3.32}$$

and where $\hat{\tilde{x}}(l), l = 0, 1, \cdots, L-1$ are the backward overlapping vectors

$$\hat{\tilde{x}}(l) = [\hat{x}^*(N-l-1) \quad \hat{x}^*(N-l-2) \quad \cdots \quad \hat{x}^*(N-l-M)]^T. \tag{3.33}$$

The filter length we use in the initialization step is the smallest integer larger than or equal to $0.75\min(N_1, N_3)$. The $\hat{h}^{(0)}(\omega)$ is calculated as in (3.12) in which $\hat{Q}^{(0)}(\omega)$ is obtained by using (3.28) with the following modifications:

$$\hat{R}^{(0)} = \frac{1}{4}\left(\hat{\bar{R}}_1^{(0)} + \hat{\tilde{R}}_1^{(0)} + \hat{\bar{R}}_3^{(0)} + \hat{\tilde{R}}_3^{(0)}\right), \tag{3.34}$$

and

$$X^{(0)}(\omega) = \frac{1}{2}\left[\bar{X}_1^{(0)}(\omega) \quad \tilde{X}_1^{(0)}(\omega) \quad \bar{X}_3^{(0)}(\omega) \quad \tilde{X}_3^{(0)}(\omega)\right], \tag{3.35}$$

where $\hat{\bar{R}}_i^{(0)}$ and $\hat{\tilde{R}}_i^{(0)}$, $i = 1, 3$, are the estimated forward and backward sample covariance matrices obtained from x_i, $i = 1, 3$; and similarly $\bar{X}_i^{(0)}(\omega)$ and $\tilde{X}_i^{(0)}(\omega)$, $i = 1, 3$, are the normalized Fourier transforms of the forward and backward overlapping vectors. To compute those quantities we use their previously given definitions with L replaced by $L_i = N_i - M + 1$.

The initial APES spectrum is given by

$$\hat{\alpha}^{(0)}(\omega_k) = \frac{1}{2}\hat{\mathbf{h}}^{(0)}(\omega_k)\left[\bar{X}_1(\omega_k) + \bar{X}_3(\omega_k)e^{-j2\omega_k(N_1+N_2)}\right],\tag{3.36}$$

for $k = 0, 1, \cdots, K - 1$.

Summary of the Steps for One Gap

Step 0. Initialization: start the algorithm using the initialization approach presented above.

Step 1. Gap filling: update the gap estimate by using (3.27) based on the most recently determined adaptive filter and complex spectrum $\{\hat{\mathbf{h}}(\omega_k), \hat{\alpha}(\omega_k)\}$.

Step 2. Spectral estimation: determine the adaptive filter and the complex spectrum with (3.12) and (3.13), respectively, from the most recently interpolated data sequence $\{\hat{x}(n)\}$.

Step 3. Iteration: repeat Steps 1 and 2 until the relative change of the cost function

$$\sum_{k=0}^{K-1}\sum_{l=0}^{L-1}\left|\hat{\mathbf{h}}^H(\omega_k)\hat{\bar{\mathbf{x}}}(l) - \hat{\alpha}(\omega_k)e^{j\omega_k l}\right|^2\tag{3.37}$$

between two consecutive iterations is equal to or less than a preset threshold value ϵ or the number of iterations reaches a preset number $I_{\max}$.

3.3.2 Data Sequence with Multiple Gaps

The extension of the algorithm presented in the previous section to the multi-gap case is straightforward. The criterion (3.7) that lies at the basis of GAPES remains unchanged and so does the spectrum estimation step of GAPES. The gap filling step requires a slight modification of the partition in (3.24) to take into account the multi-gap structure of the data, and so does the initialization step.

In fact it should be clear from the previous discussion that GAPES is applicable to cases in which the *missing data has any pattern*. The only step that may need a more significant modification in such cases is the initialization step. In the case of arbitrary missing-data patterns we can hardly use any special initialization. Hence we may have to use the simplest initialization of all possible initializations: set missing data to zero. If the ratio of the number

of available data samples to that of missing data is reasonably high the aforementioned simple initialization may be quite satisfactory.

Finally, we remark on the fact that the GAPES algorithm can be readily extended to criteria of the more general form

$$\sum_{k=0}^{K-1} w_k \sum_{l=0}^{L-1} v_l \left| \mathbf{h}^H(\omega_k)\bar{\mathbf{x}}_g(l) - \alpha(\omega_k)e^{j\omega_k l} \right|^2 \tag{3.38}$$

where the weights $\{w_k \geq 0; \ v_k \geq 0\}$ can be used to emphasize a frequency band in which we have a particular interest or a subsample of the data sequence that is thought of being more reliable.

3.4 Numerical Results

We present several numerical examples to illustrate the performance of GAPES for the complex spectral analysis of gapped data. We choose $K = N$ and $M = N/2$ in the iteration steps of GAPES. Although the frequency grid for $\hat{\alpha}(\omega)$ can be chosen in many ways, we use the DFT grid $\omega_k = 2\pi k/K$, $k = 0, 1, \cdots, K-1$. The noise added to the available data samples is white Gaussian with zero-mean and variance 0.01. In the initialization step of GAPES, the filter length is chosen to be the smallest integer larger than or equal to 3/4 of the length of the shortest available data segment. We use $\epsilon = 10^{-2}$ to test the convergence of the GAPES algorithm and set the maximum number of iterations to $I_{\max} = 10$. Once the iterative process is terminated, we obtain our final spectral estimate by evaluating the estimated spectrum of the last iteration on a grid that is four times finer than the K-point DFT grid.

We compare our GAPES algorithm with the windowed FFT approach as well as the parametric CLEAN algorithm (see, e.g., [10, 11]) that has been proved to be quite useful in many applications including astronomical data analysis, microwave imaging, and target feature extraction. When using CLEAN, we model the data as a sum of complex sinusoids. CLEAN first estimates the parameters of the strongest sinusoid via FFT with zero-padding, subtracts it from the original data, and then repeats this process for the next strongest

sinusoid until the predetermined number of sinusoids is reached or the estimated amplitude of the latest sinusoid is small enough compared to the strongest one. Once the sinusoidal parameters are estimated, they are used to simulate the data in the gaps. The windowed FFT with zero-padding is then applied to the so-obtained interpolated data sequence to form the CLEAN spectrum.

For the same example as the one in Figure 3.1, Figure 3.2(a) shows the modulus of the APES spectrum obtained from the complete data sequence $\{x(n)\}$. A comparison between Figures 3.2(a) and 3.1(c) shows that APES outperforms the windowed FFT approach. Figures 3.2(b) and (c) show the moduli of the windowed FFT spectra obtained from the data interpolated by CLEAN and GAPES, respectively. Note that in Figure 3.2(b) the weaker spectral line at $f_2 = 0.14$ Hz is not visible. Figure 3.2(c) is comparable to Figure 3.1(c) which indicates that the interpolated data obtained by GAPES are close to the true values of the unavailable data. Figures 3.2(d) shows the modulus of the APES spectrum of the data interpolated by GAPES, which is almost as good as that in Figure 3.2(a) obtained from the complete data sequence.

Next consider a gapped data sequence with the same length and the same gap size and location as in the previous example but with a more complicated spectrum. Specifically, a mixed spectrum (shown in Figure 3.3(a)) is considered in this example, which comprises two discrete spectral lines located at $f_1 = 0.05$ Hz and $f_2 = 0.07$ Hz with amplitudes $\alpha_1 = 1$ and $\alpha_2 = 0.5$, respectively, and a continuous spectral component centered at $f_s = 0.18$ Hz with a width of $b = 0.04$ Hz and a constant magnitude of $\alpha = 0.25$. Figures 3.3(b) and (c) show the moduli of the windowed FFT spectra of the gapped and complete data sequences. The moduli of the windowed FFT spectra obtained from the CLEAN and GAPES interpolated data sequences are presented in Figures 3.3(d) and (e). Figure 3.3(f) shows the magnitude of the APES spectrum of the GAPES interpolated data sequence. Comparisons between the various parts of Figure 3.3 lead to similar conclusions to those drawn from the results shown in Figures 3.1 and 3.2.

Finally, we present an example that concerns the spectral analysis of an incomplete data sequence with two gaps. The total length of the simulated sequence is $N = 128$, and the

samples 23 through 46 and 76 through 100 are missing. Hence nearly 40% of the data samples are missing. Figure 3.4(a) shows the true spectrum which consists of four discrete spectral lines at $f_1 = 0.05$ Hz, $f_2 = 0.065$ Hz, $f_3 = 0.26$ Hz, and $f_4 = 0.28$ Hz with amplitudes $\alpha_1 = \alpha_2 = \alpha_3 = 1$ and $\alpha_4 = 0.5$, and a continuous spectral component at $f_s = 0.18$ Hz with a width $b = 0.015$ Hz and a constant magnitude of $\alpha = 0.25$. Figures 3.4(b) and (c) show the moduli of the windowed FFT spectra of the gapped and complete data sequences. Figures 3.4(d) and (e) display the moduli of the windowed FFT spectra of the interpolated data sequences obtained via CLEAN and GAPES, respectively. Figure 3.4(f) shows the modulus of the APES spectrum of the interpolated data sequence obtained via GAPES. Note that in this case CLEAN cannot remove all false peaks owing to the serious leakage problem of FFT, which makes CLEAN pick peaks at wrong locations. Once again, GAPES appears to provide the most accurate interpolated data sequence and spectral estimate.

3.5 Conclusions

We have presented an algorithm for nonparametric complex spectral analysis of incomplete data with gaps of various lengths via an adaptive FIR filtering approach, referred to as the Gapped-data Amplitude and Phase EStimation (GAPES) algorithm. The GAPES algorithm iterates the following two steps: (1) estimating the adaptive filter and the corresponding complex spectrum via APES, and (2) filling in the gaps by using the APES least-squares fitting criterion. We initialized the GAPES algorithm by applying APES to the available data segments. Numerical examples have been used to demonstrate the effectiveness of the proposed GAPES algorithm and compare it with the windowed FFT approach and the parametric CLEAN algorithm. The results have shown that GAPES yields more accurate interpolated sequences and spectral estimates than the other approaches considered in this chapter.

Reference

[1] J. S. L. Marple, *Digital Spectral Analysis with Applications.* Englewood Cliffs, N.J.: Prentice-Hall, 1987.

[2] S. M. Kay, *Modern Spectral Estimation: Theory and Application.* Englewood Cliffs, N.J.: Prentice-Hall, 1988.

[3] P. Stoica and R. L. Moses, *Introduction to Spectral Analysis.* Upper Saddle River, N.J.: Prentice-Hall, 1997.

[4] J. Li and P. Stoica, "Efficient mixed-spectrum estimation with applications to target feature extraction," *IEEE Transactions on Signal Processing,* vol. 44, pp. 281–295, February 1996.

[5] J. Li and P. Stoica, "An adaptive filtering approach to spectral estimation and SAR imaging," *IEEE Transactions on Signal Processing,* vol. 44, pp. 1469–1484, June 1996.

[6] H. Li, J. Li, and P. Stoica, "Performance analysis of forward-backward matched-filterbank spectral estimators," *IEEE Transactions on Signal Processing,* vol. 46, pp. 1954–1966, July 1998.

[7] P. Stoica, H. Li, and J. Li, "A new derivation of the APES filter," *IEEE Signal Processing Letters,* vol. 6, pp. 205–206, August 1999.

[8] R. Wu, J. Li, Z. Bi, and P. Stoica, "SAR image formation via semiparametric spectral estimation," *IEEE Transactions on Aerospace and Electronics Systems,* vol. 35, October 1999.

[9] D. D. Meisel, "Fourier transforms of data sampled in unequally spaced segments," *The Astronomical Journal,* vol. 84, pp. 116–126, January 1979.

[10] J. D. Scargle, "Studies in astronomical time series analysis I: Modeling random-processes in the time domain," *The Astrophysical Journal Supplement Series,* vol. 45, pp. 1–71, 1981.

[11] D. H. Roberts, J. Lehár, and J. W. Dreher, "Time series analysis with CLEAN I: Derivation of a spectrum," *The Astronomical Journal,* vol. 93, pp. 968–989, April 1987.

[12] G. B. Rybicki and W. H. Press, "Interpolation, realization, and reconstruction of noisy, irregularly sampled data," *The Astrophysical Journal*, vol. 398, pp. 169–176, October 1992.

[13] J. D. Scargle, "Studies in astronomical time series analysis II: Statistical aspects of spectral analysis of unevenly spaced data," *The Astrophysical Journal*, vol. 263, pp. 835–853, December 1982.

[14] J. D. Scargle, "Studies in astronomical time series analysis III: Fourier transforms, autocorrelation functions, and cross-correlation functions of unevenly spaced data," *The Astrophysical Journal*, vol. 343, pp. 874–887, August 1989.

[15] J. Man, G. Liu, and J. Li, "A quasi-parametric algorithm for SAR target feature extraction and imaging with angle diversity," to appear in *Circuits, Systems, Signal Processing*.
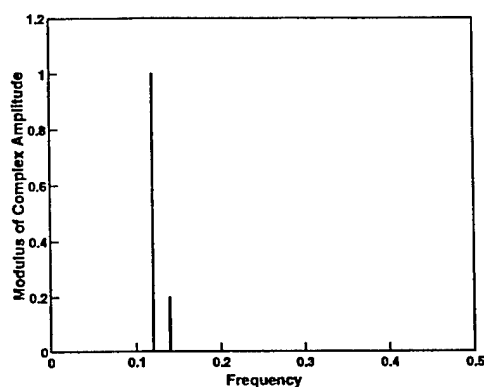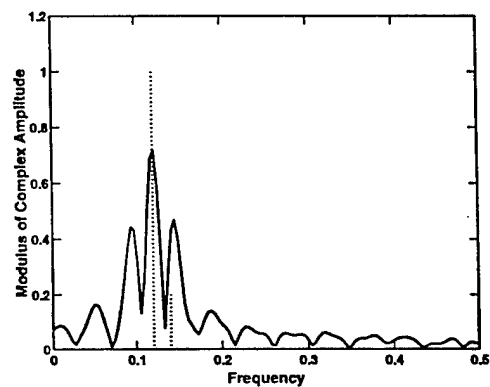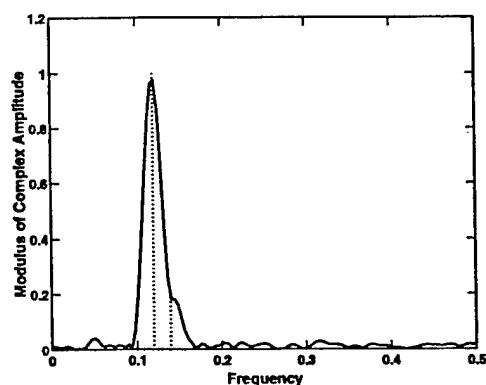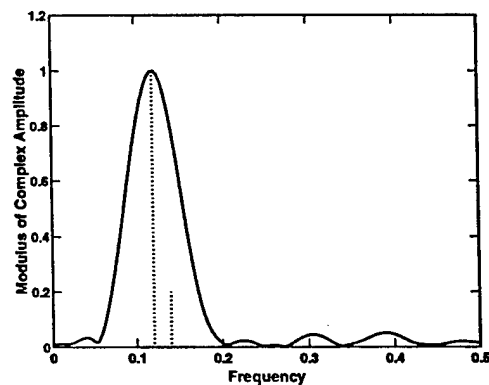
Figure 3.1: Moduli of the complex spectral estimates (solid lines in (b)-(d)) compared with the true spectrum (dotted lines in (b)-(d)); (a) true spectrum, (b) windowed FFT spectrum of the gapped data sequence, (c) windowed FFT spectrum of the complete data sequence, (d) windowed FFT spectrum of the longer contiguous-data segment.
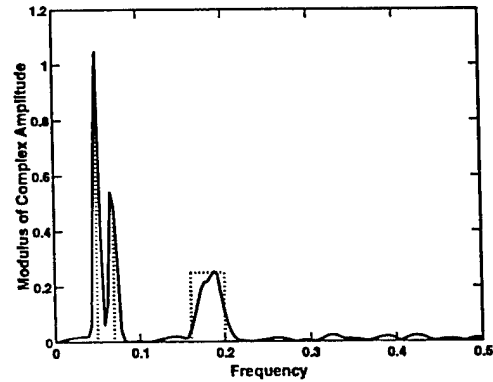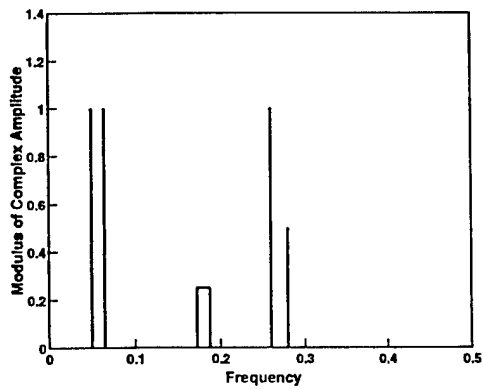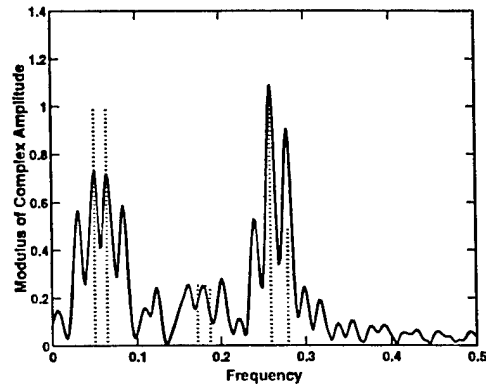
43
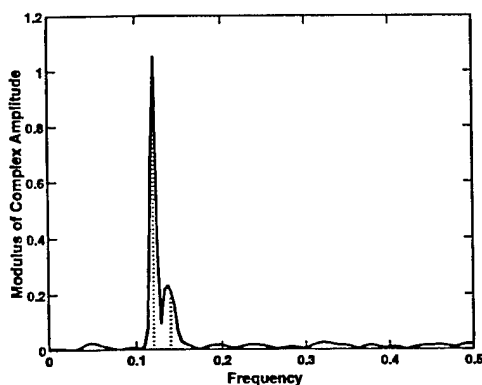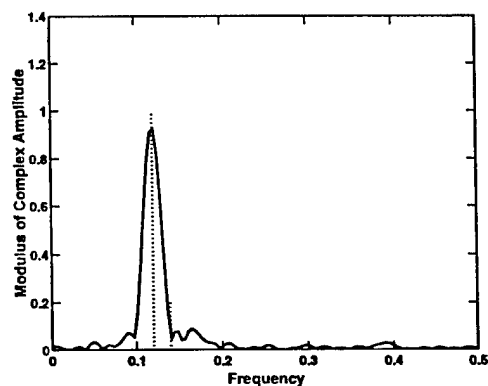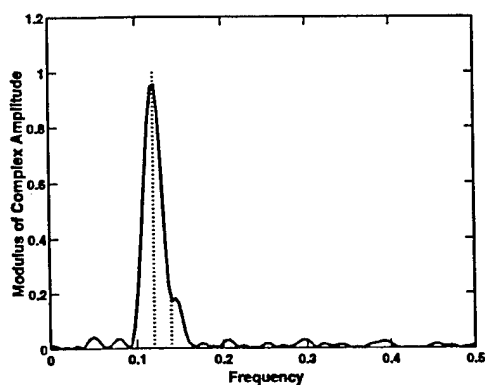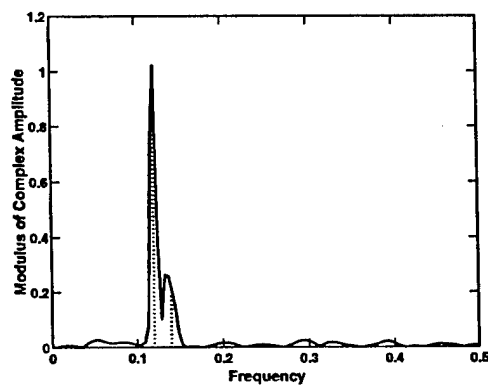
Figure 3.2: Moduli of the complex spectral estimates for the same example as in Figure 3.1. (a) APES spectrum of the complete data sequence, (b) windowed FFT spectrum of the interpolated data sequence obtained via CLEAN, (c) windowed FFT spectrum of the interpolated data sequence obtained via GAPES, (d) APES spectrum of the interpolated data sequence obtained by GAPES.
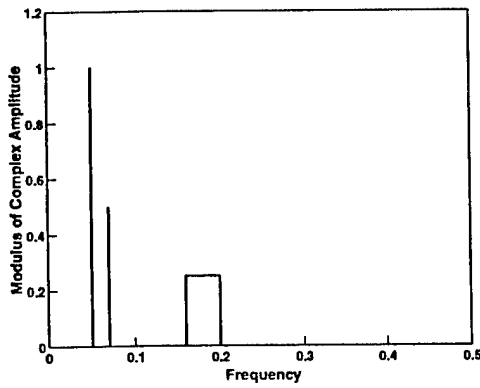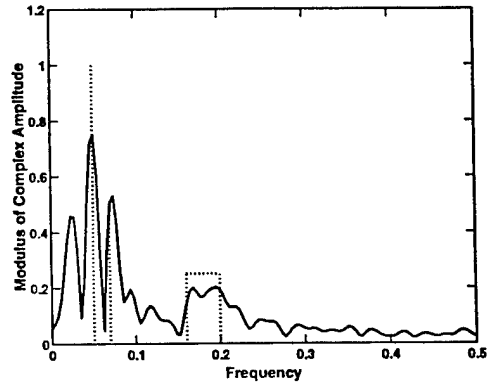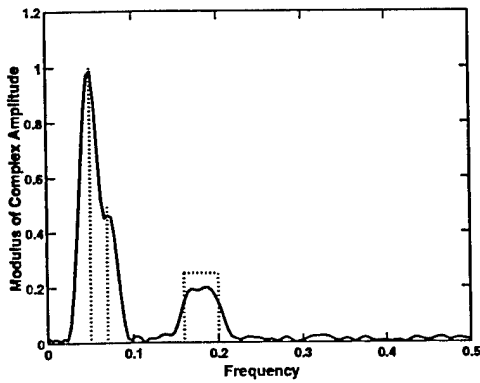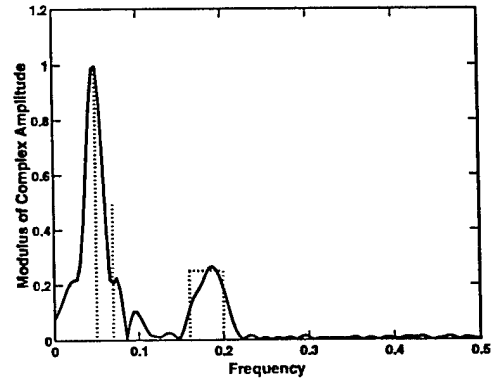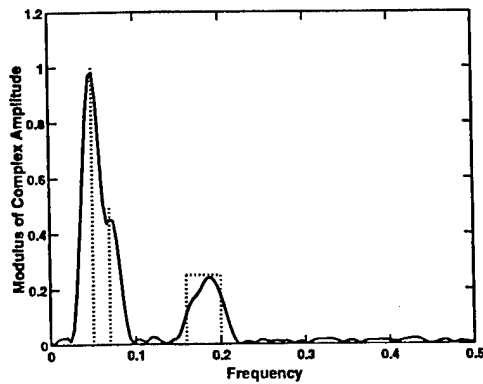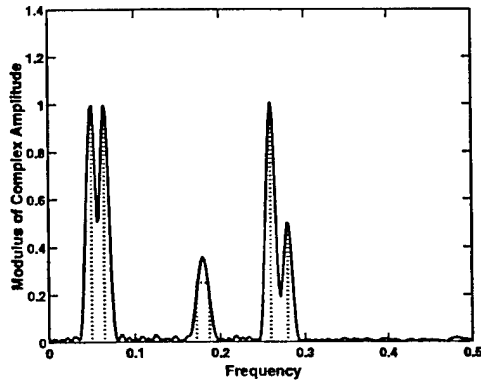
Figure 3.3: Moduli of the complex spectral estimates (solid lines in (b)-(f)) compared with the true spectrum (dotted lines in (b)-(f)); (a) true spectrum, (b) windowed FFT spectrum of the gapped data, (c) windowed FFT spectrum of the complete data, (d) windowed FFT spectrum of the interpolated data sequence obtained via CLEAN, (e) windowed FFT spectrum of the interpolated data sequence obtained via GAPES, and (f) APES spectrum of the interpolated data sequence obtained via GAPES.　　45
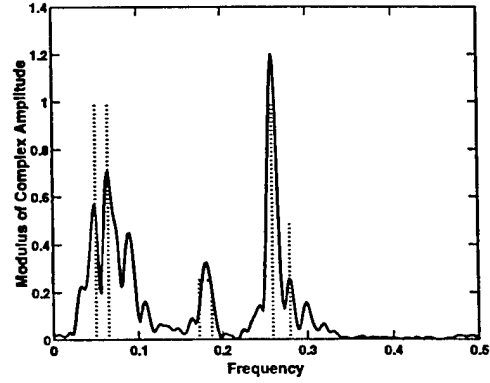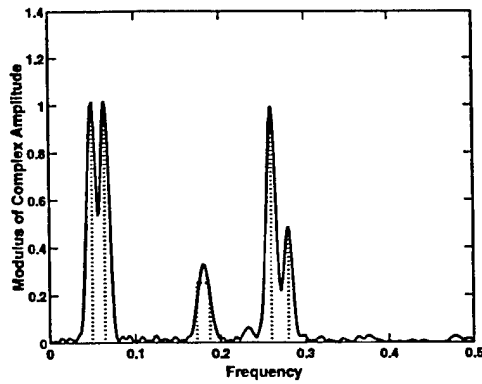
Figure 3.4: Moduli of the complex spectral estimates (solid lines in (b)-(f)) compared with the true spectrum (dotted lines in (b)-(f)); (a) true spectrum, (b) windowed FFT spectrum of the gapped data, (c) windowed FFT spectrum of the complete data, (d) windowed FFT spectrum of the interpolated data sequence obtained via CLEAN, (e) windowed FFT spectrum of the interpolated data sequence obtained via GAPES, and (f) APES spectrum of the interpolated data sequence obtained via GAPES.
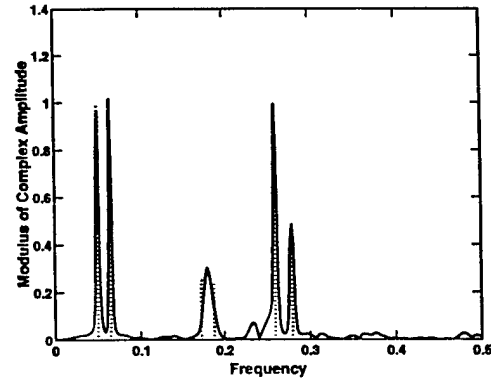
46

4. Spectral Estimation of Gapped Data and SAR Imaging with Angle Diversity

4.1 Introduction

Estimating the spectrum of a time series is crucial in applications such as radar, communications, underwater acoustics, and astronomical data analysis. Conventional fast Fourier transform (FFT) based approaches have been widely used due to their high computational efficiency. However, the major drawback of the FFT-based approaches is the inherent low resolution. A large number of methods have been proposed to obtain enhanced spectral estimates with higher resolution. Of these, the parametric (e.g. [1, 2, 3, 4]), non-parametric (e.g. [5, 6, 7, 8]), and semi-parametric [9] approaches have been considered for target feature extraction and radar imaging. In general, nonparametric approaches are less sensitive to data modeling errors and more robust than their parametric counterparts. Many nonparametric spectral estimators make use of adaptive (data-dependent) finite impulse response (FIR) filterbanks. The APES (Amplitude and Phase EStimation) spectral estimator [7, 10] belongs to this class of approaches.

The gapped-data (or missing-data) problem arises when continuous measurements are not possible, or the measurements during certain periods are not valid due to for instance interference or jamming impinging on the receiver and hence they must be discarded. In radar signal processing (see, e.g., [11, 12]), the problem of combining several sets of measurements made at different azimuth angle locations can be posed as a problem of spectral estimation from gapped data. Similar problems arise in data fusion via ultrawide-band coherent processing [13]. Furthermore, in astronomy, data are often available as groups of samples with rather long intervals during which no measurements can be taken (see, e.g., [14, 15, 16, 17, 18, 19] and the references therein). In astronomy, special attention has been paid to detecting the presence of one or more periodic signals from incomplete measurements using techniques such as the periodogram approach [15] and the CLEAN deconvolution [16].

In this paper, we consider using the APES filter for the spectral estimation of gapped data and synthetic aperture radar (SAR) imaging with angle diversity. Unlike the FFT and the windowed and/or averaged FFT spectra, the APES spectrum has good resolution properties, suffers from little or no leakage effects, and has good statistical stability [7, 20]. The excellent performance of APES in the class of nonparametric spectral analysis methods was one of the reasons why we chose to extend this particular approach to the gapped-data case. We present in the paper a relaxation based algorithm, referred to as the GAPES (Gapped-data APES) algorithm, which consists of two steps: (1) estimating the adaptive filter and the corresponding spectrum via APES, and (2) filling in the gaps via a least squares (LS) fit. For the SAR imaging with angle diversity data fusion, we perform the one-dimensional (1-D) windowed FFTs (WFFTs) in range, use the GAPES algorithm to interpolate the gaps in the aperture for each range, apply the 1-D inverse FFTs (IFFTs) and de-window in range, and apply the two-dimensional (2-D) APES algorithm to the interpolated matrix to obtain the final 2-D SAR image.

The remainder of this paper is organized as follows. In Section 2, we formulate the problem of interest. The APES algorithm for the spectral analysis of the complete data is introduced in Section 3. The GAPES algorithm for the spectral analysis of the 1-D gapped data is presented in Section 4. Section 5 presents a method to use GAPES for 2-D SAR imaging with angle diversity data fusion. In Section 6, numerical examples are presented to illustrate the performance of the proposed algorithm. Finally, Section 7 contains our conclusions.

4.2 Problem Formulation

We consider herein the spectral estimation algorithm for 1-D data sequences with multiple gaps of various sizes, and for 2-D data matrices with gaps consisting of missing columns.

Let $\{x(n)\}_{n=0}^{N-1}$ denote a complete 1-D discrete-time sequence of length N. The spectral analysis of $\{x(n)\}$ essentially amounts to decomposing $x(n)$, at each frequency $\omega \in [0, 2\pi)$

of interest as

$$x(n) = \alpha(\omega)e^{j\omega n} + e_\omega(n), \quad n = 0, \cdots, N-1, \qquad (4.1)$$

where $\alpha(\omega)$ denotes the complex amplitude of a sinusoid with frequency ω, and $e_\omega(n)$ denotes unmodeled noise and interference at ω (in other words, $e_\omega(n)$ is everything left in $x(n)$ after the sinusoidal component $\alpha(\omega)e^{j\omega n}$ has been subtracted). Note that the decomposition in (4.1) is frequency dependent and it should not be confused with assuming that $x(n)$ consists of one sinusoid in noise. In fact Equation (4.1) does not imply any modeling assumptions at all, which means that the methods based on (4.1) are *nonparametric*.

Let $\{x(n, \bar{n})\}$, $n = 0, 1, \cdots, N-1$, $\bar{n} = 0, 1, \cdots, \bar{N}-1$, denote a 2-D discrete-time data matrix. For a frequency pair $\{\omega, \bar{\omega}\}$ of interest, $\{x(n, \bar{n})\}$ is modeled as

$$x(n, \bar{n}) = \alpha(\omega, \bar{\omega})e^{j(\omega n + \bar{\omega}\bar{n})} + e_{\omega,\bar{\omega}}(n, \bar{n}),$$
$$n = 0, \cdots, N-1, \quad \bar{n} = 0, \cdots, \bar{N}-1; \quad \omega, \bar{\omega} \in [0, 2\pi), \qquad (4.2)$$

where $\alpha(\omega, \bar{\omega})$ denotes the complex amplitude of a sinusoid, and $e_{\omega,\bar{\omega}}(n, \bar{n})$ denotes unmodeled noise and interference at frequency $(\omega, \bar{\omega})$.

Assume that some segments of the data sequence $\{x(n)\}_{n=0}^{N-1}$ are unavailable for reasons explained above. Let

$$\mathbf{x} \triangleq [x(0) \quad \cdots \quad x(N-1)]^T$$
$$\triangleq [\mathbf{x}_1^T \quad \mathbf{x}_2^T \quad \cdots \quad \mathbf{x}_P^T]^T \qquad (4.3)$$

be the *complete* data vector, where $\mathbf{x}_1, \cdots \mathbf{x}_P$ are subvectors of $\mathbf{x}$, whose lengths are $N_1, \cdots, N_P$, respectively, with $\sum_{p=1}^P N_p = N$. Here $(\cdot)^T$ denotes the transpose. A *gapped-data* vector $\mathbf{x}_g$ is formed when $\mathbf{x}_p$ for $p = 2, 4, \cdots, P-1$ (P is always an odd number) are unavailable and considered as being unknown. Let $\mathbf{x}_a$ and $\mathbf{x}_u$ denote the two vectors of dimension $N_1 + N_3 + \cdots + N_P$ and $N_2 + \cdots + N_{P-1}$, whose elements are the *available* and *unavailable* data samples in $\mathbf{x}$, respectively. Hence $\mathbf{x}_a$ is given whereas $\mathbf{x}_u$ is *unknown*.

For the angle diversity data fusion problem encountered in SAR imaging, the data measured by the radar are recorded intermittently. Assuming that the radar measurements in

range are complete, the *gapped* data due to the angle diversity can be expressed as:

$$x_g(n, \bar{n}) = \begin{cases} \text{unknown}, & n = 0, 1, \cdots, N-1; \quad \bar{n} \in \mathcal{G}, \\ x(n, \bar{n}), & \text{otherwise}, \end{cases} \tag{4.4}$$

where $\mathcal{G}$ denotes the set of azimuth look indices $\bar{n}$ at which no measurements are taken.

Figure 4.1 shows a schematic map of a spotlight SAR with angle diversity. For two adjacent continuous segments and the gap between them, we will use the two continuous segments to interpolate the gap between them. The motivation for this is that in many cases the measurements can be non-stationary.

The FFT processing for the gapped data can yield a spectrum with significant artifacts, as demonstrated and explained in, e.g., [21]. The approach taken in this paper is to fill in the gaps corresponding to the missing data and use the so-obtained interpolated data for spectral estimation via APES.

4.3   APES for Complete Data

We review the basic facts about APES for complete data [7, 10] that are essential to understanding the GAPES algorithm for gapped data presented in the next section. For clarity of presentation, we discuss only the so-called *forward-only* version of APES (for both 1-D and 2-D cases). It can be shown [7] that a slightly modified approach, leading to the *forward-backward* APES, gives significantly better estimation accuracy. For this reason, the forward-backward APES will be used in the numerical examples in Section 6.

Estimation of $\alpha(\omega)$ in (4.1) by the method of least squares (LS) leads to the Fourier transform (FT) method:

$$\hat{\alpha}_{\text{FT}} = \frac{1}{N} \sum_{n=0}^{N-1} x(n) e^{-j\omega n}, \tag{4.5}$$

or its counterpart for power spectra, the periodogram. As is well-known, the FT approach suffers from leakage, poor resolution and erratic statistical behavior and it is rarely used without some corrections [22, 23, 24]. Smoothing is one of the most common corrections applied to the FT. One form of smoothing (or averaging) of the FT that will help us make

the connection with APES is as follows. Partition the data sequence in (4.1) into $M \times 1$ overlapping vectors with the following shifted structure:

$$\bar{\mathbf{x}}(l) = [x(l) \quad \ldots \quad x(l + M - 1)], \quad l = 0, \ldots, L - 1, \tag{4.6}$$

where $L = N - M + 1$ and M is a user parameter referred to as the filter length. Then calculate the FT of each of the data snapshots in (4.6) and *average* the so-obtained local FTs:

$$
\begin{aligned}
\hat{\alpha}_{\text{AFT}} &= \frac{1}{L} \sum_{l=0}^{L-1} \frac{1}{M} \sum_{m=0}^{M-1} x(l + m) e^{-j\omega(l+m)} \\
&= \frac{1}{L} \sum_{l=0}^{L-1} e^{-j\omega l} \left[\frac{1}{M} \sum_{m=0}^{M-1} x(l + m) e^{-j\omega m} \right].
\end{aligned}
\tag{4.7}
$$

To interpret (4.7) in a filterbank framework, define

$$\mathbf{a}(\omega) = \begin{bmatrix} 1 & e^{j\omega} & \ldots & e^{j\omega(M-1)} \end{bmatrix}^T. \tag{4.8}$$

Observe from (4.1) and (4.6) that we have

$$\bar{\mathbf{x}}(l) = \alpha(\omega) \mathbf{a}(\omega) e^{j\omega l} + \bar{\mathbf{e}}_\omega(l), \quad l = 0, \ldots, L - 1, \tag{4.9}$$

where $\bar{\mathbf{e}}_\omega(l)$ is formed from $\{e_\omega(n)\}$ in the same way as $\bar{\mathbf{x}}(l)$ is formed from $\{x(n)\}$ in (4.6).

Let

$$\mathbf{h}(\omega) = \frac{1}{M} \mathbf{a}(\omega). \tag{4.10}$$

The inner sum in (4.7) is equal to $\mathbf{h}^H(\omega) \bar{\mathbf{x}}(l)$, where $(\cdot)^H$ denotes the conjugate transpose, and hence:

$$\hat{\alpha}_{\text{AFT}}(\omega) = \frac{1}{L} \sum_{l=0}^{L-1} \left[\mathbf{h}^H(\omega) \bar{\mathbf{x}}(l) \right] e^{-j\omega l}, \tag{4.11}$$

where (cf. (4.9))

$$\mathbf{h}^H(\omega) \bar{\mathbf{x}}(l) = \alpha(\omega) e^{j\omega l} + \text{res.}, \quad l = 0, \ldots, L - 1. \tag{4.12}$$

The *averaged FT* (AFT) spectral estimator in (4.7) can thus be interpreted as consisting of two steps: (1) use the (frequency-dependent) finite-impulse-response (FIR) filter $\mathbf{h}(\omega)$

51

to prefilter the data sequence (cf. (4.12)), and (2) obtain an estimated spectrum from the so-obtained filtered sequence by the method of LS, which obviously leads to (4.11).

The filterbank interpretation of AFT is useful since it allows us to understand the deficiencies of this approach by simply studying its associated filterbank $\{\mathbf{h}(\omega)\}$. As $\mathbf{h}(\omega)$ is *data-independent* (or non-adaptive) it is no surprise that $\hat{\alpha}_{\mathrm{AFT}}(\omega)$ suffers from leakage and poor resolution problems. A well-designed *data-dependent* filterbank should be able to reduce such problems significantly. Indeed, such a filter should be able to achieve a much larger signal-to-interference-and-noise ratio (SINR) in the filtered data (4.12) than the SINR in the original sequence in (4.1). If this increase in SINR is significant enough to counterbalance the reduction in the number of data samples from N for (4.1) to L for (4.12), then the result will be a spectral estimate $\hat{\alpha}(\omega)$ with enhanced accuracy. This is precisely the idea behind APES, as explained next.

In the APES approach the filterbank $\{\mathbf{h}(\omega)\}$ is designed such that: (a) the filtered sequence is as close to a sinusoidal signal as possible (in a LS sense), and (b) the complex spectrum $\alpha(\omega)$ of $x(n)$ is not distorted by filtering. Mathematically, we obtain $\mathbf{h}(\omega)$ along with the estimate of $\alpha(\omega)$ by minimizing the following LS criterion:

$$\min_{\alpha(\omega),\mathbf{h}(\omega)} \sum_{l=0}^{L-1} \left| \mathbf{h}^H(\omega)\bar{\mathbf{x}}(l) - \alpha(\omega)e^{j\omega l} \right|^2, \quad \text{subject to } \mathbf{h}^H(\omega)\mathbf{a}(\omega) = 1, \qquad (4.13)$$

where the constraint $\mathbf{h}^H(\omega)\mathbf{a}(\omega) = 1$ is imposed to ensure that $\mathbf{h}(\omega)$ passes a sinusoid with frequency ω undistorted (see requirement (b) above). The solution to the above quadratic minimization problem in (4.13) is readily obtained as [10]

$$\hat{\mathbf{h}}(\omega) = \frac{\hat{\mathbf{Q}}^{-1}(\omega)\mathbf{a}(\omega)}{\mathbf{a}^H(\omega)\hat{\mathbf{Q}}^{-1}(\omega)\mathbf{a}(\omega)}, \qquad (4.14)$$

and

$$\hat{\alpha}(\omega) = \hat{\mathbf{h}}^H(\omega)\bar{\mathbf{X}}(\omega), \qquad (4.15)$$

where $\bar{\mathbf{X}}(\omega)$ is the following normalized FT:

$$\bar{\mathbf{X}}(\omega) = \frac{1}{L}\sum_{l=0}^{L-1} \bar{\mathbf{x}}(l)e^{-j\omega l}, \qquad (4.16)$$

52

and

$$\hat{Q}(\omega) = \hat{\bar{R}} - \bar{X}(\omega)\bar{X}^H(\omega) \qquad (4.17)$$

with $\hat{\bar{R}}$ being the following sample covariance matrix:

$$\hat{\bar{R}} = \frac{1}{L}\sum_{l=0}^{L-1}\bar{x}(l)\bar{x}^H(l). \qquad (4.18)$$

To avoid the inversion of an $M \times M$ matrix for each ω, we use the matrix inversion lemma (see, e.g., [22]) to obtain:

$$\hat{Q}^{-1}(\omega) = \hat{\bar{R}}^{-1} + \frac{\hat{\bar{R}}^{-1}\bar{X}(\omega)\bar{X}^H(\omega)\hat{\bar{R}}^{-1}}{1 - \bar{X}^H(\omega)\hat{\bar{R}}^{-1}\bar{X}(\omega)} \qquad (4.19)$$

Let $\hat{\bar{R}}^{-1/2}$ denote the Cholesky factor of $\hat{\bar{R}}^{-1}$, and let

$$\breve{a}(\omega) = \hat{\bar{R}}^{-1/2}a(\omega) \qquad (4.20)$$

$$\breve{X}(\omega) = \hat{\bar{R}}^{-1/2}\bar{X}(\omega) \qquad (4.21)$$

$$\beta(\omega) = \breve{a}^H(\omega)\breve{a}(\omega) \qquad (4.22)$$

$$\gamma(\omega) = \breve{a}^H(\omega)\breve{X}(\omega) \qquad (4.23)$$

$$\rho(\omega) = \breve{X}^H(\omega)\breve{X}(\omega). \qquad (4.24)$$

Then we can rewrite (4.14) and (4.15) as:

$$\hat{h}(\omega) = \frac{[\hat{\bar{R}}^{-1/2}]^H\left[(1-\rho(\omega))\breve{a}(\omega) + \gamma(\omega)\breve{X}(\omega)\right]}{\beta(\omega)(1-\rho(\omega)) + |\gamma(\omega)|^2} \qquad (4.25)$$

and

$$\hat{\alpha}(\omega) = \frac{\gamma(\omega)}{\beta(\omega)(1-\rho(\omega)) + |\gamma(\omega)|^2}, \qquad (4.26)$$

whose implementation requires only the Cholesky factorization of the matrix $\hat{\bar{R}}$ that is independent of ω.

When applied to full data sequences, APES achieves the best performance for a large range of filter lengths M. It can be shown that increasing the filter length increases the

resolution at the cost of reducing the statistical stability [7]. Note that $M = N/2$ is the maximum possible value of M as beyond it $\hat{\bar{\mathbf{R}}}$ becomes singular.

The 2-D spectrum estimation by means of an adaptive filterbank approach is briefly explained as follows. Let $\mathbf{H}(\omega,\bar{\omega})$ denote an $M \times \bar{M}$ 2-D impulse response, where M and $\bar{M}$ are the adaptive filter lengths in range and cross-range, respectively, and let

$$\mathbf{h}(\omega,\bar{\omega}) = \text{vec}\,[\mathbf{H}(\omega,\bar{\omega})] \tag{4.27}$$

where vec[·] denotes the operation consisting of stacking the columns of a matrix on top of each other. Furthermore, let $\mathbf{X}$ denote the 2-D data matrix whose $(n,\bar{n})$th element is $x(n,\bar{n})$, and $\mathbf{Z}_{l,\bar{l}}$ denote the $M \times \bar{M}$ submatrix of $\mathbf{X}$ consisting of the elements $\{x(n,\bar{n}), n = l,\ldots,l+M-1,\ \bar{n} = \bar{l},\ldots,\bar{l}+\bar{M}-1\}$ for $l = 0,1,\ldots,L-1$ and $\bar{l} = 0,1,\ldots,\bar{L}-1$ where $L = N - M + 1$ and $\bar{L} = \bar{N} - \bar{M} + 1$. Define

$$\mathbf{z}_{l,\bar{l}} = \text{vec}[\mathbf{Z}_{l,\bar{l}}], \tag{4.28}$$

and

$$\bar{\mathbf{Z}}(\omega,\bar{\omega}) = \frac{1}{L\bar{L}} \sum_{l=0}^{L-1} \sum_{\bar{l}=0}^{\bar{L}-1} \mathbf{z}_{l,\bar{l}} e^{-j(\omega l + \bar{\omega}\bar{l})}. \tag{4.29}$$

Let

$$\tilde{\mathbf{a}}(\omega,\bar{\omega}) = \bar{\mathbf{a}}(\bar{\omega}) \otimes \mathbf{a}(\omega), \tag{4.30}$$

where $\otimes$ denotes the Kronecker matrix product, $\mathbf{a}(\omega)$ is defined in (4.8), and

$$\bar{\mathbf{a}}(\bar{\omega}) = \begin{bmatrix} 1 & e^{j\bar{\omega}} & \ldots & e^{j(\bar{M}-1)\bar{\omega}} \end{bmatrix}^T. \tag{4.31}$$

Then the 2-D adaptive FIR filter and the APES spectral estimate can be obtained as [7]:

$$\mathbf{h}(\omega,\bar{\omega}) = \frac{\hat{\mathbf{Q}}^{-1}(\omega,\bar{\omega})\tilde{\mathbf{a}}(\omega,\bar{\omega})}{\tilde{\mathbf{a}}^H(\omega,\bar{\omega})\hat{\mathbf{Q}}^{-1}(\omega,\bar{\omega})\tilde{\mathbf{a}}(\omega,\bar{\omega})}, \tag{4.32}$$

and

$$\hat{\alpha}(\omega,\bar{\omega}) = \mathbf{h}^H(\omega,\bar{\omega})\bar{\mathbf{Z}}(\omega,\bar{\omega}), \tag{4.33}$$

where

$$\mathbf{Q}(\omega,\bar{\omega}) = \hat{\mathbf{R}} - \bar{\mathbf{Z}}(\omega,\bar{\omega})\bar{\mathbf{Z}}^H(\omega,\bar{\omega}), \tag{4.34}$$

54

with $\hat{\mathbf{R}}$ being the $M\bar{M} \times M\bar{M}$ sample covariance matrix associated with $\{z_{l,\bar{l}}\}$. A simple expression for $\mathbf{h}(\omega,\bar{\omega})$ can also be obtained similar to (4.25) by making use of the matrix inversion lemma (cf. (4.19)).

Since the 2-D APES algorithm requires the inversion of $(M\bar{M} \times M\bar{M})$ matrix (see, (4.32) and (4.34)), it is computationally prohibitive to apply the algorithm directly to data matrices with large dimensions. Instead we use the chip-based (approximative) implementation of the 2-D APES algorithm proposed in [25], as shown in Figure 4.2. We apply the 2-D FFT to $\mathbf{X}$ to obtain an FFT image and then break it into small overlapping FFT image chips of size $N_s \times \bar{N}_s$ with $N_s < N$ and $\bar{N}_s < \bar{N}$ (in the numerical example, we choose the overlapping to be 50% and set $N_s = \bar{N}_s = 16$ while $N = \bar{N} = 256$). We perform the 2-D IFFT on the small chips to obtain the phase history data chips to which we apply the 2-D APES algorithm. When applying the 2-D APES algorithm to each phase history data chip, we choose the filter lengths $M = N_s/2$ and $\bar{M} = \bar{N}_s/2$ and evaluate the spectrum at a frequency grid that is 4 times finer than the discrete FT (DFT) grid in both range and cross-range. When the image chips are 50% overlapped, we calculate the APES image chips $\hat{\alpha}(\omega, \bar{\omega})$ only over the frequency range $2\pi\frac{1}{4} \leq \omega, \bar{\omega} < 2\pi\frac{3}{4}$ from the each phase history data chip. The final 2-D APES SAR image consists of those APES image chips. Due to overlapping between adjacent image chips, this procedure avoids the mosaicking or tiling effect, which is noticeable for the images shown in [26].

4.4 GAPES for 1-D Gapped Data

In this section, we present the algorithm for the spectral analysis of 1-D gapped data via GAPES. The presentation follows [27]. The application of the GAPES approach to the 2-D SAR imaging with angle diversity data fusion will be given in the next section. We start by describing the algorithm for the spectral estimation of incomplete data with one gap, and then extend it to the data sequence with gaps of various sizes.

4.4.1 A Data Sequence with One Gap

In the case that there is only one gap in the measured data sequence, we can write

$$\mathbf{x}_g = \begin{bmatrix} \mathbf{x}_1^T & \mathbf{x}_2^T & \mathbf{x}_3^T \end{bmatrix}^T. \tag{4.35}$$

In this case, we have $\mathbf{x}_a = [\mathbf{x}_1^T \, \mathbf{x}_3^T]^T$, $\mathbf{x}_u = \mathbf{x}_2$, and $N = N_1 + N_2 + N_3$. The interpolated data vector will be denoted by $\hat{\mathbf{x}}$ in which an estimate $\hat{\mathbf{x}}_u$ of $\mathbf{x}_u$ is obtained and used to replace $\mathbf{x}_u$.

We obtain **initial APES estimates** of $\mathbf{h}(\omega)$ and $\alpha(\omega)$ from the *available data* $\mathbf{x}_a$ in the following way. We choose an initial filter length M_0 such that an initial full-rank covariance matrix $\hat{\bar{\mathbf{R}}}$ can be built with the filter length M_0 and using $\mathbf{x}_a$ only.

Let $L_k = N_k - M_0 + 1$, $k = 1, 3$. We apply APES to $\mathbf{x}_a$ with the following re-definitions:

$$\bar{\mathbf{X}}(\omega) = \frac{1}{L_1 + L_3} \left(\sum_{l=0}^{L_1-1} \bar{\mathbf{x}}(l) e^{-j\omega l} + \sum_{l=N_1+N_2}^{N_1+N_2+L_3-1} \bar{\mathbf{x}}(l) e^{-j\omega l} \right) \tag{4.36}$$

and

$$\hat{\bar{\mathbf{R}}}(\omega) = \frac{1}{L_1 + L_3} \left(\sum_{l=0}^{L_1-1} \bar{\mathbf{x}}(l) \bar{\mathbf{x}}^H(l) + \sum_{l=N_1+N_2}^{N_1+N_2+L_3-1} \bar{\mathbf{x}}(l) \bar{\mathbf{x}}^H(l) \right) \tag{4.37}$$

The APES spectral estimate $\hat{\alpha}(\omega)$ as defined via (4.15) is a continuous function of ω and hence, in principle, we could evaluate it at any frequency value. For the initial estimates we will evaluate $\hat{\alpha}(\omega)$ and $\hat{\mathbf{h}}(\omega)$ at the DFT grid: $\omega_k = 2\pi k/K$ for $k = 0, \ldots, K - 1$ with $K = N$. (We can also choose $K > N$, such as $K = 4N$, for somewhat better results at a cost of more computations). The final spectral estimate can, if desired, be evaluated on a finer grid.

Next we consider **the estimation of $\mathbf{x}_u$** based on the initial spectral estimates $\hat{\alpha}(\omega)$ and $\hat{\mathbf{h}}(\omega)$ obtained as outlined above. Under the fairly natural assumption that the missing data have the same spectral content as the available data we can determine $\hat{\mathbf{x}}_u$ from the condition that the output of the filter $\hat{\mathbf{h}}(\omega_k)$ fed with the data sequence made from $\mathbf{x}_a$ and $\hat{\mathbf{x}}_u$ is as close as possible (in the LS sense) to $\hat{\alpha}(\omega_k) e^{j\omega_k l}$, for $l = 0, \ldots, L - 1$ and $k = 0, \ldots, K - 1$.

56

Mathematically, we propose to obtain $\hat{x}_u$ as the solution to the following LS problem:

$$\min_{x_u} \sum_{k=0}^{K-1} \sum_{l=0}^{L-1} \left| \hat{h}^H(\omega_k) \bar{x}_g(l) - \hat{\alpha}(\omega_k) e^{j\omega_k l} \right|^2 \tag{4.38}$$

where $\bar{x}_g(l)$ is the overlapping vector constructed from x_g in the same way as $\bar{x}(l)$ is formed from x in (4.6). Besides the intuitive appeal of estimating x_u in this way, an additional bonus is that we remain in the APES framework (compare the criteria in (4.13) and (4.38)), an observation to which we will return for further comments later on in this section.

Let the $L \times N$ matrix H_k be defined by

$$H_k = \begin{bmatrix} \hat{h}^H(\omega_k) & & & \\ & \hat{h}^H(\omega_k) & & \\ & & \ddots & \\ & & & \hat{h}^H(\omega_k) \end{bmatrix} \triangleq [\underbrace{A_k}_{L \times N_1} \quad \underbrace{B_k}_{L \times N_2} \quad \underbrace{C_k}_{L \times N_3}] \tag{4.39}$$

and

$$z_k = \hat{\alpha}(\omega_k) \begin{bmatrix} 1 & e^{j\omega_k} & \dots & e^{j(L-1)\omega_k} \end{bmatrix}^T \in \mathcal{C}^{L \times 1}. \tag{4.40}$$

Let $D_k = [A_k \ C_k]$, and define

$$y_k = z_k - D_k x_a. \tag{4.41}$$

Using this notation, we can write the criterion in (4.38) as:

$$\min_{x_u} \sum_{k=0}^{K-1} \| B_k x_u - y_k \|^2 \tag{4.42}$$

whose minimizer with respect to x_u is readily obtained to be

$$\hat{x}_u = \left[\sum_{k=0}^{K-1} B_k^H B_k \right]^{-1} \sum_{k=0}^{K-1} B_k^H y_k. \tag{4.43}$$

Finally, the interpolated data sequence $\hat{x}$ is obtained by replacing x_u with $\hat{x}_u$ in (4.35).

Once an estimate $\hat{x}_u$ has become available, the next logical step should consist of **re-estimating the spectrum** by applying APES to the interpolated data sequence $\hat{x}$ made from x_a and $\hat{x}_u$. According to the discussion around (4.13), this entails the minimization

with respect to $\mathbf{h}(\omega_k)$ and $\alpha(\omega_k)$ of the function:

$$\sum_{k=0}^{K-1} \sum_{l=0}^{L-1} \left| \mathbf{h}^H(\omega_k)\hat{\bar{\mathbf{x}}}(l) - \alpha(\omega_k)e^{j\omega_k l} \right|^2 \tag{4.44}$$

subject to $\mathbf{h}^H(\omega_k)\mathbf{a}(\omega_k) = 1$, where $\hat{\bar{\mathbf{x}}}(l)$ is made from $\hat{\mathbf{x}}$. Evidently the minimization of (4.44) with respect to $\{\mathbf{h}(\omega_k), \alpha(\omega_k)\}_{k=0}^{K-1}$ decouples in K minimization problems of the form of (4.13), yet we prefer to write the criterion function as in (4.44) to make the connection with (4.38). In effect, comparing (4.38) and (4.44) it becomes clear that the alternating estimation of $\{\alpha(\omega_k)\}$ (along with $\{\mathbf{h}(\omega_k)\}$) and $\mathbf{x}_u$ outlined above is nothing but a *cyclic algorithm* for solving the following minimization problem:

$$\min_{\mathbf{x}_u, \{\alpha(\omega_k), \mathbf{h}(\omega_k)\}} \sum_{k=0}^{K-1} \sum_{l=0}^{L-1} \left| \mathbf{h}^H(\omega_k)\bar{\mathbf{x}}_g(l) - \alpha(\omega_k)e^{j\omega_k l} \right|^2 \tag{4.45}$$

subject to $\mathbf{h}^H(\omega_k)\mathbf{a}(\omega_k) = 1$. As is well-known a cyclic minimizer decreases the criterion at each iteration. Furthermore, this decrease must be strict in the present case, as the estimates of $\{\alpha(\omega_k), \mathbf{h}(\omega_k)\}$ and $\mathbf{x}_u$ that we compute at each iteration are uniquely defined (under very weak conditions). Combining these facts with the simple observation that the criterion in (4.45) is nonnegative and hence bounded from below, leads to the conclusion that the cyclic minimizer under discussion will always converge to a minimum point of the criterion. Whether that minimum point is a local or global one, this is a harder question the answer of which will in general depend on the initial estimate used.

The formulation in Equation (4.45) has a strong intuitive appeal as it leads to:

(a) an analysis filterbank $\{\mathbf{h}(\omega_k)\}$ for which the filtered sequence is as close as possible (in the LS sense) to the sinusoidal component in $x(n)$ with frequency $\omega_k \in [0, 2\pi)$,

(b) an estimated complex spectrum that should be almost leakage-free (in view of (a)) and have good statistical properties (inherited from the LS method used to obtain it), and simultaneously,

(c) an estimate of $\mathbf{x}_u$ whose spectral content mimics the spectral content of the available data as much as possible (once again, in the LS sense).

If we estimated $\mathbf{x}_u$ in a way that were different from (4.38) then the above cyclic minimization interpretation would be lost (this interpretation is the bonus of estimating $\mathbf{x}_u$ in the

APES framework, which was mentioned following (4.38)). The same thing would happen if we estimated the spectrum of the interpolated sequence by a method that is different from APES.

The **GAPES** algorithm implements the cyclic minimization of (4.45) outlined above. A step-by-step summary of this algorithm follows.

Step 0: Initialization: start the algorithm using the initialization approach mentioned at the beginning of this section.

Step 1: Gap filling: update the gap estimate in $\{\hat{x}(n)\}$ with $\hat{x}_u$ obtained by using (4.43) based on the most recently determined adaptive FIR filter and APES spectrum $\{\hat{h}(\omega_k), \hat{\alpha}(\omega_k)\}$.

Step 2: Spectrum estimation: determine the adaptive FIR filter and APES spectrum with (4.25) and (4.26), respectively, from the most recently interpolated data sequence $\{\hat{x}(n)\}$.

Step 3: Iteration: repeat Steps 1 and 2 till the relative change of the cost function in (4.45) is equal to or less than a preset threshold value ϵ or the number of iterations reaches a preset number $I_{\max}$.

4.4.2 Spectral Estimation of 1-D Data Sequences with Multiple Gaps

The extension of the algorithm presented in the previous section to the multi-gap case is straightforward. One approach could be to let the gap parameter vector $\mathbf{x}_u$ contain all gaps, accordingly modify (4.42) and all related equations, and then obtain an estimate of missing data simultaneously. However, in many applications, the measured data can be non-stationary but locally stationary. Therefore, we intend to perform the gap filling for each individual gap separately. Each gap is filled in by making use of only the two adjacent continuous segments.

4.5 SAR Imaging for Angle Diversity Data via GAPES

The 1-D GAPES algorithm can be readily applied to SAR imaging with angle diversity data fusion, where the 2-D phase history data matrix $\mathbf{X}_g$ whose $(n, \bar{n})$th element is $x_g(n, \bar{n})$ has missing columns. The principal steps are summarized as follows.

Step I: Perform 1-D WFFT for each available column of the phase history data matrix $\mathbf{X}_g$ to obtain $\mathbf{Y}_1$.

Step II: Fill in the gaps for each row of $\mathbf{Y}_1$ via GAPES to obtain $\mathbf{Y}_2$.

Step III: If a 2-D WFFT SAR image is desired, then compute 1-D WFFTs for each row of $\mathbf{Y}_2$ and stop. Otherwise, go to the next step.

Step IV: Apply 1-D IFFT and de-windowing to each column of $\mathbf{Y}_2$ to obtain the gap-filled phase history data matrix $\hat{\mathbf{X}}$.

Step V: Obtain the 2-D SAR image by applying the chip-based 2-D APES outlined above to the data matrix $\hat{\mathbf{X}}$.

4.6 Numerical Results

We now present some numerical examples to illustrate the performance of the GAPES algorithm for spectral analysis of gapped data and SAR imaging with angle diversity data fusion. We choose $K = N$ for the iteration steps and the spectrum is estimated at discrete frequencies $\omega_k = 2\pi k/K$, or $f_k = \omega_k/2\pi, k = 0, \cdots, K - 1$. The simulated signals in the examples are corrupted by additive zero-mean white Gaussian noise with variance 0.01. In the initialization step for each gap, the filter length is chosen as the smallest integer larger or equal to 3/4 of the length of the shorter adjacent continuous segment. We set $\epsilon = 10^{-2}$ to detect the convergence of the algorithm and the maximum number of iteration is set to $I_{\max} = 10$. After the estimation procedure terminates, we obtain a finer spectral estimate with APES by using $K = 4N$ for the 1-D spectral estimation example.

We compare our algorithm with the WFFT and with the parametric CLEAN algorithm (see e.g. [16]). 1-D and 2-D Taylor windows with order 5 and sidelobe level -35 dB are used for 1-D and 2-D WFFTs, respectively. When using CLEAN, we model each scatterer of the target of interest as a complex sinusoid with constant amplitude and phase. CLEAN first estimates the parameters of the strongest scatterer, subtracts it from the original signal, and then repeats this process for the next strongest scatterer until the predetermined number of scatterers is reached or the estimated amplitude of the current scatterer is small enough compared to the strongest one. Once the scatterer parameters are estimated, they are used

to simulated the data in the gaps. The WFFT approach is then used to form the CLEAN spectrum.

We also consider the Autoregressive (AR) Model based Extrapolation approach, referred to as ARME. Each available data segment (except for the last one) is used with the Yule-Walker method [22, 23, 24], which guarantees stability for forward linear prediction to fill in one half of the gap to the right. Each available data segment (except for the first one) is also used with the Yule-Walker method for backward linear prediction to fill in one half the gap to the left. We choose the AR model order to be one half of the length of the available data segment when it is used to fill in one half of the gap to the right or to the left of the data segment. The WFFT approach is then used to form the ARME spectrum after all the gaps are filled. We remark that although the Yule-Walker method avoids the instability problem for data extrapolation, the extrapolated data sequences exponentially delay to zero, which can cause artifacts (see the examples below).

Figure 4.3 presents an example of spectral analysis of incomplete data with two gaps of different sizes. The total length of the data sequence is $N = 128$ and samples 23 through 46 and 76 through 100 are missing (note that almost 40 percent of the data is missing). Figure 4.3(a) shows the true spectrum which consists of four spectral lines located at $f_1 = 0.05$, $f_2 = 0.065$, $f_1 = 0.26$, and $f_2 = 0.28$ with complex amplitudes $\alpha_1 = \alpha_2 = \alpha_3 = 1$ and $\alpha_4 = 0.5$, respectively, and a continuous spectral component centered at $f_s = 0.18$ with a width $b = 0.015$ and a constant modulus $\alpha = 0.25$. In Figure 4.3(b) the WFFT is applied to the data by filling in the gaps with zeros (note the artifacts in the spectrum due to the missing data). Figures 4.4(c) and (d) show the moduli of the WFFT and APES spectra of the complete data sequence (note the superior resolution of APES as compared to WFFT). Figures 4.3(e) and (f) demonstrate the moduli of the WFFT spectra of the interpolated data sequences via CLEAN and ARME, and Figures 4.3(g) and (h) present the moduli of the WFFT and the APES spectra of the data sequence interpolated via GAPES. Note that in this case, CLEAN and ARME cannot be used to effectively eliminate the spectral artifacts due to the amount of data missing whereas GAPES is shown to be effective for filling in the gaps and estimating the spectrum. In Figure 4.3(i), we show the true data and the data

61

interpolated via GAPES (only the real part is shown; the behavior of the imaginary part is similar). The results displayed so far are for one randomly picked realization of the data. In Figure 4.3(j), we show the GAPES spectrum for five different randomly selected data realizations.

We now illustrate the performance of SAR imaging with angle diversity data fusion via GAPES with the high resolution phase history data of a Slicy object at 0° azimuth angle generated by XPATCH [28], a high frequency electromagnetic scattering prediction code for complex 3-D objects. A photo of the Slicy object taken at 45° azimuth angle is shown in Figure 4.4(a). The original XPATCH data matrix has a resolution of 0.043 meters in both range and cross-range and a size of $N = \bar{N} = 256$. Figures 4.4(b) and (c) show the 2-D WFFT and 2-D chip-based APES SAR images from the complete XPATCH data matrix, respectively.

To demonstrate the advantage of the angle diversity data fusion via GAPES, we artificially create gaps as follows. We consider the first and the last 8 columns of the XPATCH data matrix as missing and let the remaining 240 columns contain 7 uniformly spaced gaps each with 16 columns. Each continuous data segment contains 16 columns as well. The overall missing data percentage is 50%. Figure 4.5(a) exhibits the WFFT image by filling in the gaps with zeros. Note that in cross-range, the point-like scatterers are split into multiple separate point scatterers due to the missing data so that distinct ghosts appear. Figures 4.5(b) and (c) show the SAR images obtained by using 2-D WFFT on the CLEAN and ARME interpolated data, respectively. Shown in Figure 4.5(d) is the SAR image obtained by using 2-D WFFT on the GAPES interpolated data while the final GAPES image obtained by using the 2-D chip-based APES on the GAPES interpolated data is presented in Figure 4.5(e). Note that the spectral lines due to the dihedrals are distorted by CLEAN due to the inherent modeling of them as point scatterers. The ARME approach cannot overcome the missing data-induced ghost problem associated with the point-like scatterer due to the linear prediction model not matching the sinusoidal signal for the point-like scatterer. From Figures 4.4 and 4.5, we observe that the SAR images obtained by using the GAPES interpolated data are almost the same as those obtained by using the complete data.

62

4.7 Conclusions

We have investigated the application of the APES (Amplitude and Phase EStimation) filter to spectral analysis of 1-D gapped data sequences and for 2-D SAR imaging with angle diversity data fusion. The proposed GAPES (Gapped-data APES) algorithm iterates the following two steps: (1) estimating the adaptive filter and the corresponding spectrum via APES, and (2) filling in the gaps via a least squares (LS) fitting. For the SAR imaging with angle diversity data fusion, we performed the 1-D WFFTs in range, used the GAPES algorithm to interpolate the gaps in the aperture for each range, applied the 1-D IFFTs and de-windowed in range, and applied the 2-D APES algorithm to the interpolated matrix to obtain the final 2-D SAR image. Numerical examples have been presented to demonstrate the effectiveness of the algorithm and compare it with the windowed FFT approach, the parametric CLEAN method, and the ARME (AR Model based Extrapolation) approach. The GAPES algorithm has been shown to provide the best spectral estimates and SAR images.

Reference

[1] A. Farina, F. Prodi, and F. Vinelli, "Application of superresolution techniques to radar imaging," *Chinese Journal of Systems Engineering and Electronics*, vol. 5, no. 1, pp. 1–14, January 1994.

[2] S. Barbarossa, L. Marsili, and G. Mungari, "SAR super-resolution imaging by signal subspace projection techniques," *AEU International Journal of Electronics and Communications*, vol. 50, no. 2, pp. 133–138, March 1996.

[3] J. Li and P. Stoica, "Efficient mixed-spectrum estimation with applications to target feature extraction," *IEEE Transactions on Signal Processing*, vol. 44, pp. 281–295, February 1996.

[4] Z.-S. Liu and J. Li, "Feature extraction of SAR targets consisting of trihedral and

dihedral corner reflectors," *IEE Proceedings on Radar, Sonar and Navigation*, vol. 145, pp. 161–172, March 1998.

[5] G. R. Benitz, "High definition vector imaging for synthetic aperture radar," *Proceedings of the 31st Asilomar Conference on Signals, Systems and Computers*, Pacific Grove, CA, November 1997.

[6] S. R. DeGraaf, "Sidelobe reduction via adaptive FIR filtering in SAR imagery," *IEEE Transactions on Image Processing*, vol. 3, pp. 292–301, May 1994.

[7] J. Li and P. Stoica, "An adaptive filtering approach to spectral estimation and SAR imaging," *IEEE Transactions on Signal Processing*, vol. 44, pp. 1469–1484, June 1996.

[8] H. Li, J. Li, and P. Stoica, "Performance analysis of forward-backward matched-filterbank spectral estimators," *IEEE Transactions on Signal Processing*, vol. 46, pp. 1954–1966, July 1998.

[9] R. Wu, J. Li, Z. Bi, and P. Stoica, "SAR image formation via semiparametric spectral estimation," *IEEE Transactions on Aerospace and Electronics Systems*, vol. 35, pp. 1318–1333, October 1999.

[10] P. Stoica, H. Li, and J. Li, "A new derivation of the APES filter," *IEEE Signal Processing Letters*, vol. 6, pp. 205–206, August 1999.

[11] J. Man, G. Liu, and J. Li, "A quasi-parametric algorithm for SAR target feature extraction and imaging with angle diversity," *Circuits, Systems, Signal Processing*, to appear.

[12] E. G. Larsson, P. Stoica, and J. Li, "Spectral analysis of gapped data," *the 34th Asilomar Conference on Signals, Systems, and Computers*, Pacific Grove, CA, submitted 2000.

[13] K. M. Cuomo, J. E. Piou, and J. T. Mayhan, "Ultrawide-band coherent processing," *IEEE Transactions on Antennas and Propagation*, vol. 47, pp. 1094–1107, June 1999.

[14] D. D. Meisel, "Fourier transforms of data sampled in unequally spaced segments," *The Astronomical Journal*, vol. 84, pp. 116–126, January 1979.

[15] J. D. Scargle, "Studies in astronomical time series analysis II: Statistical aspects of spectral analysis of unevenly spaced data," *The Astrophysical Journal*, vol. 263, pp. 835–853, December 1982.

[16] D. H. Roberts, J. Lehár, and J. W. Dreher, "Time series analysis with CLEAN I: Derivation of a spectrum," *The Astronomical Journal*, vol. 93, pp. 968–989, April 1987.

[17] W. Press and G. Rybicki, "Fast algorithm for spectral analysis of unevenly sampled data," *The Astrophysical Journal*, pp. 277–280, March 1989.

[18] J. D. Scargle, "Studies in astronomical time series analysis III: Fourier transforms, autocorrelation functions, and cross-correlation functions of unevenly spaced data," *The Astrophysical Journal*, vol. 343, pp. 874–887, August 1989.

[19] G. B. Rybicki and W. H. Press, "Interpolation, realization, and reconstruction of noisy, irregularly sampled data," *The Astrophysical Journal*, vol. 398, pp. 169–176, October 1992.

[20] P. Stoica, A. Jakobsson, and J. Li, "Capon, APES and matched-filterbank spectral estimation," *Signal Processing*, vol. 66, pp. 45–59, April 1998.

[21] P. Stoica, G. Liu, J. Li, and E. G. Larsson, "Nonparametric spectral analysis of gapped data via an adaptive filtering approach," Submitted to *Circuits, Systems and Signal Processing*, April 2000.

[22] P. Stoica and R. L. Moses, *Introduction to Spectral Analysis.* Englewood Cliffs, NJ: Prentice-Hall, 1997.

[23] S. M. Kay, *Modern Spectral Estimation: Theory and Application.* Englewood Cliffs, N.J.: Prentice-Hall, 1988.

[24] S. L. Marple, Jr., *Digital Spectral Analysis with Applications*. Prentice Hall NJ: Upper Saddle River, 1987.

[25] M. R. Palsetia and J. Li, "Using APES for interferometric SAR imaging," *IEEE Transactions on Imaging Processing*, pp. 1340–1353, September 1998.

[26] S. R. DeGraaf, "SAR imaging via modern 2-D spectral estimation methods," *SPIE Proceedings on Optical Engineering in Aerospace Sensing*, vol. 2230, pp. 36–47, Orlando, FL, April 1994.

[27] P. Stoica, E. G. Larsson, and J. Li, "Adaptive filterbank approach to restoration and spectral analysis of gapped data," *The Astronomical Journal*, to appear.

[28] D. J. Andersh, M. Hazlett, S. W. Lee, D. D. Reeves, D. P. Sullivan, and Y. Chu, "X-PATCH: a high-frequency electromagnetic scattering prediction code and environment for complex three-dimensional objects," *IEEE Antennas and Propagation Magazine*, vol. 36, pp. 65–69, February 1994.
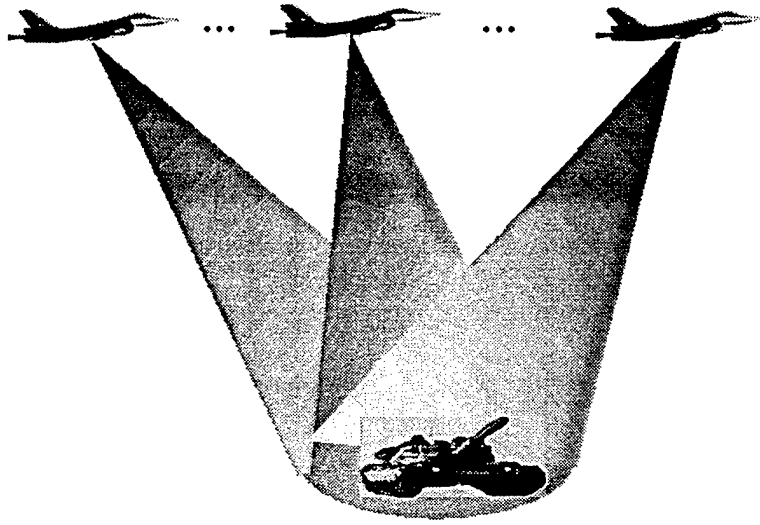
Figure 4.1: Schematic map of a spotlight SAR data acquisition with angle diversity.
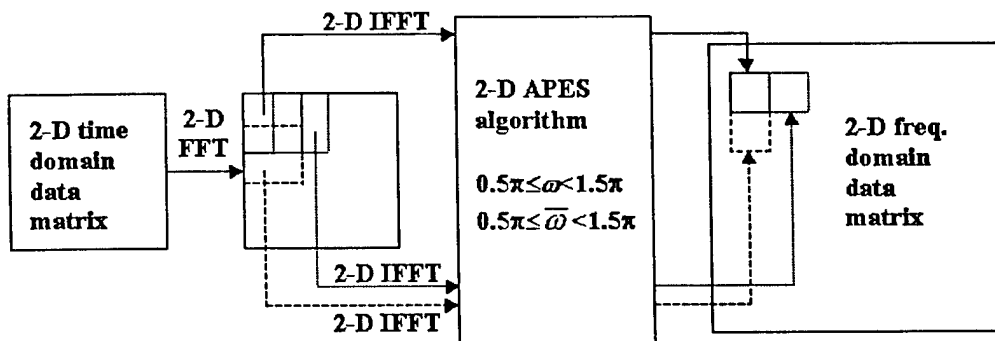
Figure 4.2: Breaking a large data matrix into small chips and applying 2-D APES to each small chip to obtain the 2-D spectral estimation of a data matrix with large dimensions.
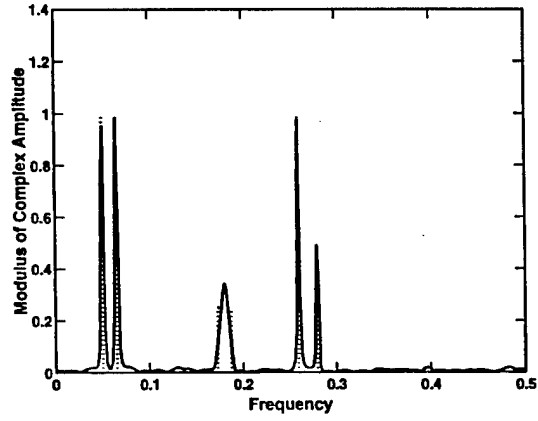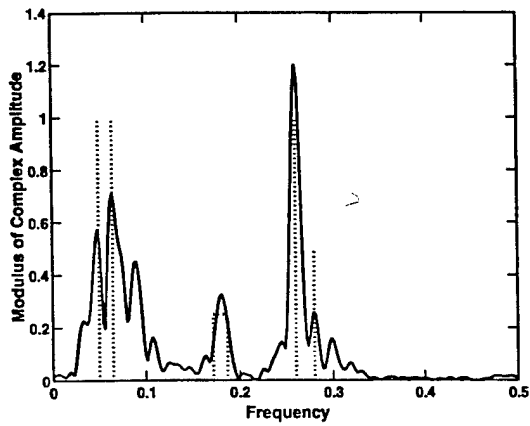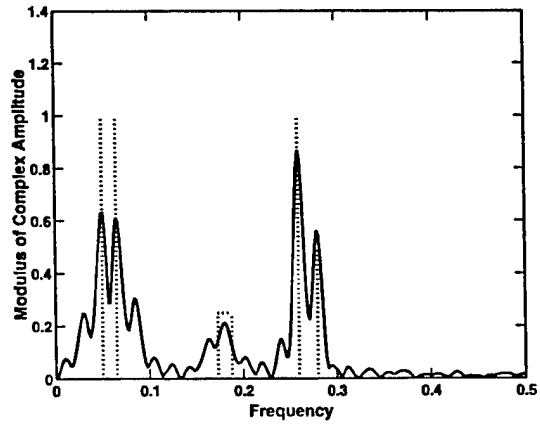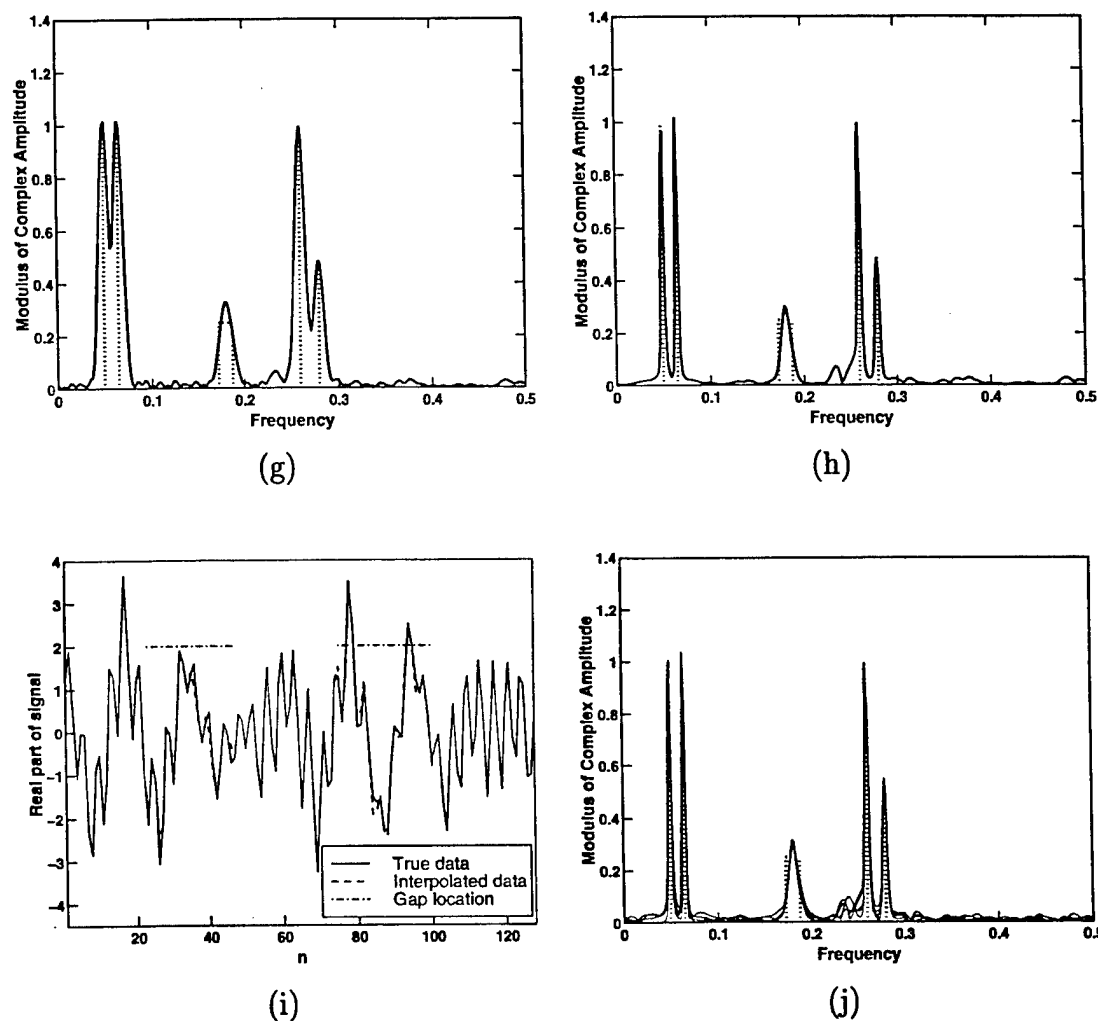
(a)

(b)

(c)

(d)

(e)

(f)

68
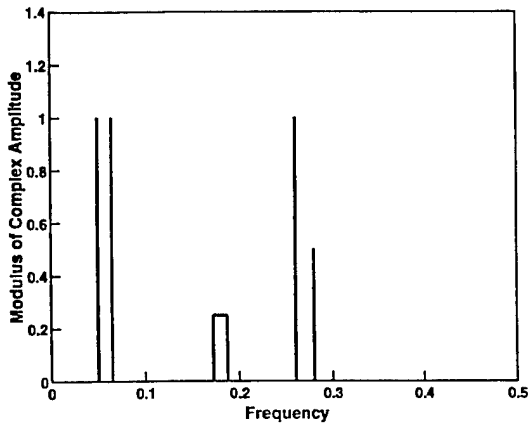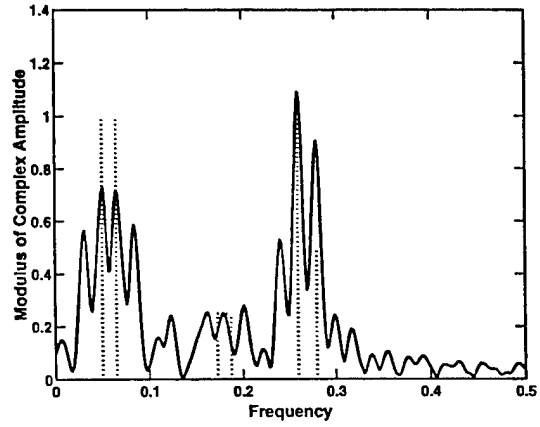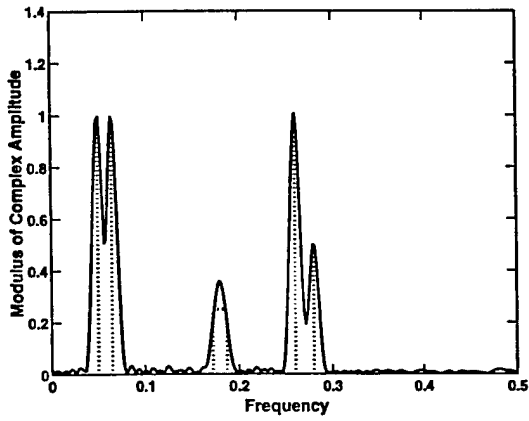
Figure 4.3: Moduli of complex spectral estimates (solid lines in (b)-(h) compared with the true spectrum (dotted lines in (b)-(h)); (a) true spectrum, (b) WFFT spectrum of the gapped data (filling in the gaps with zeros), (c) WFFT spectrum of the complete data, (d) APES spectrum of the complete data, (e) WFFT spectrum of the interpolated data sequence via CLEAN, (f) WFFT spectrum of the interpolated data sequence via ARME, (g) WFFT spectrum of the interpolated data sequence via GAPES, and (h) APES spectrum of the interpolated data sequence via GAPES, (i) True data and data interpolated via GAPES, and (j) GAPES spectrum for five different realizations.
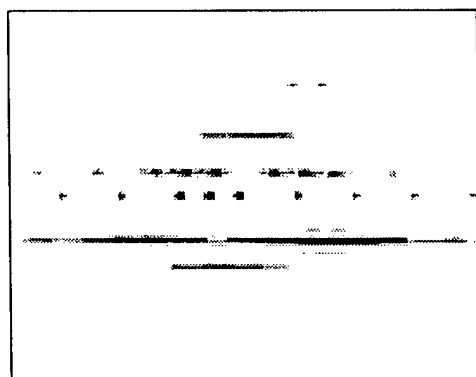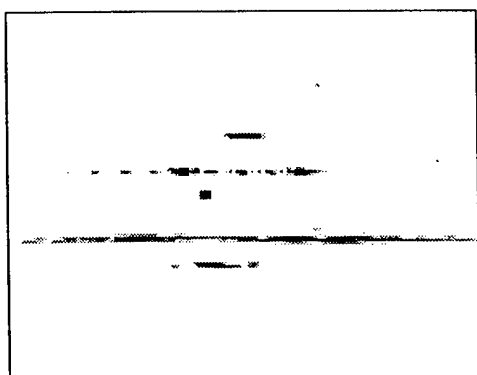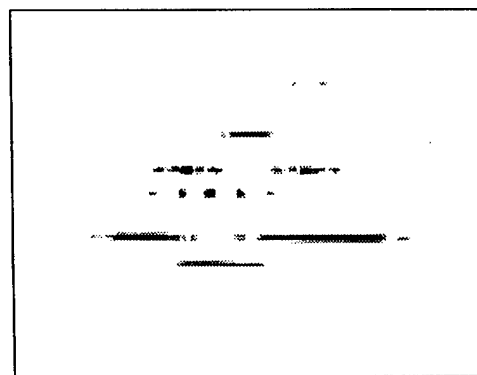
69
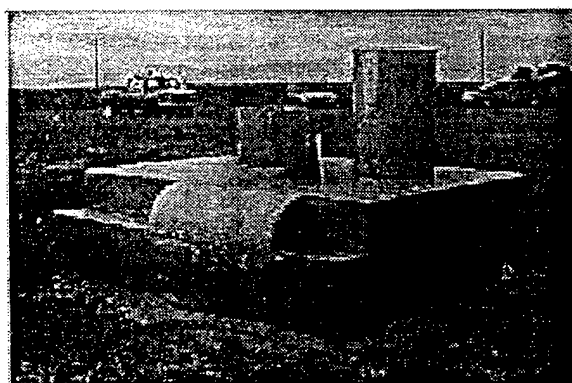
(a)
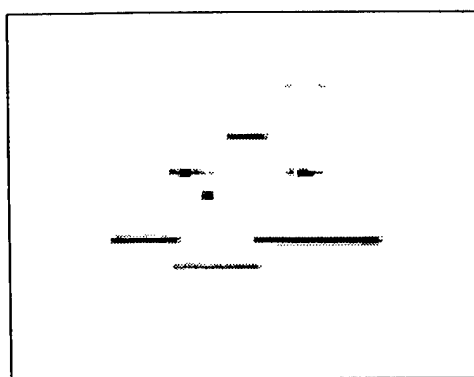
(b)
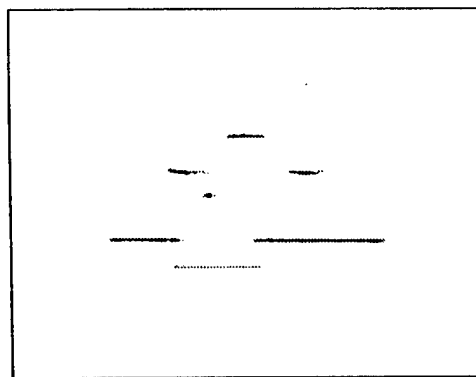
(c)

Figure 4.4: (a) Target photo taken at 45° azimuth angle, and (b) 2-D WFFT (c) and 2-D APES SAR images obtained by using the complete XPATCH data of size 256×256.

(a)
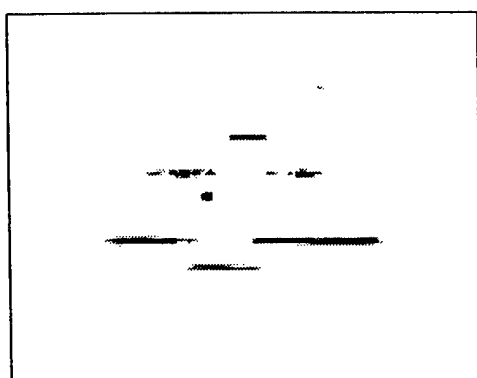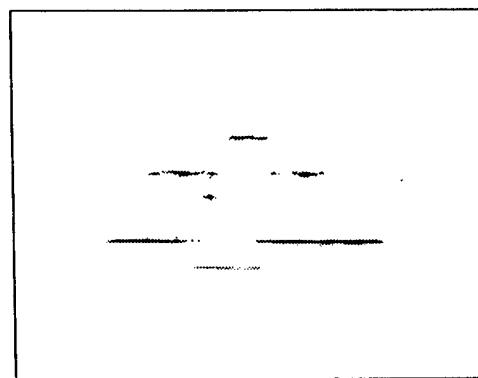
(b)   (c)

(d)   (e)

Figure 4.5: Comparison of SAR images. (a) WFFT image of gapped data matrix, (b) WFFT image with angle diversity data fusion via CLEAN, (c) WFFT image with angle diversity data fusion via ARME, (d) WFFT image with angle diversity data fusion via GAPES, and (e) APES image with angle diversity data fusion via GAPES.

71

5. A Quasi-parametric Algorithm for SAR Target Feature Extraction and Imaging with Angle Diversity

5.1 Introduction

Target feature extraction from spotlight mode synthetic aperture radar (SAR) measurements plays an important role in many applications including battlefield awareness [1] and automatic target recognition (ATR) [2, 3]. Fast Fourier transform (FFT) based approaches have been widely used due to their high computational efficiency and robust performance. However, the disadvantages of such approaches are their low resolution, poor accuracy, and high sidelobes. A variety of spectral estimation methods have been proposed to obtain target features with high resolution and low sidelobes. Of these, the parametric (e.g. [4, 5, 6, 7]), non-parametric (e.g. [8, 9, 10, 11]), and semi-parametric [12] approaches have been considered for SAR image formation and target feature extraction. In general, parametric approaches may outperform their nonparametric counterparts in resolution and accuracy but are more sensitive to data modeling errors.

Azimuth angle diversity data fusion, which combines several sets of radar measurements made at different azimuth angle locations with advanced signal processing methodology, provides a useful tool for SAR target feature extraction and imaging with improved resolution and can be used to achieve better ATR performance. From the viewpoint of signal processing, the solution to the angle diversity data fusion problem shares a similar principle to the missing or gapped data problem, which occurs, for example, in astronomy. Valuable astronomical data are often available only in the form of groups of samples which are gapped within rather long intervals when no reliable measurements can be taken (see, e.g. [13, 14, 15, 16], and the references therein). Special attentions have been paid to detecting the presence of one or more periodic signals from incomplete measurements using techniques such as the periodogram approach [14], the CLEAN deconvolution [15], and/or reconstruction of the unevenly sampled data on a regular grid by making certain assumptions on the data.

Most parametric SAR target feature extraction methodologies make the assumption that

the man-made target of interest consists of several trihedral corner reflectors (point-like scatterers) and derive the corresponding algorithms based on the two-dimensional (2-D) complex sinusoidal data model in which the amplitude and phase are constant in both range and cross-range. However, this data model does not always fit the actual radar observations. Many man-made targets can contain dominant scattering mechanisms other than trihedral-like scatterers. For instance, radar responses from many man-made targets such as vehicles and buildings are primarily caused by both trihedral and dihedral corner reflectors [17]. A principal difference between a trihedral and a dihedral corner reflector lies in their radar responses in cross-range. That is, the former can be modeled as a complex sinusoid with a constant amplitude and phase, while the latter can be approximately described as a complex sinusoid with its amplitude being a sinc function (defined as $\mathrm{sinc}(x)=\sin(x)/x$) and its phase a constant. A mixed data model was presented in [7], which characterizes the reflections in cross-range from a trihedral and a dihedral corner reflector with a constant and a sinc function, respectively. In [12], this data model is extended by modeling each target scatterer as a 2-D complex sinusoid with arbitrary amplitude and constant phase in cross-range and with constant amplitude and phase in range, and a Semi-PARametric (SPAR) algorithm was proposed for SAR target feature extraction and high resolution image formation. Due to its flexible data model, SPAR combines the advantages of both parametric and non-parametric spectral estimation methods, and thus has batter estimation performance and higher resolution capability than nonparametric algorithms and is more robust against data modeling errors over parametric ones.

To achieve excellent ATR performance, the radar range resolution capability is becoming an increasingly important factor to be considered in the radar system design. For example, ultra wideband (UWB) radar has been an effective technology due to its extremely large bandwidth (several GHz) and very high range resolution (on the order of several centimeters). As the range resolution increases, the radar cross-sections of target scatterers vary within the large bandwidth [18], and the assumption of constant responses can no longer hold. This makes the signal processing needed by such ultra high range resolution radars more difficult. More flexible data model is required to achieve robust performance of target feature

extraction.

In this paper, we study the SAR target feature extraction and imaging with angle diversity using an UWB radar. Instead of having a radar collecting data continuously over a large angle to achieve high resolution in cross-range, which is a huge commitment of radar resources, we attempt to achieve high resolution in cross-range by collecting data continuously over a small angle but at several diverse azimuth angle locations. More specifically, with angle diversity, the radar collects data continuously, stops, collects more data continuously, stops again, and so forth. Hence the data available with angle diversity consist of several pieces of the data collected continuously over a large angle. Instead of using the mixed data model in [7] or the semi-parametric data model in [12], we use a more flexible data model, which describes each target scatterer as a 2-D complex sequence with arbitrary amplitude and constant phase in both range and cross-range. This data model is essentially quasi-parametric because of the arbitrary amplitude assumption in both dimensions. The feature extraction algorithm based on such a flexible data model is more robust against the data modeling errors than the parametric and semi-parametric methods. A new algorithm, referred to as the QUALE (QUasi-parametric ALgorithm for target feature Extraction) algorithm, is presented for the SAR target feature extraction with angle diversity. QUALE first chips each scatterer out from the image of the target of interest and apply 2-D inverse FFT (IFFT) to obtain the phase history data. Secondly QUALE estimates the model parameters involved in the flexible data model, which includes, for each scatterer of the target of interest, locations in range and cross-range, a constant phase, and a 2-D arbitrary real-valued amplitude sequence. Thirdly QUALE performs an average in the range dimension over the estimated 2-D real-valued amplitude sequence, models the so-obtained 1-D sequence with a simple sinc function, and estimates the relevant sinc parameters by minimizing a nonlinear least squares (NLS) function. Finally, the 2-D SAR image is reconstructed by using the estimated features. Like the semi-parametric data model in [12], there are also ambiguity problems associated with our data model. To alleviate this problem, QUALE uses an isolation process to chip out the most dominant scatterer with a 2-D window in the image domain, so that it only deals with one scatterer at a time.

The remainder of this paper is organized as follows. Section 2 establishes the data model and formulates the problem of interest. The QUALE algorithm is presented in Section 3. In Section 4, numerical examples are presented to illustrate the performance of the proposed algorithm. Finally, Section 5 contains our conclusions.

5.2 Data Model

To obtain high resolution SAR target features and to reconstruct the SAR images of targets of interest, we need to build a proper data model for the target scatterers. It has been investigated in [12] that the assumption of arbitrary amplitude and constant phase in cross-range is in general more applicable than the mixed data model to characterize the scattering mechanisms including both trihedral and dihedral corner reflectors. Since for an UWB radar collecting data continuously over a large angle, the RCS of a target scatterer is not constant within the radar bandwidth, we model the received signal reflected from a target scatterer as:

$$\tilde{s}(n,\bar{n}) = \tilde{z}(n,\bar{n})e^{j\phi}e^{j2\pi(fn+\bar{f}\bar{n})}, \quad n = 0,1,\cdots,N-1, \quad \bar{n} = 0,1,\cdots,\bar{N}-1, \qquad (5.1)$$

where N and $\bar{N}$ denote the dimensions of data samples in range and cross-range, respectively; $\tilde{z}(n, \bar{n})$ is an arbitrary unknown 2-D real-valued function of n and $\bar{n}$ determined by the RCS of the scatterer as a function of frequency and angle with respect to the radar and the particular scattering mechanism of the scatterer; ϕ is a constant phase; finally, $\{f, \bar{f}\}$ is the frequency pair proportional to the locations in range and cross-range of the scatterer. This data model is essentially quasi-parametric since little parameterization is assumed in either range or cross-range.

Assume that a target of interest consists of K scatterers. Then the target data model in the presence of noise and clutter has the form:

$$\begin{aligned} \tilde{y}(n,\bar{n}) &= \sum_{k=1}^{K} \tilde{z}_k(n,\bar{n})e^{j\phi_k}e^{j2\pi(f_k n+\bar{f}_k\bar{n})} + \tilde{e}(n,\bar{n}), \\ &\quad n = 0,1,\cdots,N-1, \quad \bar{n} = 0,1,\cdots,\bar{N}-1, \end{aligned} \qquad (5.2)$$

75

where $\tilde{z}_k(n, \bar{n})$ denotes an arbitrary 2-D real-valued amplitude function of n and $\bar{n}$ for the kth scatterer; ϕ_k and $\{f_k, \bar{f}_k\}$, respectively, are the constant phase and the frequency pair of the kth scatterer; finally, $\tilde{e}(n, \bar{n})$ denotes the unknown 2-D noise and clutter sequence. Note that, if the amplitude function $\tilde{z}_k(n, \bar{n})$ is assumed to be constant in range, we get the same data model as the one presented in [12].

For angle diversity data fusion, the data measurements are recorded intermittently. For this case, the data model can be expressed as:

$$y(n, \bar{n}) = \begin{cases} 0, & n = 0, 1, \cdots, N-1, \quad \bar{n} \in G, \\ \tilde{y}(n, \bar{n}), & \text{otherwise,} \end{cases} \tag{5.3}$$

where G consists of the indices where the data measurements are not made. Note that, (5.3) is equivalent to setting

$$z_k(n, \bar{n}) = \begin{cases} 0, & n = 0, 1, \cdots, N-1, \quad \bar{n} \in G, \\ \tilde{z}_k(n, \bar{n}), & \text{otherwise,} \end{cases} \tag{5.4}$$

and letting

$$\begin{aligned} y(n, \bar{n}) &= \sum_{k=1}^{K} z_k(n, \bar{n}) e^{j\phi_k} e^{j2\pi(f_k n + \bar{f}_k \bar{n})} + e(n, \bar{n}), \\ & n = 0, 1, \cdots, N-1, \quad \bar{n} = 0, 1, \cdots, \bar{N}-1, \end{aligned} \tag{5.5}$$

where $e(n, \bar{n})$ is formed from $\tilde{e}(n, \bar{n})$ in the same way as $z_k(n, \bar{n})$ is formed from $\tilde{z}_k(n, \bar{n})$. To reduce the amount of computations and avoid model ambiguity, we chip out each scatterer one at a time (see the next section for more details). Our objective is to estimate the model parameters from each scatterer chip.

Once the amplitude estimate of each scatterer is obtained, we attempt to obtain approximate target features by averaging it over n. We remark that we can readily modify our approach to model the amplitude estimate to vary with n as n^α [18]. We choose to average it over n to simplify the problem.

We then approximately model the kth real-valued amplitude average as a sinc function of $\bar{n}$, i.e., as $\alpha_k \text{sinc}\,[\pi b_k(\bar{n} - \tau_k)]$, where α_k, b_k, and τ_k denote the unknown real-valued amplitude, the spectral width, and the signal's peak location of the kth scatterer, respectively.

These three parameters have quite clear physical interpretations. That is, α_k is proportional to the RCS, b_k is related to the length of the scatterer in cross-range, and τ_k gives the peak location of the data sequence and is determined by the orientation of the scatterer. We estimate the approximate scatterer parameters $\{\alpha_k, \ b_k, \ \tau_k\}$ from the amplitude average and reconstruct an approximate 2-D SAR image using the estimated parameters.

5.3 The QUALE Algorithm

The QUALE algorithm consists of three main steps. First, each scatterer is chipped out in the image domain by using an isolation method, which will be described in Section 5.3.1, then 2-D IFFT is applied to the image chip to get the corresponding phase history data of each scatterer. Secondly, the model parameters of each scatterer are estimated according to the 2-D quasi-parametric model in (5.5) (see Section 5.3.2 for details), then the sinc function parameters are estimated by minimizing a NLS cost function (see Section 5.3.2 for details). Finally, the phase history data of each scatterer are simulated according to the estimated scatterer parameters and 2-D FFT is applied to the simulated data to obtain the enhanced image chips, and then these enhanced image chips are put back to the locations of the original image chips to reconstruct the 2-D approximate SAR image (see Section 3.3 for details).

5.3.1 Scatterer Isolation

Because of the flexibility of the data model we use, there will be ambiguity problems when two or more scatterers are located in the same range or cross range. To avoid this problem, we chip each scatterer out and work only on one of them at a time. Before we present the isolation method, we need to consider another problem: when working with the gapped data with angle diversity, the peak of a single scatterer will be split into several peaks, which makes it difficult to single out each scatterer. This phenomenon is illustrated in Figures 5.1(a) and (b). Figure 5.1(a) is the zero-padded FFT of an all-one sequence, and Figure 5.1(b) is the zero-padded FFT of the gapped data due to angle diversity. More specifically, the length of the all-one sequence is 32, the gapped data due to angle diversity is formed by

setting the middle 50% to zero. The two sequences are both zero-padded to 128. It is clear that one peak is split into many peaks. We avoid this peak splitting problem by isolating the scatterers based on the image generated from a continuous data segment that has the most power. Let $\mathbf{X}$ denote the original data matrix and $\check{\mathbf{X}}$ denote the continuous data segment with the most power, with both of which $N \times \bar{N}$ matrices ($\check{\mathbf{X}}$ can be obtained by setting other data segments to zero). Let $\mathbf{V}$ denote the 2-D FFT of $\mathbf{X}$ without zero-padding, and $\check{\mathbf{V}}$ denote the 2-D FFT of $\check{\mathbf{X}}$ with zero-padding to $L \times \bar{L}$, where zero-padding is necessary to improve the accuracy. We determine the size and position of the isolation window of each scatterer on $\check{\mathbf{V}}$ and chip out the scatterer from $\mathbf{V}$.

There is a linear relationship on the size and position between the windows in $\check{\mathbf{V}}$ and $\mathbf{V}$. If $\{l, \bar{l}\}$ is a location in $\check{\mathbf{V}}$, then the corresponding location $\{n, \bar{n}\}$ in $\mathbf{V}$ can be obtained with

$$n = \left\lfloor \frac{N}{L}(l-1) + 1 \right\rfloor, \tag{5.6}$$

and,

$$\bar{n} = \left\lfloor \frac{\bar{N}}{\bar{L}}(\bar{l}-1) + 1 \right\rfloor, \tag{5.7}$$

where $\lfloor \cdot \rfloor$ denotes the nearest integer towards minus infinity. Next we describe how to determine the windows needed to chip out each scatterer. In [12], a windowing method is proposed to chip out the most dominant scatterer one at a time. In this paper, we use a more robust version to meet the requirement of the gapped data due to angle diversity. Unlike SPAR, which uses the same threshold value for both range and cross-range, we use different threshold values for range and cross-range.

To chip out the most dominant scatterer, we first determine the peak location $(l^+, \bar{l}^+)$ from the magnitude of $\check{\mathbf{V}}$. We then fix $\bar{l}$ to $\bar{l}^+$ and search around l^+ by starting from l^+ to determine the interval $l_1 \le l \le l_2$ so that the magnitude of $\check{\mathbf{V}}$ is above a certain threshold T_r. Similarly, we can fix l to l^+ and search around $\bar{l}^+$ by starting from $\bar{l}^+$ to determine the interval $\bar{l}_1 \le \bar{l} \le \bar{l}_2$ so that the magnitude of $\check{\mathbf{V}}$ is above another certain threshold T_{cr}. The corresponding window position $\{n_1, n_2, \bar{n}_1, \bar{n}_2\}$ on $\mathbf{V}$ can be determined according to (5.6) and (5.7). The corresponding phase history data of the scatterer can be obtained by chipping out the image chip determined by $\{n_1, n_2, \bar{n}_1, \bar{n}_2\}$ from $\mathbf{V}$ and applying 2-D IFFT. Note that

when two scatterers are closely spaced in range, they may fall into the same window, which can result in biased target feature estimates. To minimize the problem while determining the interval $\bar{l}_1 \leq \bar{l} \leq \bar{l}_2$, we also check the ratio R between the height of the second peak and that of the strongest peak within the window around $(l^+, \bar{l}^+)$. If it is larger than a threshold T_{ratio}, they will be split into two separate windows with the valley point between the two peaks as the window boundary.

The steps of chipping out all of the scatterers can be summarized as follows:

Step 0: Compute the 2-D FFT $\mathbf{V}$ and $\check{\mathbf{V}}$ of $\mathbf{X}$ and $\check{\mathbf{X}}$, respectively.

Step k: Determine the window $\check{W}_k$ for the strongest scatterer on $\check{\mathbf{V}}$, compute the corresponding window W_k on $\mathbf{V}$. Set those elements of $\check{\mathbf{V}}$ covered by $\check{W}_k$ to zero. Obtain the corresponding phase history data matrix for the scatterer by applying 2-D IFFT to the image chip obtained by applying W_k to $\mathbf{V}$.

Stop: Stop when we have K scatterers, which can be predetermined or according to how strong the new scatterer is as compared to the strongest scatterer.

5.3.2 Scatterer Parameter Estimation

We first present the estimation of the parameters of each scatterer according to the 2-D quasi-parametric model, then the sinc function parameters are estimated by minimizing a NLS cost function.

2-D Quasi-Parametric Parameter Estimation

Due to the scatterer isolation process described in Section 3.1, the phase history data matrix corresponding to the kth scatterer in the presence of noise has the form:

$$
\begin{aligned}
y_k(n, \bar{n}) &= x_k(n, \bar{n}) e^{j\phi_k} e^{j2\pi(f_k n + \bar{f}_k \bar{n})} + e_k(n, \bar{n}), \\
&n = 0, 1, \cdots, N_k - 1, \quad \bar{n} = 0, 1, \cdots, \bar{N}_k - 1,
\end{aligned} \tag{5.8}
$$

where N_k and $\bar{N}_k$ are the dimensions of the kth scatterer data matrix in range and cross-range, respectively; $x_k(n, \bar{n})$ denotes an arbitrary 2-D real-valued amplitude function of n and

79

$\bar{n}$ for the scatterer; ϕ_k and $\{f_k, \bar{f}_k\}$, respectively, are the constant phase and the frequency pair of the scatterer; finally, $e_k(n, \bar{n})$ denotes the unknown 2-D noise and clutter sequence. Let $\mathbf{Y}_k$, $\mathbf{X}_k$, and $\mathbf{E}_k$ be $N_k \times \bar{N}_k$ matrices with their $(n, \bar{n})$th elements being $y_k(n, \bar{n})$, $x_k(n, \bar{n})$ and, $e_k(n, \bar{n})$, respectively. Let $\mathbf{D}(f_k, \bar{f}_k)$ denote the following $N_k \times \bar{N}_k$ matrix:

$$\mathbf{D}(f_k, \bar{f}_k) = \omega_{N_k}(f_k)\omega_{\bar{N}_k}^T(\bar{f}_k), \tag{5.9}$$

where $(\cdot)^T$ denotes the transpose,

$$\omega_{N_k}(f_k) = \begin{bmatrix} 1 & e^{j2\pi f_k} & \cdots & e^{j2\pi(N_k-1)f_k} \end{bmatrix}^T, \tag{5.10}$$

and

$$\omega_{\bar{N}_k}(\bar{f}_k) = \begin{bmatrix} 1 & e^{j2\pi\bar{f}_k} & \cdots & e^{j2\pi(\bar{N}_k-1)\bar{f}_k} \end{bmatrix}^T. \tag{5.11}$$

Then (5.8) can be rewritten in a matrix form as

$$\mathbf{Y}_k = e^{j\phi_k}\mathbf{D}(f_k, \bar{f}_k) \odot \mathbf{X}_k + \mathbf{E}_k, \tag{5.12}$$

where $\odot$ denotes the Hadamard matrix product, i.e., the element-wise matrix product. The NLS estimates $\{\hat{\mathbf{X}}_k, \hat{\phi}_k, \hat{f}_k, \hat{\bar{f}}_k\}$ of $\{\mathbf{X}_k, \phi_k, f_k, \bar{f}_k\}$, can be obtained by minimizing the following cost function

$$\begin{aligned} C_1(\mathbf{X}_k, \phi_k, f_k, \bar{f}_k) &= \left\| \mathbf{Y}_k - e^{j\phi_k}\mathbf{D}(f_k, \bar{f}_k) \odot \mathbf{X}_k \right\|_F^2 \\ &= \sum_{n=0}^{N_k-1} \sum_{\bar{n}=0}^{\bar{N}_k-1} \left| y_k(n, \bar{n}) - x_k(n, \bar{n})e^{j\phi_k}e^{j2\pi(f_k n + \bar{f}_k \bar{n})} \right|^2, \end{aligned} \tag{5.13}$$

where $\| \cdot \|_F$ denotes the Frobenius norm. After some straightforward derivations, we can rewrite (5.13) as

$$\begin{aligned} C_2(\mathbf{X}_k, \phi_k, f_k, \bar{f}_k) &= \sum_{n=0}^{N_k-1} \sum_{\bar{n}=0}^{\bar{N}_k-1} \left\{ |y_k(n, \bar{n})|^2 + \left[x_k(n, \bar{n}) - \text{Re}\left[y_k^*(n, \bar{n})e^{j(2\pi f_k n + 2\pi \bar{f}_k \bar{n} + \phi_k)} \right] \right]^2 \right\} \\ &\quad - \sum_{n=0}^{N_k-1} \sum_{\bar{n}=0}^{\bar{N}_k-1} \left\{ \text{Re}^2\left[y_k^*(n, \bar{n})e^{j(2\pi f_k n + 2\pi \bar{f}_k \bar{n} + \phi_k)} \right] \right\}, \end{aligned} \tag{5.14}$$

80

where Re($\cdot$) denotes the real part and $(\cdot)^*$ denotes the complex conjugate. The estimate of each element of $\mathbf{X}_k$ is given by

$$\hat{x}_k(n, \bar{n}) = \text{Re}\left[y_k^*(n, \bar{n})e^{j(2\pi f_k n + 2\pi \bar{f}_k \bar{n} + \phi_k)}\right]\Big|_{f_k = \hat{f}_k, \bar{f}_k = \hat{\bar{f}}_k, \phi_k = \hat{\phi}_k},$$
$$n = 0, 1, \cdots, N_k - 1, \quad \bar{n} = 0, 1, \cdots, \bar{N}_k - 1. \tag{5.15}$$

Inserting (5.15) into (5.14), we obtain the NLS estimates $\{\hat{\phi}_k, \hat{f}_k, \hat{\bar{f}}_k\}$ of $\{\phi_k, f_k, \bar{f}_k\}$ by equivalently maximizing the following cost function:

$$C_3(\phi_k, f_k, \bar{f}_k) = \sum_{n=0}^{N_k-1} \sum_{\bar{n}=0}^{\bar{N}_k-1} \text{Re}^2\left[y_k^*(n, \bar{n})e^{j(2\pi f_k n + 2\pi \bar{f}_k \bar{n} + \phi_k)}\right]$$
$$= \frac{1}{2} \sum_{n=0}^{N_k-1} \sum_{\bar{n}=0}^{\bar{N}_k-1} \left\{|y_k(n, \bar{n})|^2 + \text{Re}\left[y_k^2(n, \bar{n})e^{-j2(2\pi f_k n + 2\pi \bar{f}_k \bar{n} + \phi_k)}\right]\right\}. \tag{5.16}$$

The estimate of ϕ_k is given by

$$\hat{\phi}_k = \frac{1}{2}\text{angle}\left\{\sum_{n=0}^{N_k-1} \sum_{\bar{n}=0}^{\bar{N}_k-1}\left[y_k^2(n, \bar{n})e^{-j2\pi(2f_k n + 2\bar{f}_k \bar{n})}\right]\right\}\Bigg|_{f_k = \hat{f}_k, \bar{f}_k = \hat{\bar{f}}_k}. \tag{5.17}$$

Inserting (5.17) into (5.16) and dropping out a term that is not related to the frequency estimation, we finally obtain the estimate $\{\hat{f}_k, \hat{\bar{f}}_k\}$ of $\{f_k, \bar{f}_k\}$ by the following maximization:

$$\{\hat{f}_k, \hat{\bar{f}}_k\} = \arg\max_{f_k, \bar{f}_k}\left|\sum_{n=0}^{N_k-1} \sum_{\bar{n}=0}^{\bar{N}_k-1} y_k^2(n, \bar{n})e^{-j2\pi(2f_k n + 2\bar{f}_k \bar{n})}\right|, \tag{5.18}$$

which can be done by simply applying 2-D FFT to $y_k^2(n, \bar{n})$ with $2f_k$ and $2\bar{f}_k$ as the frequency variables.

Note that $\hat{x}_k(n, \bar{n})$ usually does not contain obvious gaps due to chipping or windowing in the image domain. After the estimate $\hat{x}_k(n, \bar{n})$ of $x_k(n, \bar{n})$ is obtained, the segments of $\hat{x}_k(n, \bar{n})$ corresponding to the gaps of $z_k(n, \bar{n})$ should be set to zero. Let G_k contain the indices corresponding to where the gaps of $\hat{x}_k(n, \bar{n})$ should be. Then the relationship between the indices in G_k and G is linear and can be computed with:

$$G_k(i) = \left\lceil \frac{\bar{N}_k}{\bar{N}} G(i)\right\rceil, \tag{5.19}$$

81

or

$$G_k(i) = \left\lfloor \frac{\bar{N}_k}{\bar{N}} G(i) \right\rceil, \qquad (5.20)$$

where $\lceil \cdot \rceil$ and $\lfloor \cdot \rfloor$ denote the nearest integers towards positive infinity and minus infinity, respectively, and $G_k(i)$ and $G(i)$ denote the ith indices of G_k and G, respectively. We compute the begining of the gaps with (5.19) and the end of the gaps with (5.20).

The steps of the parameter estimation for a single scatterer can be summarized as follows:

Step 1: Estimate the frequency pair $\{f_k, \bar{f}_k\}$ with (5.18) by using 2-D FFT with zero-padding to obtain an initial estimate, which is then refined by using the FMINS function of MATLAB.

Step 2: Calculate $\hat{\phi}_k$ according to (5.17) with $\{f_k, \bar{f}_k\}$ replaced by $\{\hat{f}_k, \hat{\bar{f}}_k\}$ obtained in **Step 1**.

Step 3: Determine $\hat{x}_k(n, \bar{n})$, $n = 0, 1, \cdots, N_k - 1, \bar{n} = 0, 1, \cdots, \bar{N}_k - 1$, according to (5.15) with $\{\phi_k, f_k, \bar{f}_k\}$ replaced by $\{\hat{\phi}_k, \hat{f}_k, \hat{\bar{f}}_k\}$ obtained in the previous two steps.

Step 4: Compute the cross-range indices to form G_k and set those columns of $\hat{x}_k(n, \bar{n})$ corresponding to the indices in G_k to zero.

Sinc Function Based Real-Valued Amplitude Estimation

When the estimate of the 2-D real-valued amplitude sequence $\hat{x}_k(n, \bar{n})$ for the kth scatterer is obtained, we average it over the range dimension to obtain

$$\bar{y}_k(\bar{n}) = \frac{1}{N_k} \sum_{n=0}^{N_k-1} \hat{x}_k(n, \bar{n}), \quad \bar{n} = 0, 1, \cdots, \bar{N}_k - 1, \quad \bar{n} \notin G_k. \qquad (5.21)$$

We then approximately model the so-obtained 1-D real-valued sequence with a sinc function. The parameter estimation of the sinc function is given next.

Let

$$\bar{y}_k(\bar{n}) = \alpha_k g_k(\bar{n}) + e_k(\bar{n}), \quad \bar{n} = 0, 1, \cdots, \bar{N}_k - 1, \quad \bar{n} \notin G_k. \qquad (5.22)$$

where $g_k(\bar{n})$ is defined as

$$g_k(\bar{n}) = \text{sinc}\left[b_k \pi (\bar{n} - \tau_k) \right]. \qquad (5.23)$$

Let $\bar{y}_k$ and g_k denote the vectors whose $\bar{n}$th elements are $\bar{y}_k(\bar{n})$ and $g_k(\bar{n})$, $\bar{n} \notin G_k$, respectively. Then the NLS estimates of $\{\alpha_k, b_k, \tau_k\}$ can be determined by minimizing the following cost function

$$C_7(\alpha_k, b_k, \tau_k) = \|\bar{y}_k - \alpha_k g_k\|^2 .$$ (5.24)

Minimizing C_7 in (5.24) with respect to α_k gives the estimate $\hat{\alpha}_k$ of α_k:

$$\hat{\alpha}_k = \left. \frac{g_k^T \bar{y}_k}{\|g_k\|^2} \right|_{b_k = \hat{b}_k, \tau_k = \hat{\tau}_k} .$$ (5.25)

Inserting (5.25) into (5.24), C_7 in (5.24) can be simplified to

$$C_8(b_k, \tau_k) = \|\bar{y}_k\|^2 - \frac{\left(\bar{y}_k^T g_k\right)^2}{\|g_k\|^2},$$ (5.26)

which can be minimized by maximizing its last term

$$C_9(b_k, \tau_k) = \frac{\left(\bar{y}_k^T g_k\right)^2}{\|g_k\|^2}.$$ (5.27)

The maximization of (5.27) requires a 2-D search over the parameter space. We use an alternating maximization procedure by iteratively updating b_k and τ_k while fixing the other parameter.

The initial estimate $\hat{\tau}_k$ of τ_k is obtained by finding the peak position of $\|\bar{y}_k\|$. When we search for $\hat{b}_k$ with the FMIN function of MATLAB, we also need to obtain the initial estimate $\hat{b}_k$ of b_k. We calculate the 1-D FFT $\bar{y}_{kf}$ of the data sequence $\bar{y}_k$ and search two frequency positions $\check{f}_l$ and $\check{f}_r$ nearest to 0, where $\check{f}_l < 0$ and $\check{f}_r > 0$, such that $\left|\bar{y}_{kf}(\check{f}_l)\right| < \frac{1}{2}\left|\bar{y}_{kf}(0)\right|$ and $\left|\bar{y}_{kf}(\check{f}_r)\right| < \frac{1}{2}\left|\bar{y}_{kf}(0)\right|$. The initial estimate $\hat{b}_k$ of b_k is given by

$$\hat{b}_k = \check{f}_r - \check{f}_l.$$ (5.28)

The algorithm for the NLS estimation of the parameters of the sinc function model in (5.22) is described as follows.

Step (1): Obtain the initial estimates $\hat{\tau}_k$ of τ_k by using the above mentioned initialization.

Step (2): Update $\hat{b}_k$. Replace τ_k in (5.27) by $\hat{\tau}_k$ obtained in the previous step and search for $\hat{b}_k$ which maximizes C_9.

Step (3): Update $\hat{\tau}_k$. Replace b_k in (5.27) with $\hat{b}_k$ obtained in **Step (2)** and search for $\hat{\tau}_k$ which maximizes C_9.

Step (4): Repeat **Steps 2** and **3** until "practical convergence" which is determined by checking the relative change ϵ of the cost function C_9 in (5.27) between two consecutive iterations. We use $\epsilon = 10^{-3}$ in our numerical examples.

Step (5): Calculate $\hat{\alpha}_k$ using (5.25).

5.3.3 Image Reconstruction

After the estimates $\left\{ \hat{\alpha}_k, \hat{b}_k, \hat{\tau}_k \right\}_{k=1}^{K}$ of the sinc function parameters are obtained, we simulate $\left\{ \{\tilde{\tilde{y}}_k(\bar{n})\}_{\bar{n}=1}^{\bar{N}_k} \right\}_{k=1}^{K}$ by using $\left\{ \hat{\alpha}_k, \hat{b}_k, \hat{\tau}_k \right\}_{k=1}^{K}$ according to (5.22), and repeat $\left\{ \{\tilde{\tilde{y}}_k(\bar{n})\}_{\bar{n}=1}^{\bar{N}_k} \right\}_{k=1}^{K}$ in range to obtain the 2-D real-valued amplitude $\{\tilde{X}_k\}_{k=1}^{K}$, that is

$$\tilde{x}(n,\bar{n})_k = \tilde{\tilde{y}}_k(\bar{n}), \quad n = 0, 1, \cdots, N_k - 1, \quad \bar{n} = 0, 1, \cdots, \bar{N}_k - 1, \quad k = 1, 2, \cdots, K. \quad (5.29)$$

With $\{\tilde{X}_k\}_{k=1}^{K}$ and $\{\hat{\phi}_k, \hat{f}_k, \hat{\bar{f}}_k\}_{k=1}^{K}$, the phase history data matrix of each scatterer is simualted without gaps. Then we perform the 2-D FFT on the simulated phase history data matrix to obtain the enhanced image chip for each scatterer. Each enhanced image chip is put back to its original location in the FFT image **V** defined in Section 5.3.1 to reconstructed the approximate SAR image of the target. If the image chips of different scatterers overlap, we use whichever is stronger for the overlapping part.

5.4 Numerical Results

We illustrate the SAR target feature extraction and imaging performance of QUALE with a set of high resolution phase history data generated by XPATCH [19], a high frequency electromagnetic scattering prediction code for complex 3-D objects. A photo of the slicy object taken at 45° azimuth angle and the corresponding FFT SAR image from the XPATCH data obtained at 0° are, respectively, shown in Figures 5.2(a) and (b) where a good agreement between the slicy object and the image can be seen clearly. The XPATCH data matrix we use has a resolution of 0.038 meters in both range and cross-range and a size of $N = \bar{N} =$

288. To demonstrate the advantages of the angle diversity data fusion, we assume that we have three segments of the XPATCH phase history data available to us with each segment consisting of continuous data columns from the beginning, middle, and end of the original data matrix. Hence the data are collected at three diverse azimuth angle locations.

Now we compare QUALE with the FFT approaches as well as CLEAN, which has been proved to be very useful in several applications including astronomical data analysis, microwave imaging, spectral estimation, and target feature extraction. When using CLEAN, we model each scatterer of the target of interest as a complex sinusoid with constant amplitude and phase in both range and cross-range. CLEAN first estimates the parameters of the strongest scatterer, subtracts it from the original signal, and then repeats this process for the next strongest scatterer until the predetermined number of scatterers is reached or the estimated amplitude of the current scatterer is small enough. Once the scatterer parameters are estimated, they are used to simulate the data in the missing gaps. FFT is then used to form the CLEAN images. Since CLEAN uses a point-like scatterer model, a larger number of scatterers have to be assumed to model a dihedral corner reflector. We set a total number of scatterers to be 30 for CLEAN.

The thresholds T_R and T_{CR} used in the isolation process of QUALE is 2% and 5% of the peak value in range and cross-range, respectively. We implement the scatterer isolation process of QUALE based on the 2-D FFT of the middle segment of the gapped data with zero-padding. In a cross-range, if the second peak is greater than 40% of the largest one in one window, they will be split into two windows. We assume that the number of scatterers is $K = 7$ for QUALE.

We first consider a case where the gapped data set due to angle diversity contains 50% of the original XPATCH data set. The original data matrix in columns 49 through 120 and 169 through 240 are set to zero to form the gapped data set. Hence the angle diversity data we use in this example has three non-zero data segments (each with 48 columns) intermitted by two gaps (each with 72 columns). Figure 5.3(a) shows the windows used by QUALE to chip out the 7 scatterers. Figures 3(b) and (c) show the FFT SAR images obtained by using the middle segment only and all of the segments, respectively. Compared with Figure 5.2(b),

Figures 3(b) and (c) exhibit distinct energy leakage in cross-range from the mainlobes of the scatterers, with peak splitting occurring in Figure 5.3(c) due to the gapped data. Figures 3(d) shows the SAR image obtained by using CLEAN. The SAR image obtained via QUALE is presented in Figure 5.3(e). Note that, CLEAN generates images with isolated points. The line-shaped features in cross-range caused by dihedral-like scatterers (see Figure 5.2) are represented with several point scatterers. For the trihedral type of corner reflectors, CLEAN works very well since the data model is quite accurate. From Figure 5.3(d) we note that QUALE can generate better images than the FFT approaches and CLEAN for dihedral type of corner reflectors. For this example, our simulations show that the ratios between the MATLAB flops needed by CLEAN and QUALE over those needed by the FFT approaches are, 178.73 and 11.59, respectively. CLEAN requires much more computations than QUALE because the former performs 2-D FFT on the entire data matrix while QUALE works with the scatterer image chips with much smaller dimensions. Also, the NLS approach used to estimate the sinc function parameters in QUALE causes little additional burden to the total amount of computations since the approach convergences quickly within a few iterations.

Consider next an example with much larger gaps. We set the original XPATCH data matrix in columns 11 through 139 and 150 through 278 to zero to form the angle data diversity data set. Three data segments each with 10 columns are separated by two gaps each with 129 columns. That is, the total angle diversity data set contains only 10% of the original data set. The cross-range resolution of each segment is $288 \times 0.038/10 \approx 1.094$ meters. The windows used by QUALE to chip out the 7 scatterers is shown in Figure 5.4(a). The SAR images obtained by using the FFT approaches, CLEAN, and QUALE are shown in Figures 5.4(b) through (e), which correspond to the images in Figures 5.3(b) through (e), respectively. A comparison between Figures 5.3 and 5.4 shows that the FFT SAR images become worse due to the larger data gaps with more mainlobe energy leaked in cross-range and more severe peak splitting. While both FFT approaches and CLEAN need the same amounts of computations as in the previous example, QUALE requires approximately 40% more computations than in the previous example due to larger image chips. Hence QUALE is still computationally much more efficient than CLEAN.

5.5 Conclusions

We have presented a quasi-parametric estimation algorithm, referred to as QUALE, for approximate SAR target feature extraction and imaging with angle diversity based on a flexible data model, which describes each target scatterer as a 2-D complex sequence with arbitrary amplitude and constant phase in range and cross-range. This data model is essentially quasi-parametric because of the arbitrary amplitude assumption. QUALE first estimates the model parameters that include, for each scatterer, a 2-D arbitrary real-valued amplitude sequence, a constant phase, and the locations in range and cross-range. It then averages the estimated 2-D real-valued amplitude sequence over the range dimension, approximately models the so-obtained 1-D sequence with a sinc function, and estimates the sinc function parameters by minimizing a NLS cost function. Finally, the 2-D SAR image is reconstructed by using the estimated features. We have shown with XPATCH simulated examples that QUALE outperforms the FFT approaches and the well-known CLEAN algorithm for a target containing both dihedrals and trihedrals even in the presence of very large data gaps. QUALE is also computationally much more efficient than CLEAN.

Reference

[1] M. T. Fennell and R. P. Wishner, "Battlefield awareness via synergistic SAR and MTI exploitation," *IEEE Aerospace and Electronic Systems Magazine*, vol. 13, no. 2, pp. 39–45, February 1998.

[2] S. Hudson and D. Psaltis, "Correlation filters for aircraft identification from radar range profiles," *IEEE Transactions on Aerospace and Electronic Systems*, vol. 29, pp. 741–748, July 1993.

[3] S. P. Jacobs and J. A. O'Sullivan, "High resolution radar models for joint tracking and recognition," *IEEE National Conference on Radar,* Syracuse, New York, pp. 99–104, May 1997.

[4] A. Farina, F. Prodi, and F. Vinelli, "Application of superresolution techinques to radar imaging," *Chinese Journal of Systems Engineering and Electronics,* vol. 5, no. 1, pp. 1–14, January 1994.

[5] S. Barbarossa, L. Marsili, and G. Mungari, "SAR super-resolution imaging by signal subspace projection techniques," *AEU International Journal of Electronics and Communications,* vol. 50, no. 2, pp. 133–138, March 1996.

[6] J. Li and P. Stoica, "Efficient mixed-spectrum estimation with applications to target feature extraction," *IEEE Transactions on Signal Processing,* vol. 44, pp. 281–295, February 1996.

[7] Z.-S. Liu and J. Li, "Implementation of the RELAX algorithm," *IEEE Transactions on Aerospace and Electronics Systems,* vol. 34, pp. 657–664, April 1998.

[8] G. R. Benitz, "High definition vector imaging for synthetic aperture radar," *Proceedings of the 31st Asilomar Conference on Signals, Systems and Computers,* Pacific Grove, CA, November 1997.

[9] S. R. DeGraaf, "Sidelobe reduction via adaptive FIR filtering in SAR imagery," *IEEE Transactions on Image Processing,* vol. 3, pp. 292–301, May 1994.

[10] J. Li and P. Stoica, "An adaptive filtering approach to spectral estimation and SAR imaging," *IEEE Transactions on Signal Processing,* vol. 44, pp. 1469–1484, June 1996.

[11] H. Li, J. Li, and P. Stoica, "Performance analysis of forward-backward matched-filterbank spectral estimators," *IEEE Transactions on Signal Processing,* vol. 46, pp. 1954–1966, July 1998.

[12] R. Wu, J. Li, Z. Bi, and P. Stoica, "SAR image formation via semiparametric spectral estimation," *IEEE Transactions on Aerospace and Electronics Systems,* vol. 35, October 1999.

[13] D. D. Meisel, "Fourier transforms of data sampled in unequally spaced segments," *The Astronomical Journal*, vol. 84, pp. 116–126, January 1979.

[14] J. D. Scargle, "Studies in astronomical time series analysis II: Statistical aspects of spectral analysis of unevenly spaced data," *The Astronomical Journal*, vol. 263, pp. 835–853, December 1982.

[15] D. H. Roberts, J. Lehár, and J. W. Dreher, "Time series analysis with CLEAN I: Derivation of a spectrum," *The Astronomical Journal*, vol. 93, pp. 968–989, April 1987.

[16] G. B. Rybicki and W. H. Press, "Interpolation, realization, and reconstruction of noisy, irregularly sampled data," *The Astronomical Journal*, vol. 398, pp. 169–176, October 1992.

[17] V. Larson and L. Novak, "Polarimetric subspace target detector for SAR data based on the Huynen dihedral model," *Proceedings of SPIE*, vol. 2487, pp. 235–250, Orlando, Florida, April 1995.

[18] K. M. Cuomo, J. E. Piou, and J. T. Mayhan, "Ultrawide-band coherent processing," *IEEE Transactions on Antennas and Propagation*, vol. 47, pp. 1094–1107, June 1999.

[19] D. J. Andersh, M. Hazlett, S. W. Lee, D. D. Reeves, D. P. Sullivan, and Y. Chu, "X-PATCH: a high-frequency electromagnetic scattering prediction code and environment for complex three-dimensional objects," *IEEE Antennas and Propagation Magazine*, vol. 36, pp. 65–69, February 1994.
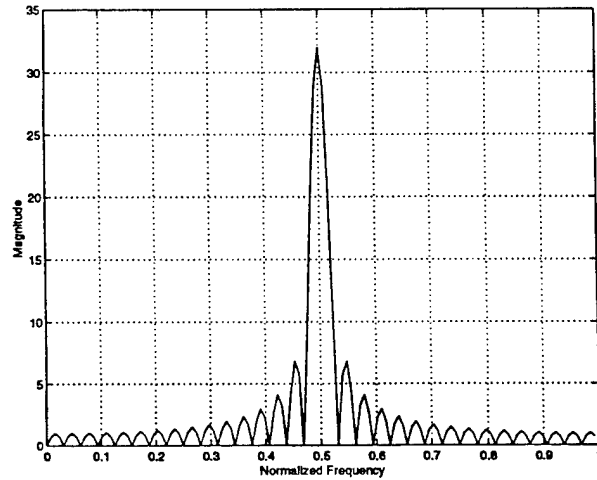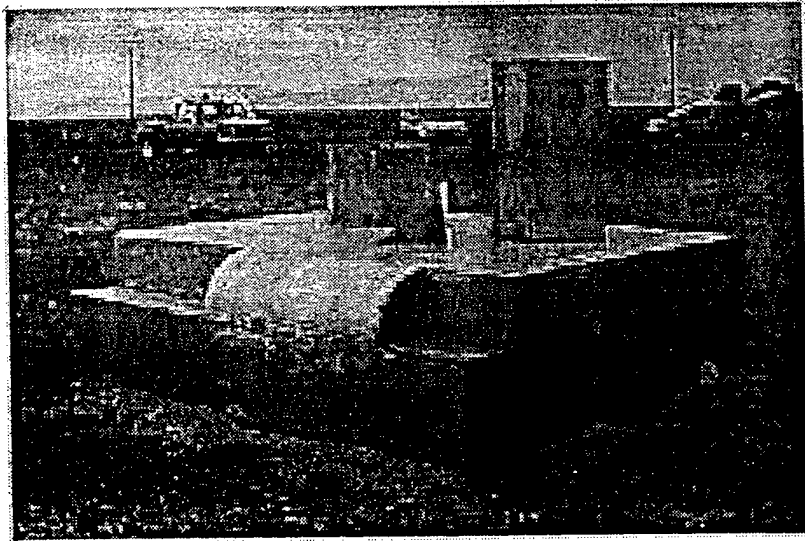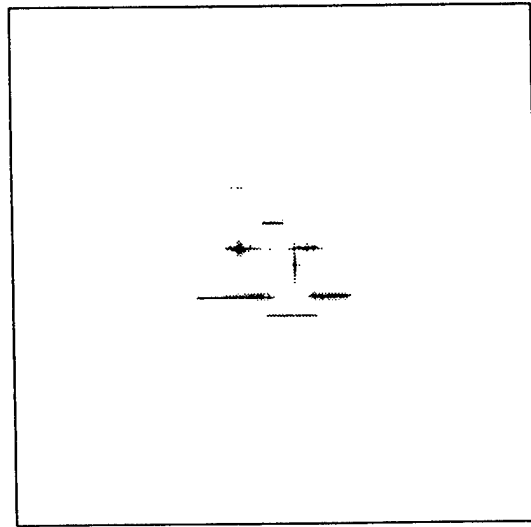
(a)
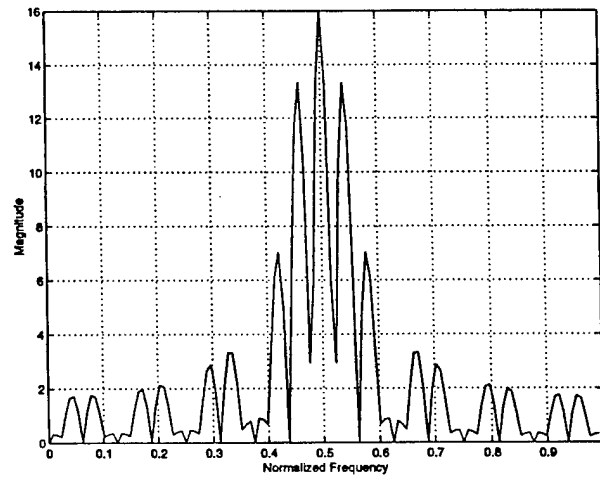
(b)

Figure 5.1: 1-D FFTs of continuous data and gapped data due to angle diversity. The continuous data used is an all-one sequence with length 32, and the gapped data due to angle diversity is formed by setting the middle 50% of the continuous data to zero. (a) FFT of continuous data, (b) FFT of gapped data due to angle diversity.
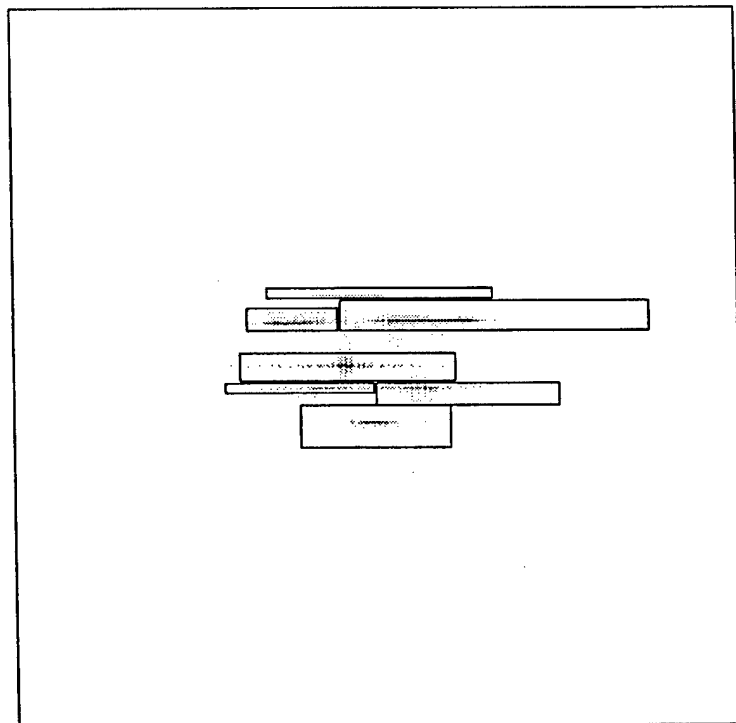
90

(a)

(b)

Figure 5.2: (a) Target photo taken at 45° azimuth angle, (b) 2-D FFT SAR image obtained at 0° azimuth angle using the entire XPATCH data with a resolution 0.038 meters in both range and cross-range.
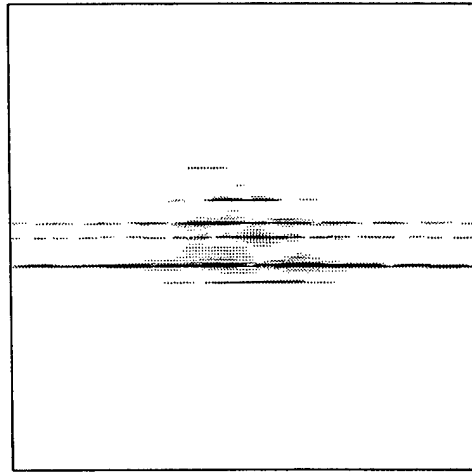
(a)

(b) (c)

(d) (e)
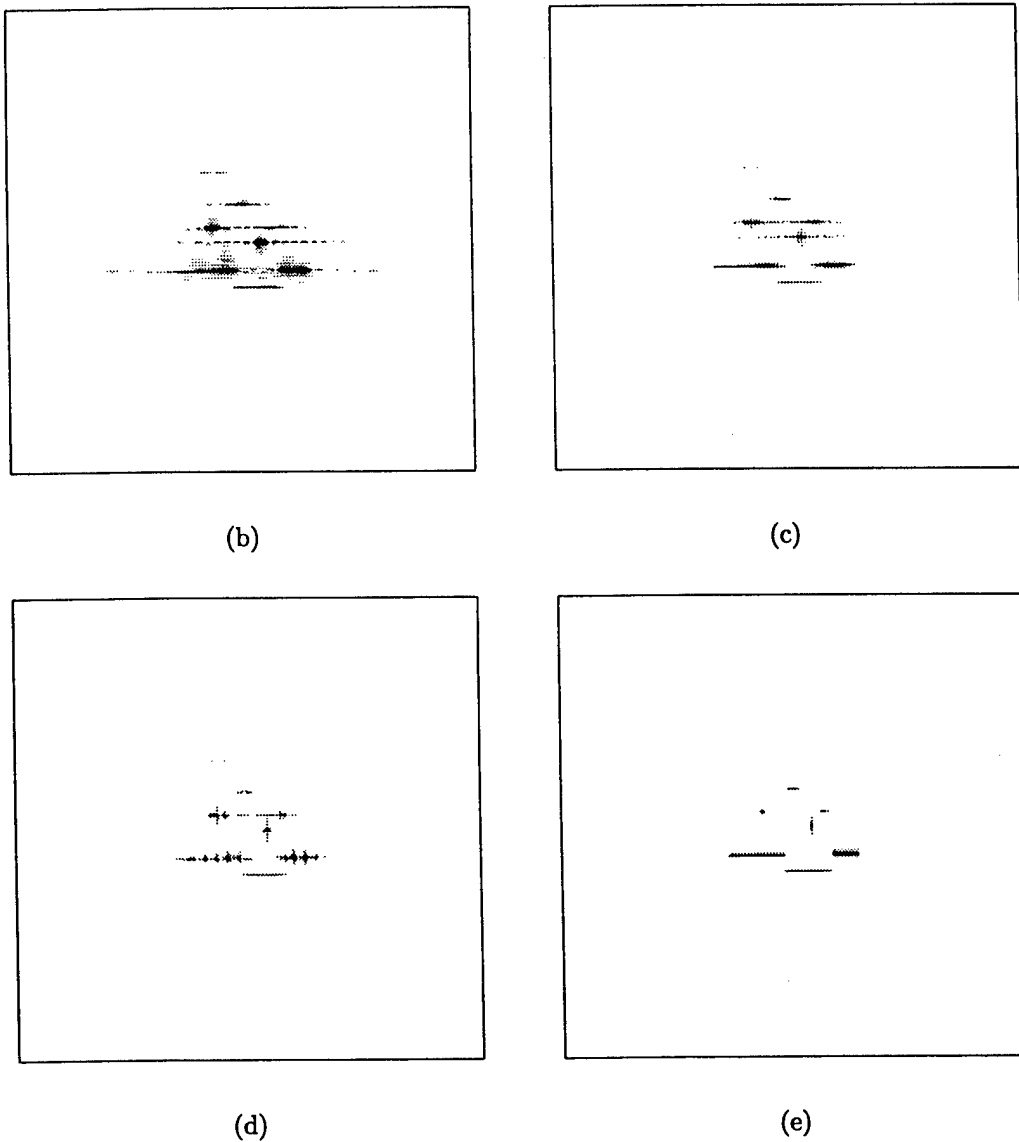
Figure 5.3: Comparison of SAR images obtained via different algorithms for the XPATCH data with two gaps in cross-range (only 50% of the data are used with cross-range resolution of each segment being $288 \times 0.038/48 \approx 0.228$ meters). (a) The windows used by QUALE to chip out the 7 scatterers, (b) 2-D FFT SAR image from the middle segment of the gapped XPATCH data with zero-padding, (c) 2-D FFT SAR image from the entire gapped XPATCH data, (d) CLEAN SAR image, and (d) QUALE SAR image.
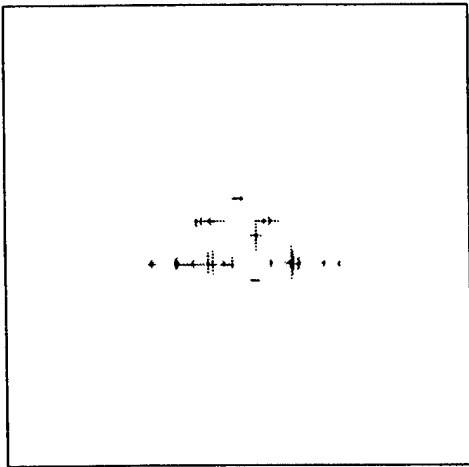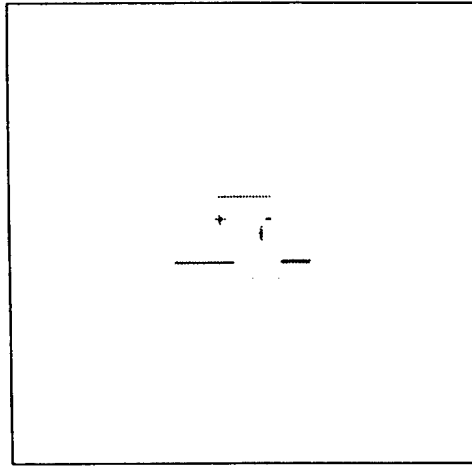
93

(a)
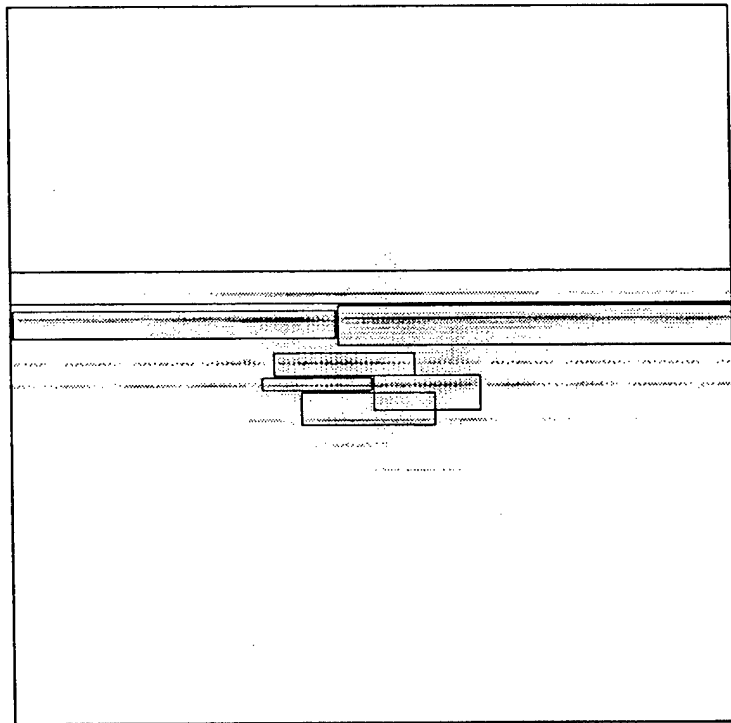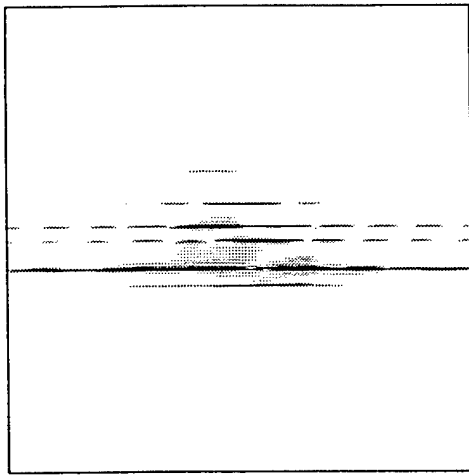
Figure 5.4: Comparison of SAR images obtained via different algorithms for the XPATCH data with two gaps in cross-range (only 10% of the data are used with cross-range resolution of each segment being $288 \times 0.038/10 \approx 1.094$ meters). (a) The windows used by QUALE to chip out the 7 scatterers, (b) 2-D FFT SAR image from the middle segment of the gapped XPATCH data with zero-padding, (c) 2-D FFT SAR image from the entire gapped XPATCH data, (d) CLEAN SAR image, and (d) QUALE SAR image.